University of Alberta
Department of Civil Engineering

THE EFFECT OF TENSION FLANGE

MOVEMENT ON THE STRENGTH OF

POINT LOADED I-BEAMS

by

Dean Mullin

and

J.J. Roger Cheng

January, 1995

THE EFFECT OF TENSION FLANGE MOVEMENT ON THE STRENGTH OF POINT LOADED I-BEAMS

by

Dean Mullin

and

J.J. Roger Cheng

Department of Civil Engineering

University of Alberta

Edmonton, Alberta, Canada T6G 2G7

January, 1995

ABSTRACT

The tension flange movement failure mode was first observed during a test at the University of Texas in 1968. To date, only one research project has been conducted to further explore this failure mode. The objective of this project is to add to the current body of test data set and further understanding of this failure mode.

Two experimental programs were conducted. First, a series of nine scale model tests were conducted on styrene I-beams of various cross sections. The model tests were designed to study effects of in-plane and out-of-plane beam stiffness variation by through flange width and thickness variation. Beams were mid-span loaded and simply supported. Five full scale tests were conducted in the second phase of the research. Two cross sections, W360x33 and W360x39, were tested at various span lengths. Beams were point loaded at mid-span. Restraining moments with no bottom flange warping restraints were provided at the ends of the beams. Compression flange lateral bracing was provided for all tests and exceeded S16.1-M89 requirements for lateral bracing.

Both full scale and model tests exhibited lateral tension flange movement at failure. There was little reserve strength and ductility past the peak test load. Test to predicted ratios are provided for finite element analysis results (Test / Pred. = 1.140 to 0.274) and the AISC-LRFD design equation (Test / Pred. = 6.005 to 0.932). An interaction formula considering flexural and vertical web stresses below the concentrated load is proposed and compared to test data (Test / Pred. = 1.198 to 0.612). The S16.1-M89 design specification web crippling and web yielding design strengths are shown to exceed test peak loads for all full scale tests.

The wide range of test / predicted ratios for all predictive model clearly demonstrated the need for further research of the tension flange movement failure mode.

ii

ACKNOWLEDGMENTS

CONTENTS

LIST OF FIGURES

LIST OF TABLES

1   DEFINITION OF PROBLEM

1.1   University of Texas Tests

Between 1969 and 1971, the University of Texas performed research to further the understanding of the relationship between lateral and local instability of steel I-beams (*Costley*, 1970; *Bansal*, 1971). Tests were conducted on continuous doubly symmetric I-beams with point loads along their length and unequal end moments. The flange width to thickness ratio and unbraced length exceeded American Institute of Steel Construction (AISC) Specification (1969) requirements to facilitate investigation of the safety of the specification equations. Stiffeners were omitted where possible to further test the conservatism of the AISC specification design equations for local and lateral buckling in plastic design.

During the test program, it was noted that several specimens failed via tension flange movement rather than the expected web buckling, web crippling or lateral torsional buckling modes. The first instance of tension flange movement resulting in premature and unexpected failure of the specimen was very sudden. The beam was nearing the formation of a plastic hinge when the tension flange kicked out from beneath the load, resulting in a large decrease in the load carrying capacity of the member. The failure occurred without warning and the buckled system had very little rotational capacity. Figure 1.1 (*Costley*, 1970) shows the load versus in-plane mid-span deflection of the failed beam as well as the predicted elastic-plastic response of the system (dashed line). P_{max} is the maximum load reached during the test while P_u is the unfactored capacity of the system.

theory by *Summers,* it will be referred to as that here, and referenced *Summers* (1982).

The *Basler* theory adopts the traditional view of web buckling in which the flanges do not move laterally and can be considered braced members. The *Yura* theory acknowledges that the tension flange, if unbraced, can move laterally and in doing so develop elastic restraining forces for the web (*Summers,* 1982). If the forces developed by this lateral movement are not sufficient to equilibrate the lateral force induced by geometry changes and vertical loads, buckling will occur. The *Yura* theory considers the lateral stiffness of the tension flange, simply supported and point loaded in its strong direction at mid-span, as the restraining stiffness of the flange, as shown in Figure 1.4.

Replacing the lateral support of the tension flange in *Baslers* theory with a lateral spring of stiffness, k, where:

$$[1.1] \; k = \frac{48EI_f}{L^3}$$

E = Modulus of Elasticity

If = Moment of Inertia of the Tension Flange about the Strong Axis

L = Beam Span

results in the system shown in Figure 1.4.

Performing a buckling analysis on that system yields an equation, represented by the non dimensional plot shown in Figure 1.5. P_E in the figure is defined as the elastic buckling load of a pinned-pinned column. Using the non-

dimensional plot, properties of the beam cross-section and material properties, a tension flange movement failure load can be estimated.

1.4   The AISC Sidesway Buckling Equation

After the observation of capacity reduction of point loaded beams with unstiffened webs, *Yura* suggested that the AISC Specifications should include a sidesway buckling provision. The development of the set of equations, which appear in the first edition of the AISC-LRFD Specification (1986) and the ninth edition of the AISC-ASD (Allowable Stress Design) (1989), involved the simplification of the original *Yura* theory. A fundamental simplification involved the assumption that the web depth to thickness ratio of beams would be 40 for all cases. This ratio represents an upper limit for economic cross-sections in bending. The loaded flange may be considered either restrained from rotation (as in the *Basler* theory) or not restrained from rotation.

The calculation of failure loads in the specifications was greatly simplified by modifying the form of the non-dimensional solution curve central to the original *Yura* theory (Figure 1.5). The specification substitutes straight lines for the non-dimensional solution curves of *Yura*. The inclusion of straight lines greatly simplifies the calculation of failure load and adds conservatism to the calculated values. A schematic plot of the design equation is shown in Figure 1.6 and the derivation of the specification equations and presentation of the assumptions made are presented in Appendix A.

1.5   The Summers Investigation

In lieu of full scale tests, *Summers* (1982) conducted a parametric study using acrylic models and finite element analysis. The model beams were simply supported and point loaded under load control at their mid-spans. Summers noted that creep was present at the stress levels reached in the tests.

The BASP (Buckling Analysis of Stiffened Plates) finite element program (Akay, H.U., et al., 1977) was used to compare to each of the model tests and analyze the results of previous full scale tests by *Costley* (1970) demonstrating the tension flange movement mode. The program was also used to conduct parametric studies of the tension flange movement mode. The BASP program is discussed in some detail in Chapter 3.

1.5.1   Parametric Study

The parametric study consisted of 64 finite element analyses. *Summers* varied length, lateral and torsional restraint and all aspects of cross-section dimensions for his parametric study. In one problem series of particular interest he varied the lateral stiffness of the tension flange while keeping flange area constant. The neutral axis of the section remained constant and the moment of inertia about that axis was nearly constant. The maximum tension flange lateral stiffness, defined by a mid-span lateral point load, was 84 times the minimum lateral stiffness. According to *Yura* theory, the lateral stiffness of the tension flange is a significant factor in determining buckling load. Changes in flange stiffness of this magnitude should affect a two or three fold increase in the buckling strength of the system. With this large range of lateral stiffnesses, only a 7 percent change was noted in the resulting buckling loads. Similar changes to

the lateral stiffness of the compression flange were made but had no effect on the tension flange movement load. This provides some insight into the flexural behaviour of the modified sections and indicates that lateral tension flange stiffness may not be as significant a variable in determining lateral tension flange movement buckling load as originally expected.

1.5.2   Model Testing

Three model test specimens were constructed. The first model test specimen was designed to be a preliminary investigation of lateral tension flange movement. The second and third models were of identical cross section but differed in the amount of out-of-plane initial tension flange deflection. The second model was considered initially perfect while the third model had a 0.76 mm initial out-of-plane mid-span deflection over a 610 mm span (L/800). The presence of out-of-straightness reduced the measured buckling load of the third specimen to 30% of the value for the initially perfect specimen. All three specimens failed in the tension flange movement failure mode.

After the model testing, the BASP program was used to analyze the results of the full scale tests by Costley and the model tests. Output from BASP analysis of full scale tests showed distinct buckled shapes peculiar to the tension flange movement failure mode, but data was not sufficient from the full scale tests to conduct proper comparisons. It would be unrealistic to compare the full scale tests to BASP output since BASP is an elastic analysis program while in all but one instance, the failures of full scale tests were highly inelastic. *Summers* model tests were arguably inelastic because of the presence of creep in the specimens. This inelasticity was apparently not sufficient to greatly effect the failure load of the

test beams since BASP elastic analysis gives good agreement with the experimental buckling loads from the model tests.

Finite element analysis was also used to investigate the vertical web stress distribution below the load point. Parameters such as flange thickness, bearing length and presence of a fillet were not varied in the analysis. The results differed significantly from the triangular stress distribution assumed in the *Yura* and *Basler* theory. The new stress distribution was included in the revised *Yura* theory, described in the next section.

1.6   The Revised Yura Theory

The results of *Summers* work were additional to, and refinements of the *Yura* theory. The *Yura* theory ignored the torsional stiffness of the top and bottom flange and finite element analysis results revealed some discrepancy between assumed web vertical stress distributions and analytical results. The addition of the torsional restraints and modification of the assumed vertical stress distribution result in the model shown in Figure 1.7.

Although this solution is a refinement to the original *Yura* Theory, the current AISC Sidesway Buckling Provision is a codification of the original *Yura* Theory and does not consider the modified stress distribution below the load or the rotational restraint of the flanges.

1.7   Scope of Work

To date, few tests have been conducted to explore the tension flange movement failure mode. Current theories and code equations are, therefore, untested.

This work attempted to add to the body of tension flange movement test data and further understanding of the tension flange movement failure mode. Finite element modelling, model tests and full scale tests were used to add to existing data. The model tests provided buckling loads and qualitative observation of buckled shapes. To avoid some potential problems encountered with previous model test series (*Summers* 1982), tests were conducted using a material less susceptible to creep, a test frame with less internal friction and stroke control loading to allow static loading, observations in the post-buckling region and better control near the buckling load.

Full scale tests designed specifically to explore this phenomenon were conducted. Buckled shapes, local stress distributions below the concentrated load, boundary conditions and material properties were all reported for these tests. Data collected from this and previous work were assembled to form a comprehensive sample of specimen behaviour; specifically failure loads, loss of vertical stiffness and ductility in the post buckling range. Finite element modelling and existing code equations were compared to the test data to determine their applicability. The failure loads observed in the full scale tests were compared to code predictions for the same systems to determine the degree of capacity loss in susceptible structures. A more comprehensive predictive model was formulated and presented for comparison with test results. Recommendations were made for further research.

1.8 Outline of Thesis

Chapter 1 provides a brief history of research conducted on the tension flange movement failure mode and describes theories put forward to explain the phenomenon.

Chapter 2 describes the apparatus, procedure and results of the styrene model test series.

Chapter 3 provides details of finite element modelling, model test data analysis and the development of an interaction equation for prediction of tension flange movement failure load.

Full scale test apparatus, material properties, preparation, test procedure and measurement devices are presented in Chapter 4.

Full scale tests results including in-plane behaviour, out-of-plane behaviour, web strains, in-plane moments, web deflections and end moments are presented for all full scale tests in chapter 5. Specimen behaviour is explained.

Chapter 6 presents full scale, styrene model and previous test results and compares them to finite element, design and interaction equation predictive models. Each prediction method is critically evaluated.

Chapter 7 summarizes observations made during testing and analysis. Based on the observations, conclusions are made about the behaviour of test specimens and the accuracy of the predictive models. Recommendations are made for future research.
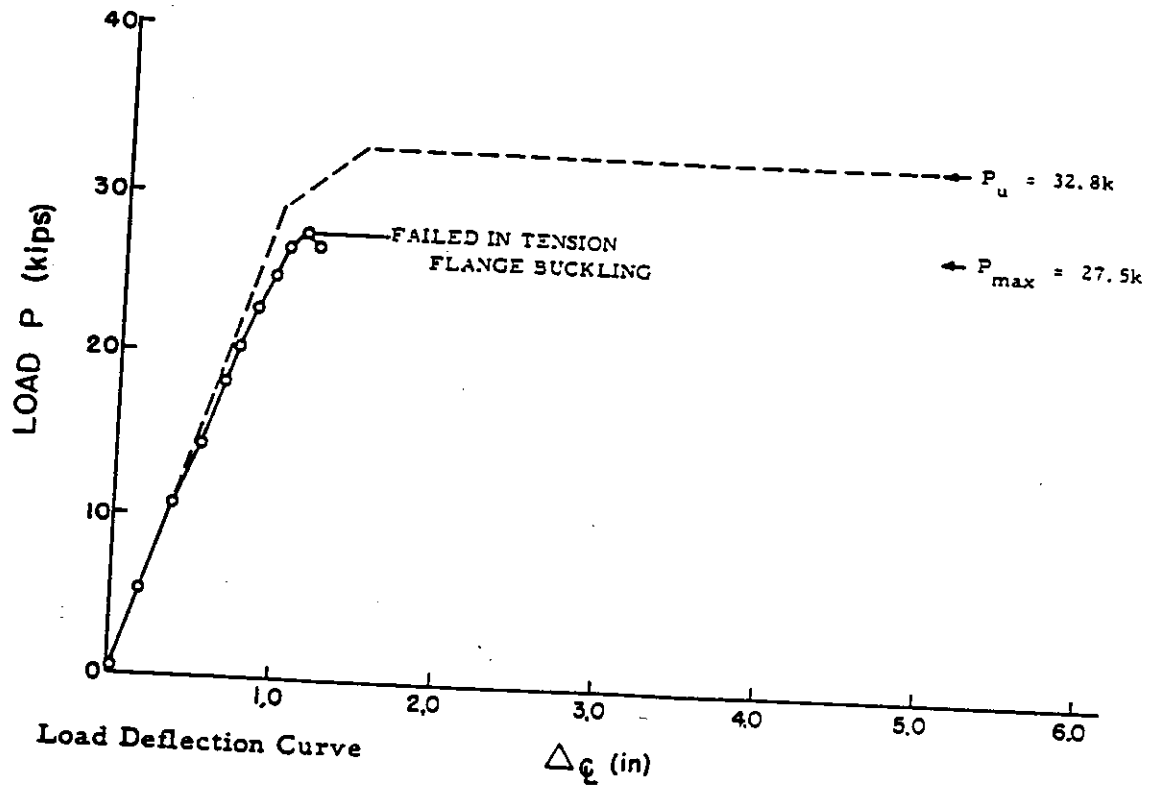
Figure 1.1
Load versus in-plane mid-span
deflection of observed tension flange movement failure
University of Texas test
(Taken from *Costley*, 1970)
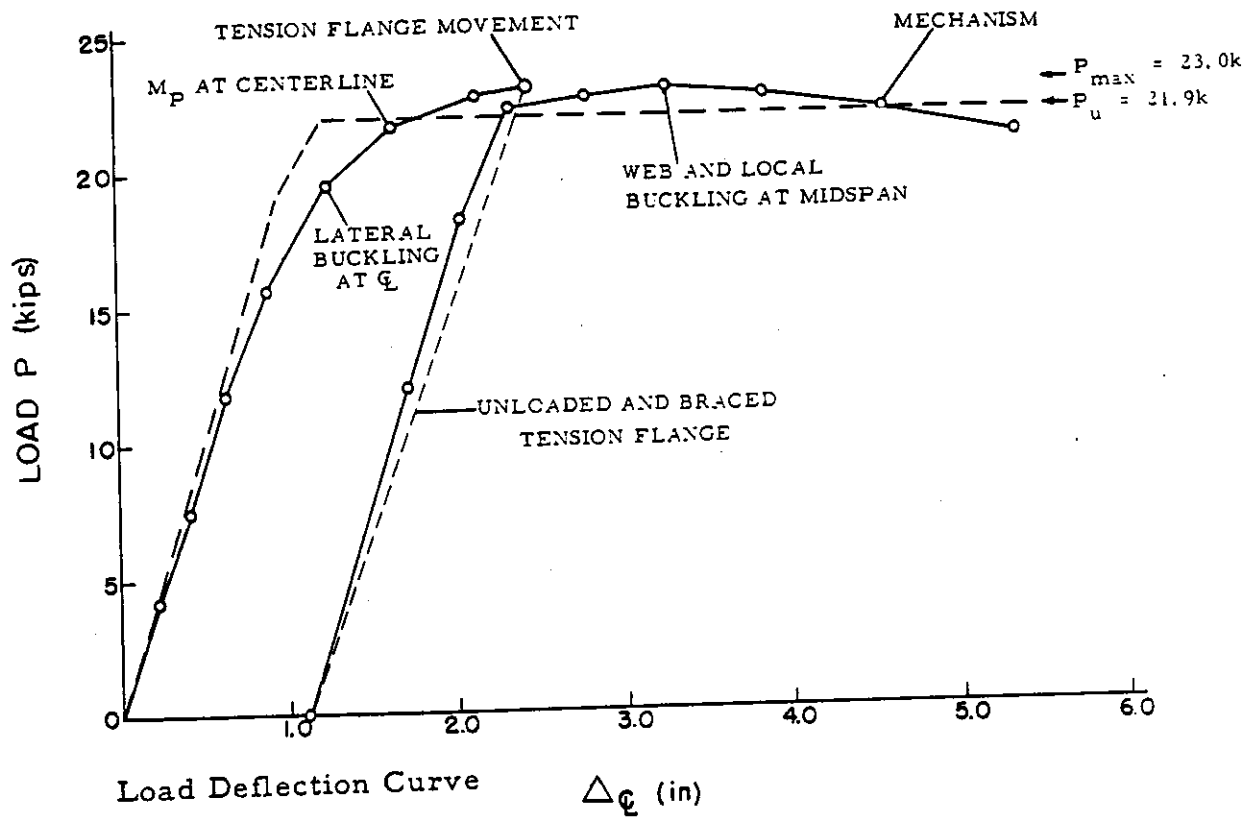
Figure 1.2
Load versus in-plane mid-span
deflection of suppressed tension flange movement
University of Texas test
(Taken from *Costley*, 1970)
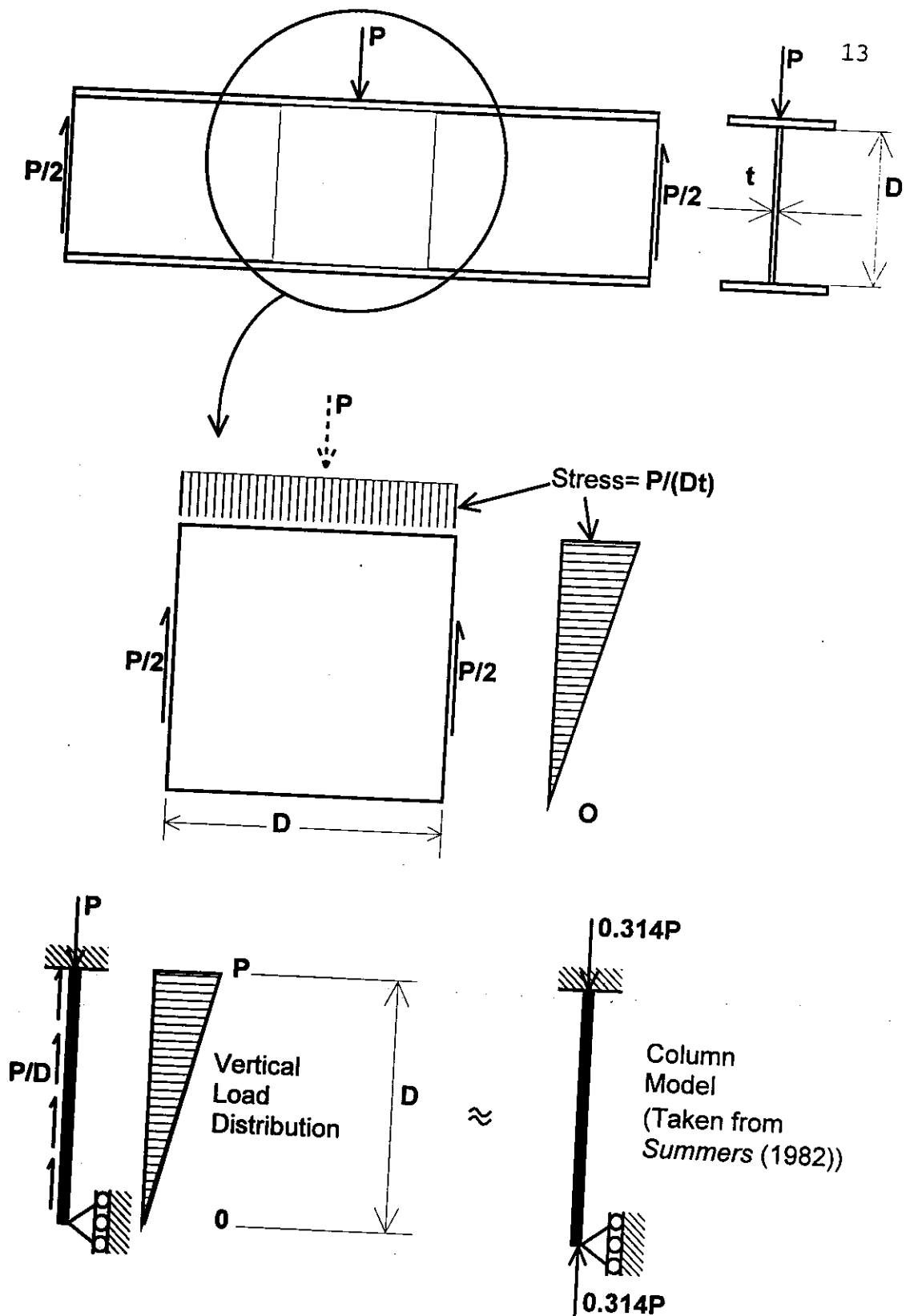
Figure 1.3
Basler theory assumptions
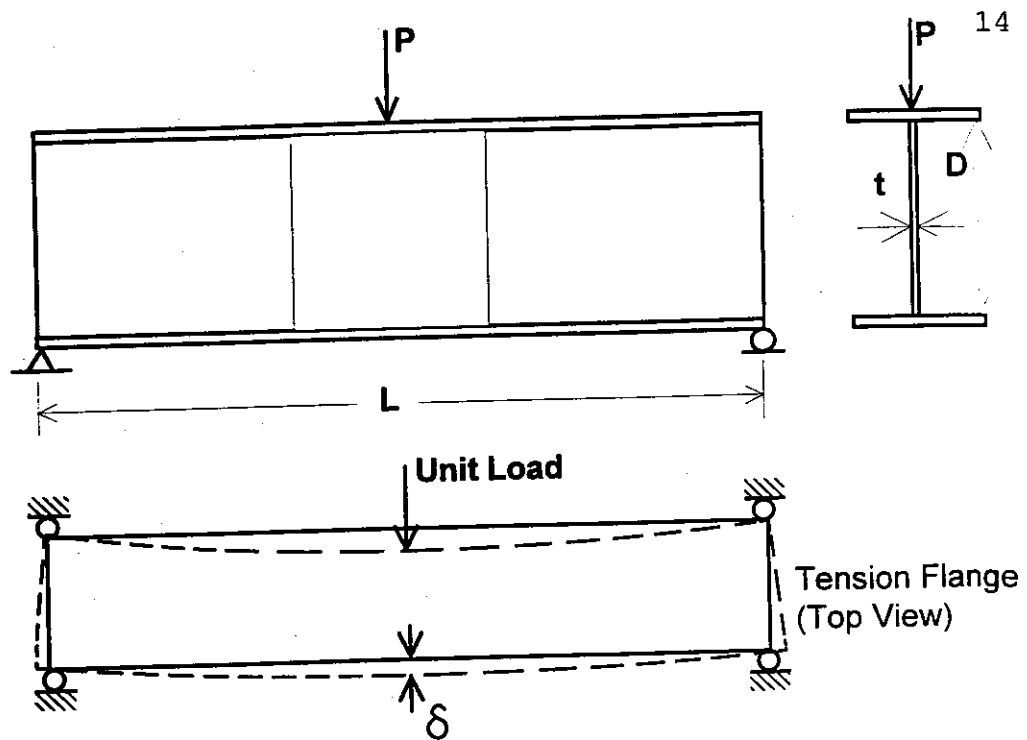
$$\text{Stifffness of the tension flange, } k = \frac{1}{\delta} = \frac{48EI_f}{L^3}$$
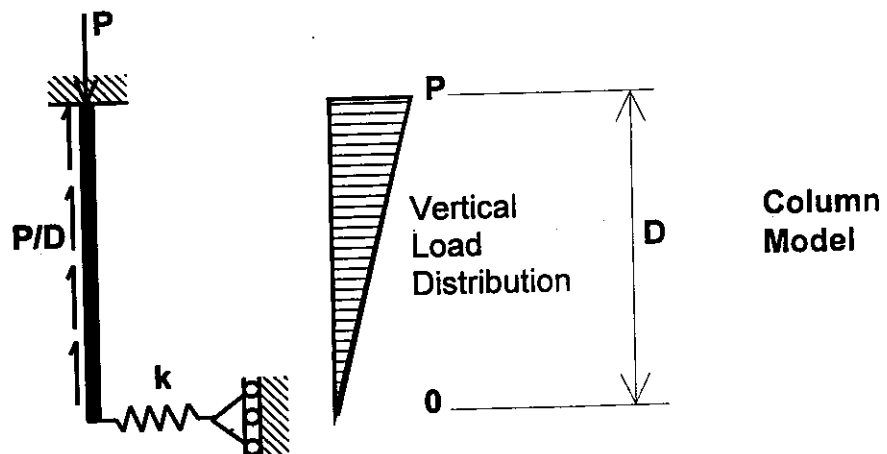
Figure 1.4
Yura theory assumptions
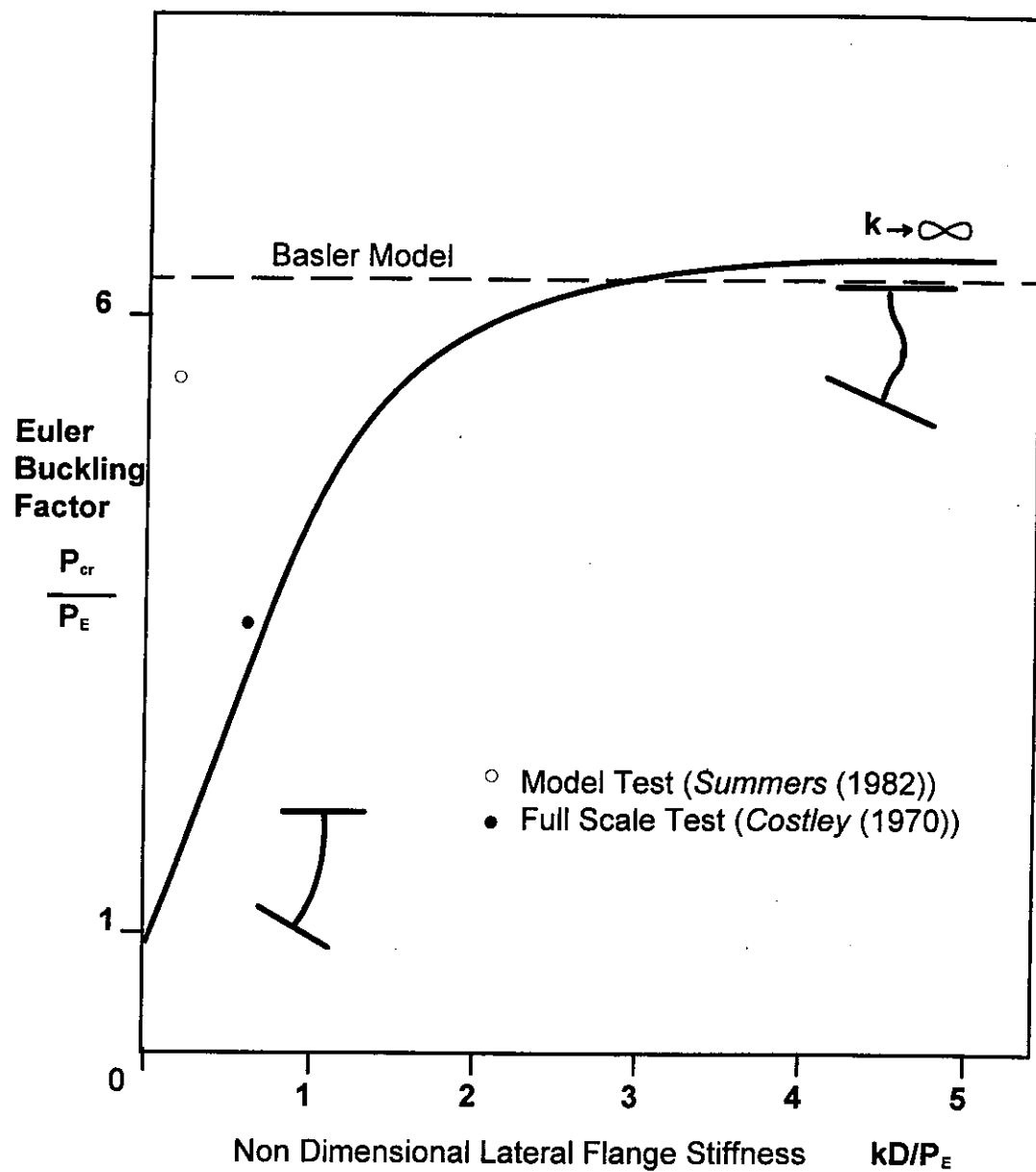
Figure 1.5
Non Dimensional Plot
for Solution of Yura Theory
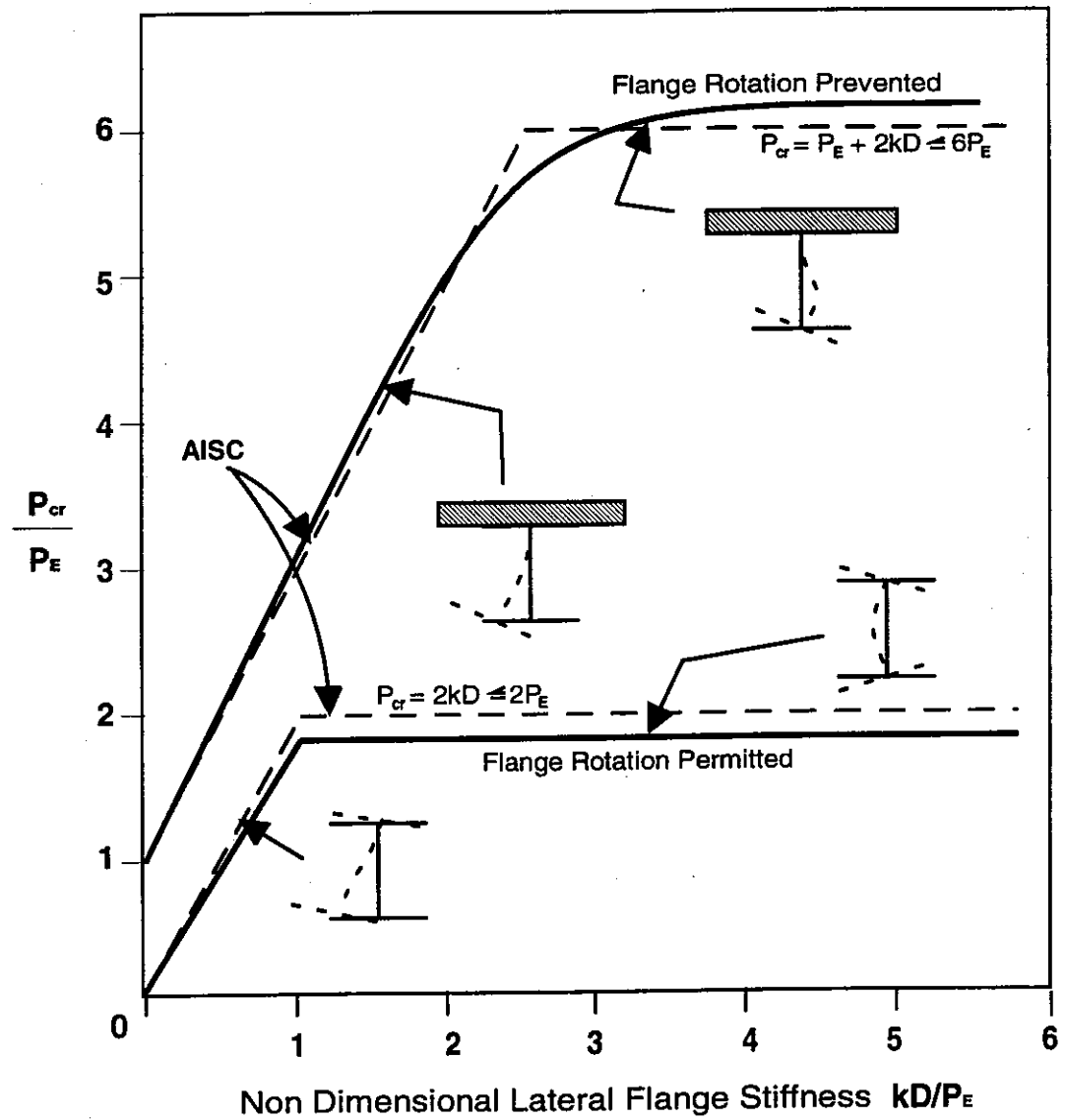
Figure 1.6
Non Dimensional Plot
for Solution of Yura Theory
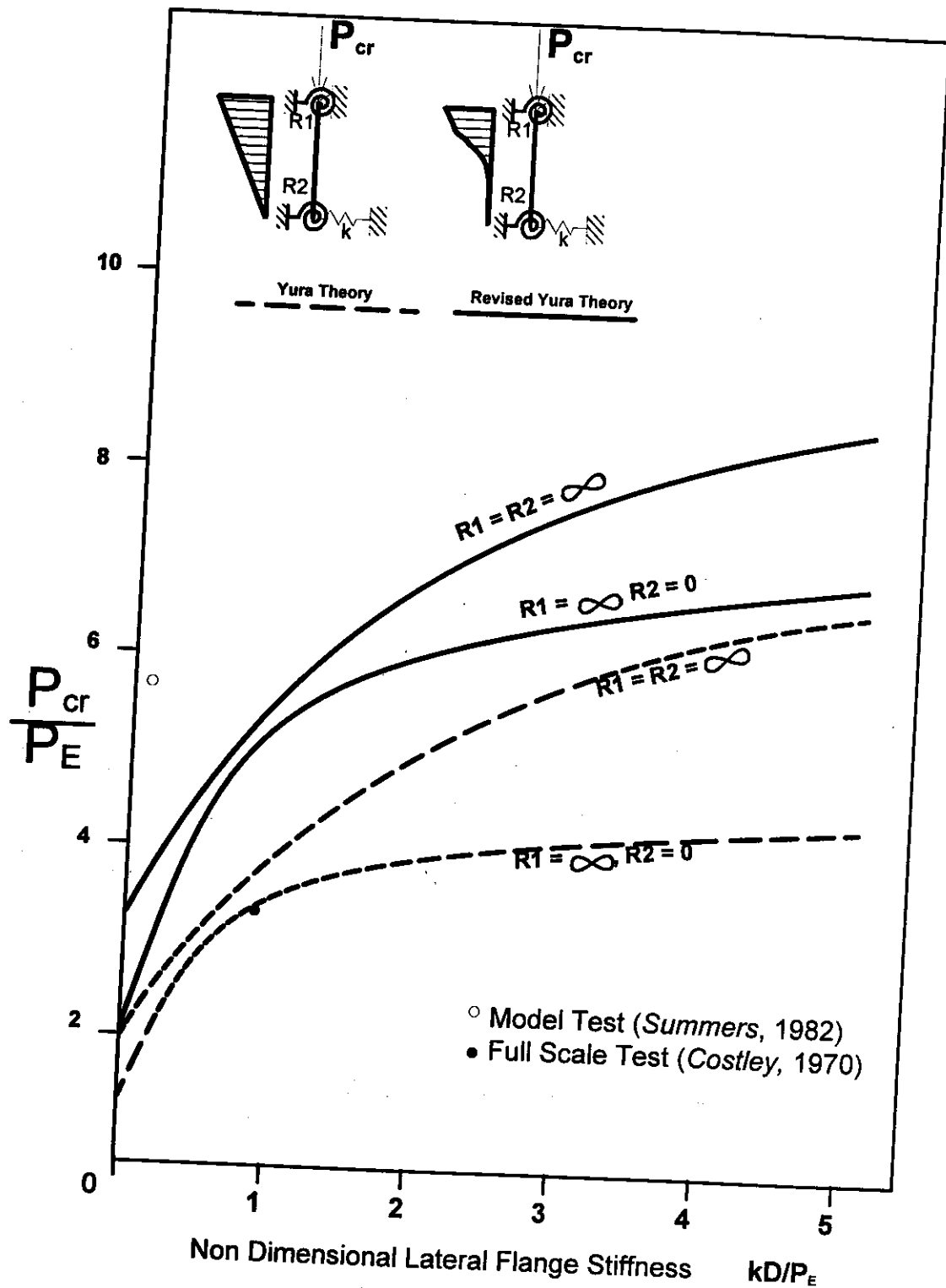
Figure 1.7
Non Dimensional Plot
for Solution of Yura Theory
and Revised Yura Theory

2. MODEL TESTING

2.1 General

Since little investigation of the phenomenon of tension flange movement buckling has been done, the initial stages of this research were done using scale model tests. The use of scale model tests allows reduction of test set up time and more control of cross-sectional dimensions than full scale testing and is much less costly.

During *Summers*(1982) tests on acrylic beams, creep was detected in the model specimens during testing. In an attempt to ensure elastic model tests, a different material was required. Styrene, an opaque white thermoplastic, is linear elastic, brittle and does not creep at high stress levels and was selected as the material for the model tests.

Styrene scale models were used to conduct a parametric study of the effect of varying flange dimensions on failure load. All test beams were of doubly symmetric cross-section and nine different flange sized beams were tested. The specimens were all 611 mm in length and simply supported at both ends. End bearing points were vertically stiffened to one half the web depth. Discrete bracings were provided at the top flange quarter points and the beams were loaded at the mid-span.

2.2 Specimens

Model beams were constructed by laminating 0.5 mm thick styrene sheets to build up the desired thickness of material. A total of eleven specimens were

constructed, as described in Chapter 4, and their nominal dimensions are provided in Table 2.1. Specimens P1 and P2 were used to proof test the testing apparatus and fabrication technique. The other nine specimens were used to conduct the parametric study. Finite element analyses done for the selection of the P2 specimen revealed that styrene beams with web depth to thickness ratios between 45 and 55 were particularly susceptible to tension flange movement failure for a wide range of flange sizes. Parametric series beam web depth to thickness ratios ranged between 48.4 and 49.4. Web thickness and flange centre to centre depth were both constant for all parametric test beams. Three different flange widths were combined with three different flange thicknesses to provide 9 different sets of flange dimensions.

After completing the tests of specimens P1 and P2, three specimens were constructed (A, B and C) each with the maximum flange width (b = 31.8 mm) and one of the three flange thicknesses (t_f = 2.5 mm, t_f = 2.0 mm, t_f = 1.5 mm). After each test, the specimens were measured to detect any residual deformations from testing. If the specimens behaved elastically during the previous test, the flanges were then cut to reduce flange widths to b = 25.4 mm (specimens D, E and F) and finally b = 19.1 mm (specimens G, H and I) for further testing. In all cases, specimens exhibited no residual deformations and were modified for further testing.

To suppress the buckling of the web at support locations, web stiffeners were applied to the beams for each test. Stiffeners were simply a single laminate of styrene (t = 0.5 mm) glued flat to the ends of the specimen, using a solvent type adhesive. The stiffeners were removed from the specimens for cutting of flange tip material between tests and new stiffeners were applied for testing. No web buckling above supports was noted through the entire parametric test program.

2.3 Material Properties

2.3.1 Apparatus

Accurate determination of the material properties of the styrene used for model test specimens was of extreme importance for the success of the model test program. Styrene is a thermoplastic and has a very low Young's Modulus and tensile strength when compared to steel and concrete. Further, the cross-sectional area of all coupons was less than 100 mm². This combination of small cross section and low strength prohibit the use of test machines designed for testing of relatively large steel and concrete specimens in the testing of styrene coupons. A test frame was constructed using a hollow structural section (HSS 76 x 51 x 3.8 mm) as the main member of the load frame. Two members extended from the ends of the hollow structural section at 90° to its' axis to create a bent as shown schematically in Figure 2.1. Test coupons were clamped in end fittings which, in turn, were pinned to the fixed and moving ends of the system. The fixed end was attached to the loading frame by a pin ended tension rod. The moving end included a proving ring for load measurement and a threaded actuator rod to impose strain on the system. Coupon strain was measured using a dial gauge extensometer that clamped on the coupon.

2.3.2 Test Procedure

To address a possible effect of lamination on material properties, both virgin and laminated specimens were tested. Laminated specimens were fabricated by placing the lower laminate on a flat smooth surface and applying a solvent type adhesive over the entire upper surface of the lower laminate. The upper laminate was then placed on the lower, slowly moving from one end to the other. Full

contact between laminates and removal of air bubbles and wrinkles was ensured. A smooth flat plate was then placed on top of the assembly and weighted to provide approximately 1 kg/cm^2 of clamping pressure. The assembly was allowed to cure for one day. If further laminates were needed, they were applied to the built up styrene following the same procedure.

Coupons were cut from the stock material (0.5 mm thick styrene sheet) or laminated sheets by hand using a utility knife and straight edge. The edges of the coupons were smoothed by wet sanding to remove any surface imperfections that could lead to premature fracture of the specimens. The specimen dimensions are shown in Figure 2.2. One specimen, 50 mm wide by 0.5 mm thick was tested to determine if there was a size effect in coupon tests.

Two coupons were cut at right angles to the orientation of all other coupons to detect any possible anisotropy in the source material. No lamination was done on these specimens.

A zero load reading was taken from the load ring before the specimen was clamped in the frame. Since the loading system requires catenary forces to exist within the specimen, the catenary forces would be present as error in the failure load of the coupon if the zero load reading was taken after insertion of the specimen. Loading of the specimen proceeded to a preload of about 10% of the predicted ultimate load. The dial gauge extensometer was clamped to the specimen over a gauge length of 102 m and load and zero strain readings were taken. The specimen was loaded in increments of 5% of the predicted ultimate load. It was not necessary to allow time for creep to occur since it was not observed until stresses exceeded 95% of the fracture stress. Load and strain readings were taken at each data point and the test was continued at the prescribed load rate until

fracture of the coupon. In all cases specimens behaved linearly until fracture. Eight of the ten coupons failed near the center of the coupon while two failed closer to the ends of the narrowest portion of the coupon. No coupons failed as a result of stress concentrations at locations of coupon width changes.

2.3.3 Results

All coupons exhibited similar behaviour when loaded. Stress-strain relationships were linear-elastic until fracture of the specimens. Specimen width, lamination and orientation had no effect on the measured properties of the coupons. The results of all the coupon tests and published expectations for the material are shown in Table 2.2.

2.4 Model Test Apparatus

The model test apparatus consisted of a base plate, restraint frames, load frame, loading system and supports. It was designed to be a self equilibrating loading system. Each component will be described in detail below. The assembly is shown schematically in Figure 2.3 and photographically in Figure 2.4. All components were constructed using ACRYLITE™, a transparent industrial acrylic. The material was selected because it did not obscure photographs of test specimens and was available in 3 m and 6 m thicknesses, capable if sustaining loads well in excess of the test maximum loads.

The base plate was a longitudinal-rib-stiffened plate designed to resist the lateral and flexural loads imposed on it by the test specimen. The base plate was a 210 x 1200 x 6 m thick top flange with three 40 x 6 m thick rib stiffeners extending the full length of the plate along its centerline and each edge. Two 800

x 5 m longitudinal slots were cut through the plate flange at 55 m from the plate centerline. The slots accepted bolts from the outer frames of the restraint and load frames and allowed the frames to be positioned anywhere along the slot length. A detailed drawing of the base plate is shown in Figure 2.5.

The restraint frame was an assembly of an outer frame and an inner frame. The outer frame comprises two vertical guides and a base. The outer frame base bolted to the base plate via four holes, placed at the corners of a 110 x 30 m rectangle. The 110 m hole spacing corresponds to the distance between the slots of the base plate. The two guides extended vertically upwards from the outer frame base. They were 141.5 m apart and symmetrical about the base plate centerline. The inner face of each guide had a 3 x 6 m wide vertical groove to accept the deep groove ball bearings of the inner frame. The inner frame was 134.5 m wide and 70 m high with one deep groove ball bearing at each corner. This frame translated vertically inside the outer frame and was restrained from movement and rotation in all other directions. To allow other degrees of freedom to the top flange of the test beam, selected degrees of freedom were released by bearings included in the inner restraint frame. Longitudinal restraint and in-plane rotation restraint of the beam top flange were released through translation bearings and a pin connection as shown in Figure 2.6. The inner loading frame was used as the only longitudinal support for the test specimen and therefore did not include longitudinal translation bearings (see Figure 2.7).

Each end of the test specimen rested on a steel roller and smooth plate arrangement that allowed free rotation and longitudinal translation of the support.

Figure 2.8 is a schematic of the loading system, loading frame and specimen. The loading system imposed deflection on the model beam and

provided an instrument for measurement of the resulting internal force in the system. A lower distributing beam was positioned below the base plate and two threaded steel tension rods extended vertically upwards on both sides of the base plate from each side of the test specimen. The rods passed through holes in the ends of the top distributing beam and nuts were above the beam. Load was transferred to the inner loading frame through a proving ring bolted to the top distributing beam. As the nuts were turned down, deflection was imposed on the beam and the load passing through the proving ring could be measured. A photograph of the loading system is shown in Figure 2.9.

2.5   Model Test Procedure

Specimens were measured for mid-span out-of-straightness in the strong and weak direction prior to testing. Measurement was accomplished by simply supporting the specimen and measuring the position of the mid-span using a dial gauge (accurate to 0.001") (Specimens were then inverted and the process repeated). Prepared specimens were placed in the apparatus and the top flange was clamped to the appropriate restraint and load frames by tightening the clamp nuts finger tight. A zero load reading was taken from the proving ring and the proving ring/top distributing beam assembly was lowered into place. A zero deflection reading was taken (the distance between the top and bottom distributing beam). The loading progressed in 1 m increments of vertical deflection. A load and deflection reading were taken at each deflection increment. The test was halted when tension flange lateral deflection reached a level determined before the test or when a peak load was reached. The lateral tension flange movement stop criterion was determined by calculating the out-of-plane flange deflection corresponding to the flange tip reaching ultimate strain (assuming the flange deflected shape was a sinusoid). The test was stopped when the lateral deflection

of the bottom flange was one-half of the calculated deflection corresponding to flange tip ultimate strain.

After unloading, mid-span lateral and vertical deflections were once again measured and compared to measured pre-test values. Specimens with mid-span residual deflection of L/1000 (0.024") or less ware considered undeformed and were used for subsequent tests.

2.6   Model Test Results

As a proof test of the testing apparatus and fabrication technique, two beams were tested prior to the parametric series. The first was designed to fail in web buckling and was referred to as "P1". The specimen was fabricated and the test conducted using the same procedure used for the parametric series specimens (outlined in the previous section). As load was applied, the specimen exhibited elastic in-plane behaviour. No out-of-plane deflections were noted until a local web buckle formed abruptly below the load point at a load of 220 N. With increasing load beyond the formation of a web buckle, a reduction of the in-plane stiffness of the member and increasing out-of-plane deflection of the buckle were noted. The test was continued with some reduction of in-plane stiffness and at a load of 344.9 N, tension flange twist and lateral movement were noticed. Further reduction of in-plane stiffness was observed with increasing flange deformation. Loading was continued to 388.4 N, the ultimate load of the specimen, where excessive local web deformations and lateral flange movement limited the beams capacity. A load versus in-plane deflection curve for the test is shown in Figure 2.10. The results of the test were compared to theoretical predictions of load versus in-plane deflection to indicate whether the apparatus could provide accurate

results. Excellent agreement with in-plane stiffness predictions indicated that the system was capable of providing accurate test data.

The second test, "P2" was conducted to determine whether the tension flange movement buckling failure mode could be observed. A specimen was selected using finite element analysis as a source of determining the lowest energy buckling loads. Suitable test beams had predicted buckling loads less than predicted failure loads corresponding to web crippling and first yield in flexure. The load versus in-plane deflection curve for P2 is shown in Figure 2.11. The specimen displayed no visible out-of-plane deflections up to a load of 200 N. First observed out-of-plane deflection was a small bulge at the top of the web, directly below the load point. As loading continued, the web bulge increased in depth and width until it extended to one half the web depth. Further loading was accompanied by lateral tension flange movement and further widening of the web buckle. The test was halted at a load of 279.6 N due to excessive lateral deflection (one half flange width) of the tension flange. Results of this test agreed well with the predicted finite element failure load of 258.6 N and theoretical in-plane stiffness. As a result of the good agreement of this test with theoretical predictions, the parametric test series was begun.

After model beams P1 and P2 were tested, nine beams (A through I) were constructed and tested for a parametric study of the tension flange movement buckling mode. Model beam A showed no sign of out-of-plane deformation until reaching a load of approximately 440 N. At that load, the beam developed lateral tension flange deflections. The in-plane stiffness of the beam decreased very quickly with loading and a maximum load was reached at 466.1 N, as shown in Figure 2.12. Model tests B through I all behaved linearly in-plane at low load levels (up to 50% of the test maximum). At higher load levels, bottom flange

lateral deflections became more pronounced and were coupled with progressive reduction of in-plane stiffness with larger out-of-plane flange deformation (as shown in Figures 2.13 through 2.20). Peak loads were often observed as a plateau in the load versus in-plane deflection curves. Model beams F, H and I all experienced pronounced load plateaus as seen in Figures 2.17, 2.19 and 2.20.

Of the nine model tests conducted in the parametric series, only model test B was halted as a result of excessive deflections. All other tests reached a peak load. Load versus in-plane deflection curves are presented in figures 2.10 through 2.20. Included with each of the load versus in-plane deflection curves is a predicted elastic bending response for comparison. Table 2.3 summarizes the results of the model test program and includes AISC LRFD predicted failure loads and test to predicted ratios.

It can be seen from Table 2.3, that the AISC LRFD design equation provides conservative estimated of failure load. This can be explained by the omission of flange torsional stiffness and the assumption of a triangular vertical stress distribution below the load point. *Summers*(1982) suggested that both assumptions were conservative and would result in the AISC LRFD design equation providing conservative estimates of failure load.

Table 2.1

Model test specimen dimensions

Specimen	Cross Section				
	l (m)	b (m)	t_f (m)	d (m)	t_w (m)
P1	611	31.8	2.0	76.2	1.0
P2	611	31.8	1.5	49.3	1.0
A	611	31.8	2.5	48.4	1.0
B	611	31.8	2.0	48.9	1.0
C	611	31.8	1.5	49.4	1.0
D	611	25.4	2.5	48.4	1.0
E	611	25.4	2.0	48.9	1.0
F	611	25.4	1.5	49.4	1.0
G	611	19.1	2.5	48.4	1.0
H	611	19.1	2.0	48.9	1.0
I	611	19.1	1.5	49.4	1.0

l = beam length
t_w=web thickness
t_f=flange thickness
b=flange width
d=web depth

Note: Nominal dimensions are quoted. Actual dimension tolerances were:

$\pm$ 0.01 m for all thicknesses

$\pm$ 1 m for beam length

$\pm$ 0.05 m for all other dimensions

Table 2.2

Model coupon test results

Coupon Type	Laminates	Orientation (Degrees)	E (MPa)	F_u (MPa)
1	1	0	3167	16.5
1	1	0	3142	15.8
1	1	0	3247	16.7
1	2	0	3094	16.5
1	2	0	3093	15.9
1	3	0	3288	16.2
1	3	0	3135	16.0
1	1	90	3083	16.7
1	1	90	3157	17.0
2	1	0	3204	16.0
		Average	3161	16.3
		St. Dev.	68	0.41

*Quoted E =   3176 MPa
*Quoted Tensile Strength = 15.9 MPa

*Source: Handbook of Mathematical, Scientific, and Engineering
            Formulas, Tables, Functions , Graphs, Transforms (1991)

Table 2.3

Model Test Peak Loads

Beam	Test Peak (N)	AISC LRFD (N)	Test/Pred.
A	466.1	321.6	1.449
B	363.5	321.6	1.130
C	295.2	316.7	0.932
D	382.6	273.3	1.400
E	261.0	230.7	1.131
F	229.9	187.2	1.228
G	264.1	147.0	1.797
H	248.6	128.6	1.933
I	233.0	109.8	2.122
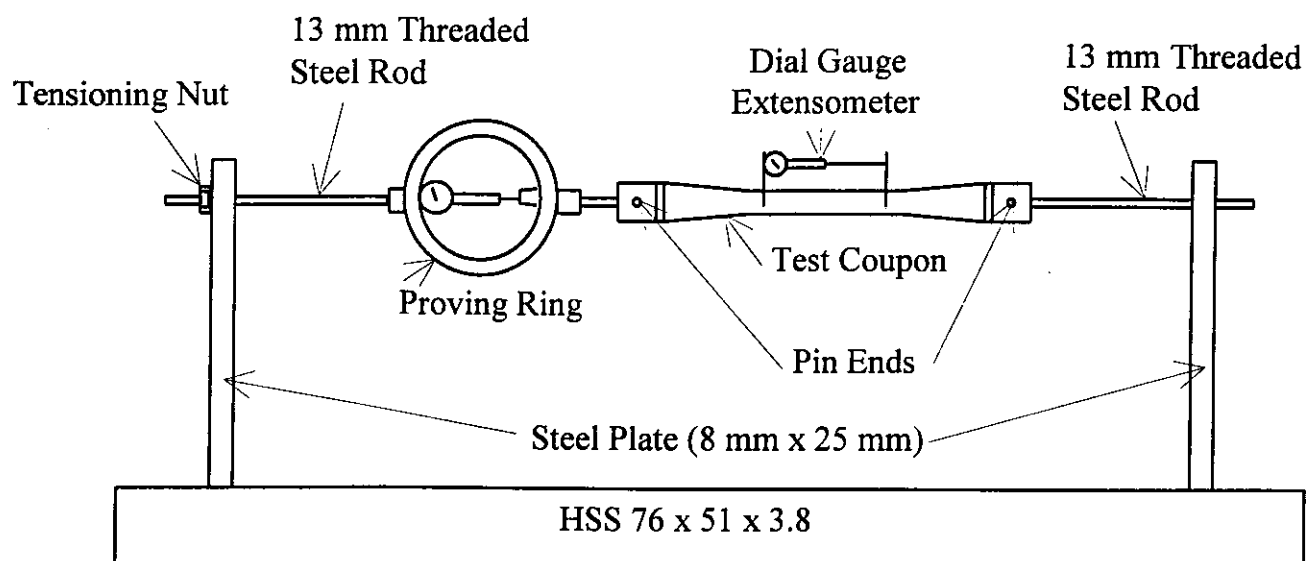
Figure 2.1 Schematic of Tension Test Setup
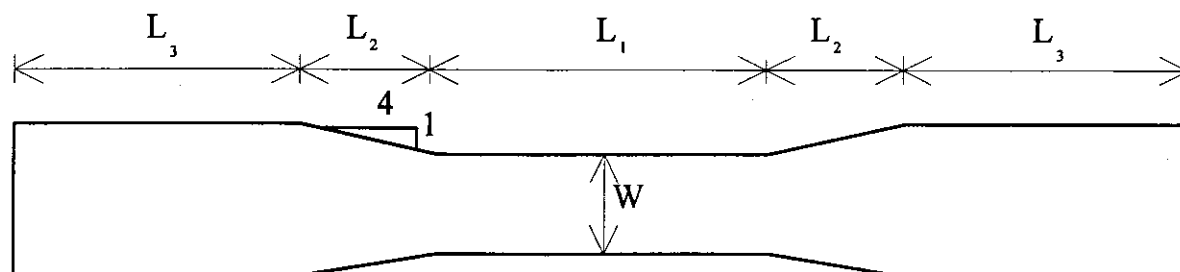
	L_3	L_2	L_1	W
COUPON TYPE 1	50.9	50.9	152.7	25.5
*COUPON TYPE 2	50.9	50.9	152.7	50.0

All dimensions in millimeters

* Only used for one test to determine if there was a size effect

Figure 2.2 Coupon Dimensions
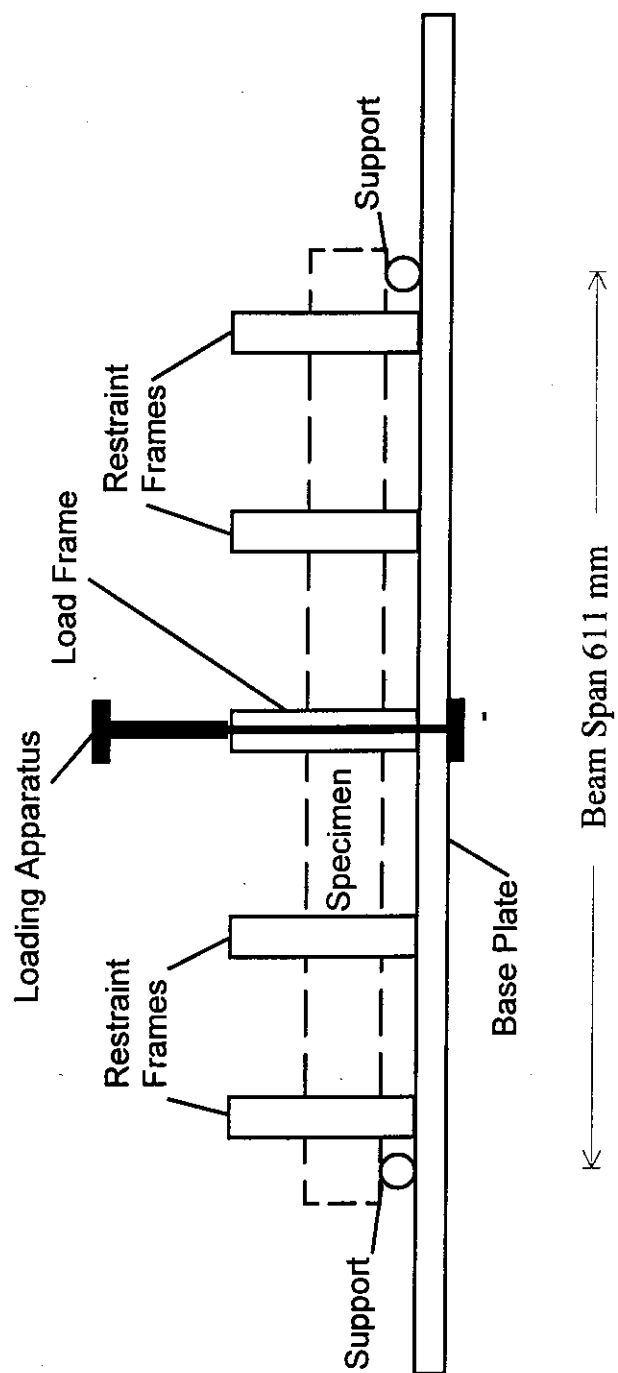
Figure 2.3
Schematic of Model Test Apparatus
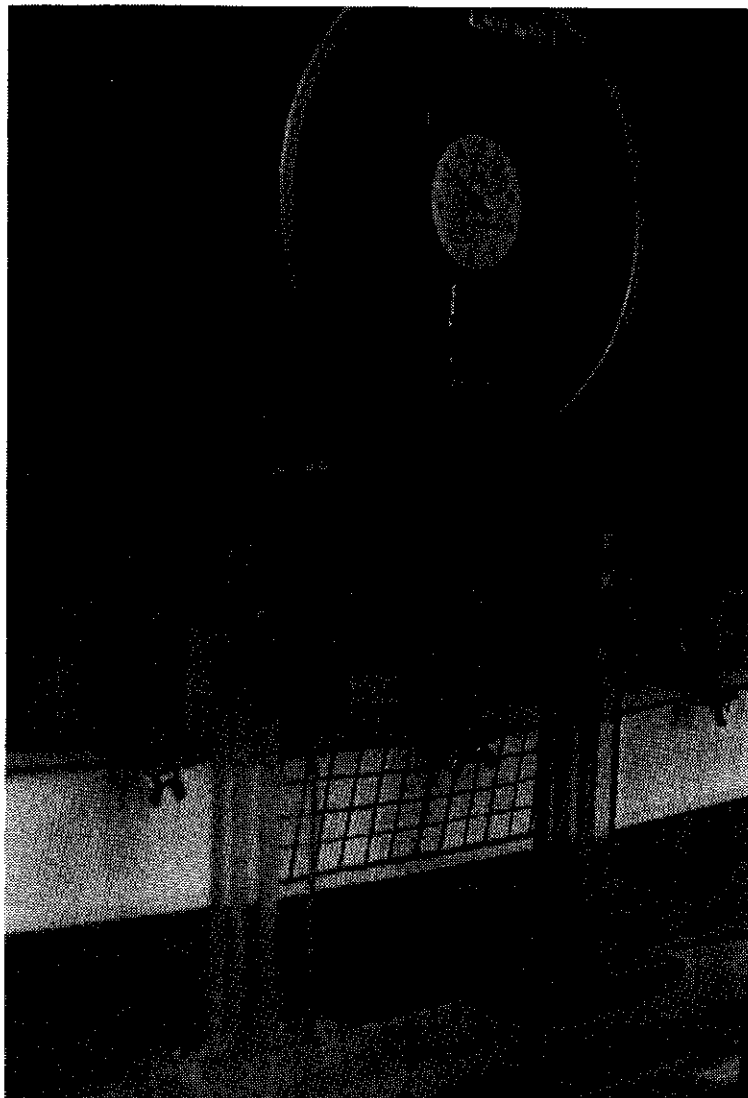
Figure 2.4
Model Test Apparatus

All dimensions in millimeters

6 mm
ACRYLITE
Sheet

Rib
Stiffeners

210

40

800

5

55

55

Slot

Slot

1200

Figure 2.5
Base Plate

Longitudinal Translation Bearing

Translation Bearing

Restraint Frame

Pin

Specimen

Specimen omitted for clarity
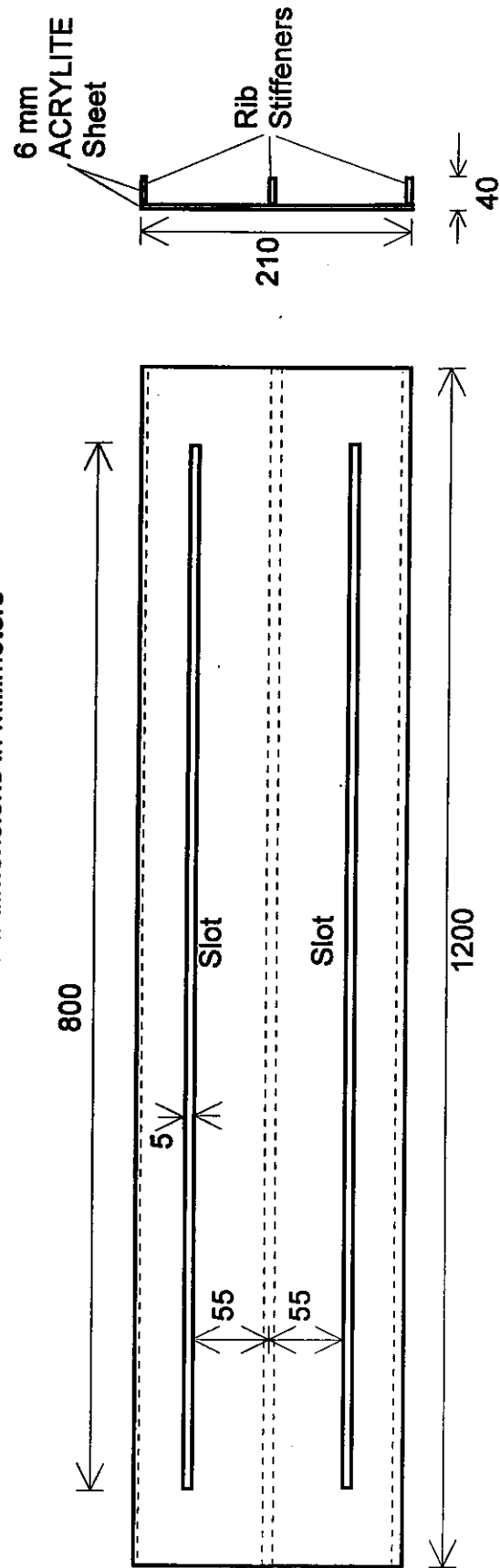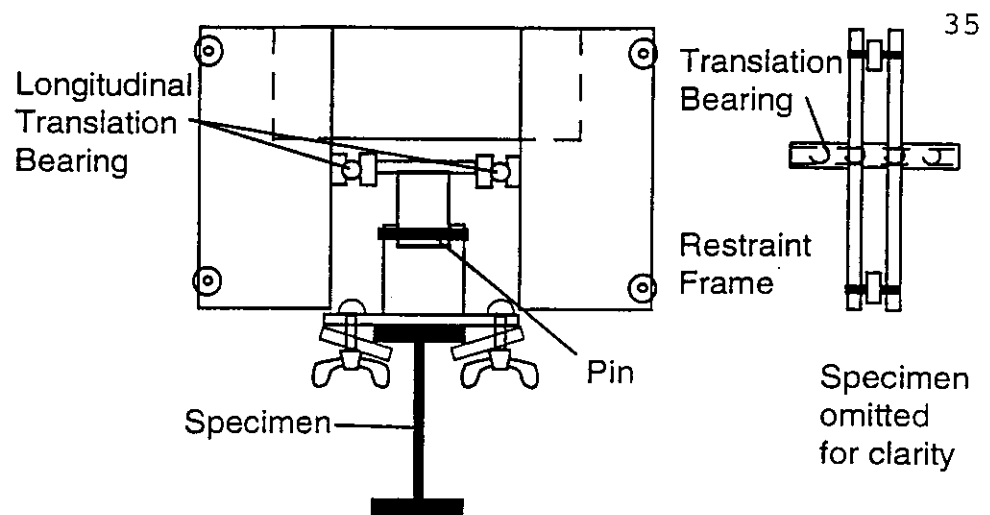
Figure 2.6
Model Test - Inner Restraint Frame

Deep Groove Ball Bearing

Load Frame

Pin

Specimen

Inner Frame
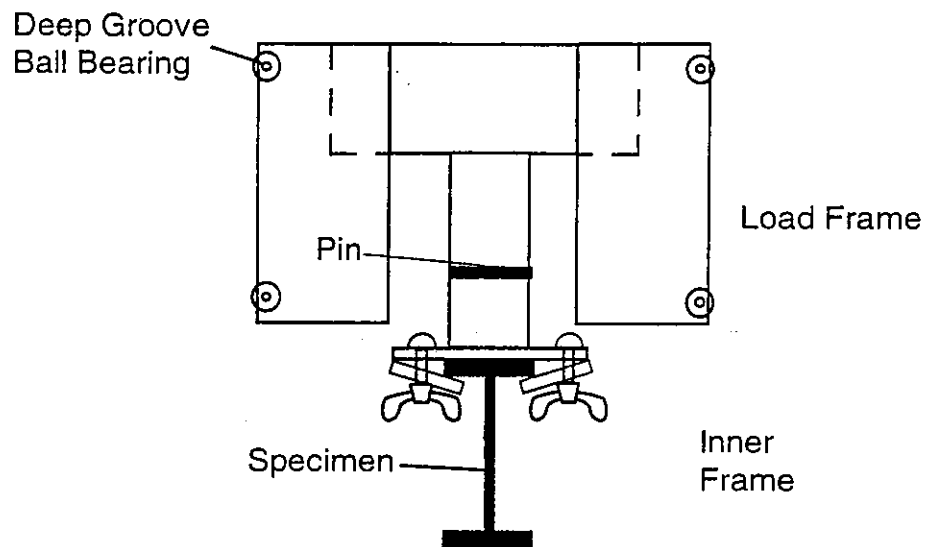
Figure 2.7
Model Test - Inner Load Frames

Load, P

Specimen

Base Plate

A

A

Top Distributing Beam

Tension Rod

Inner Frame

Specimen

Base Plate

Bottom Distributing Beam

Load, P

Section A-A
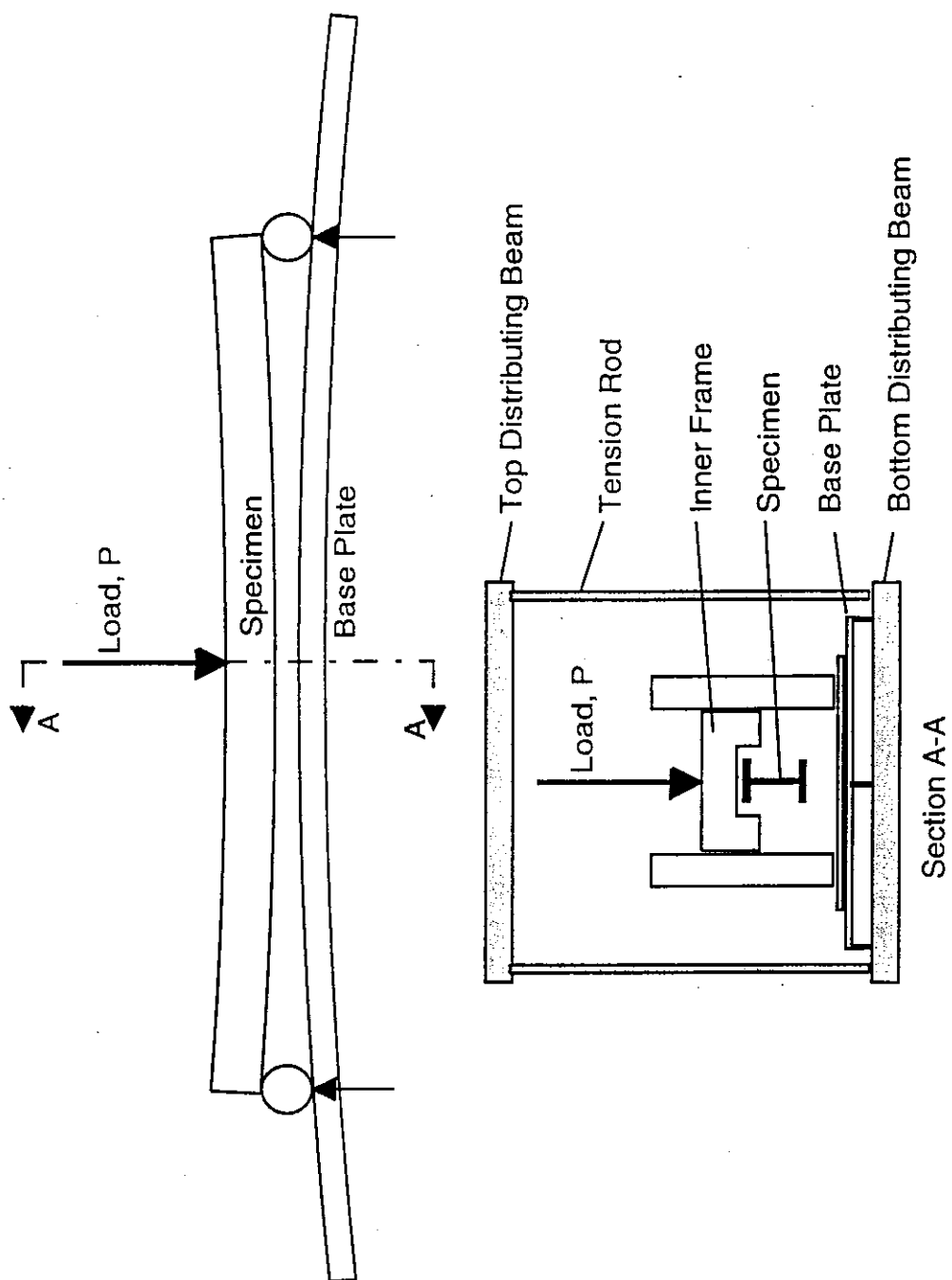
Figure 2.8
Loading System Schematic
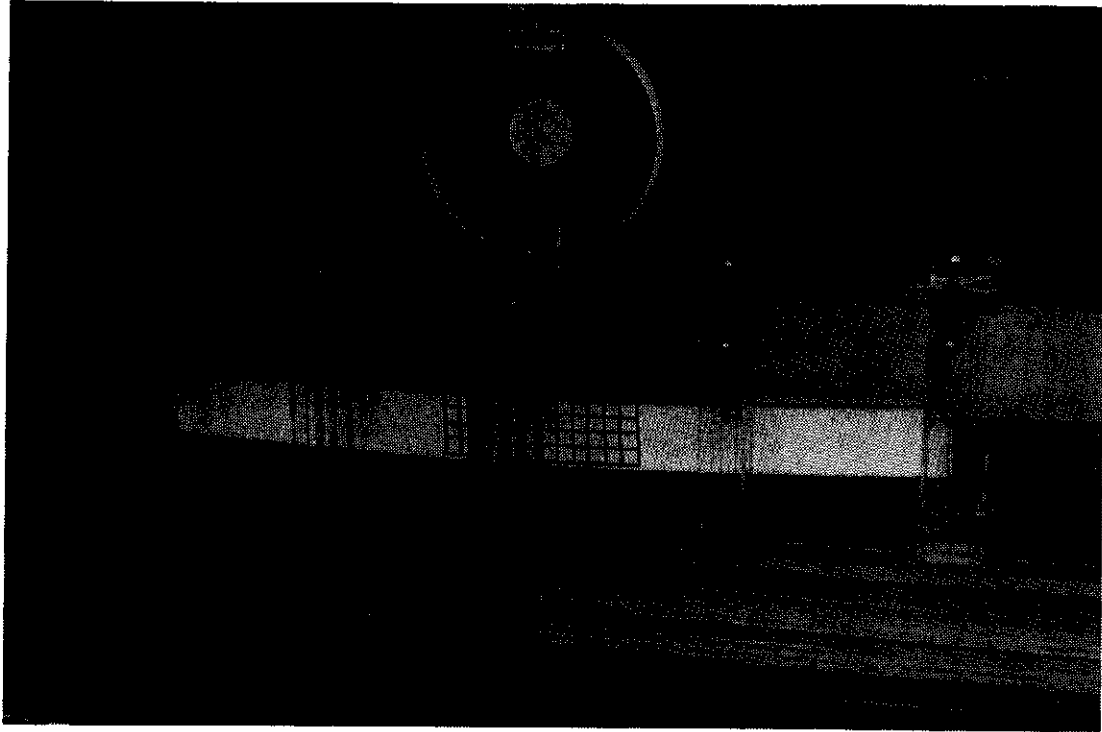
Figure 2.9
Model Test Loading System
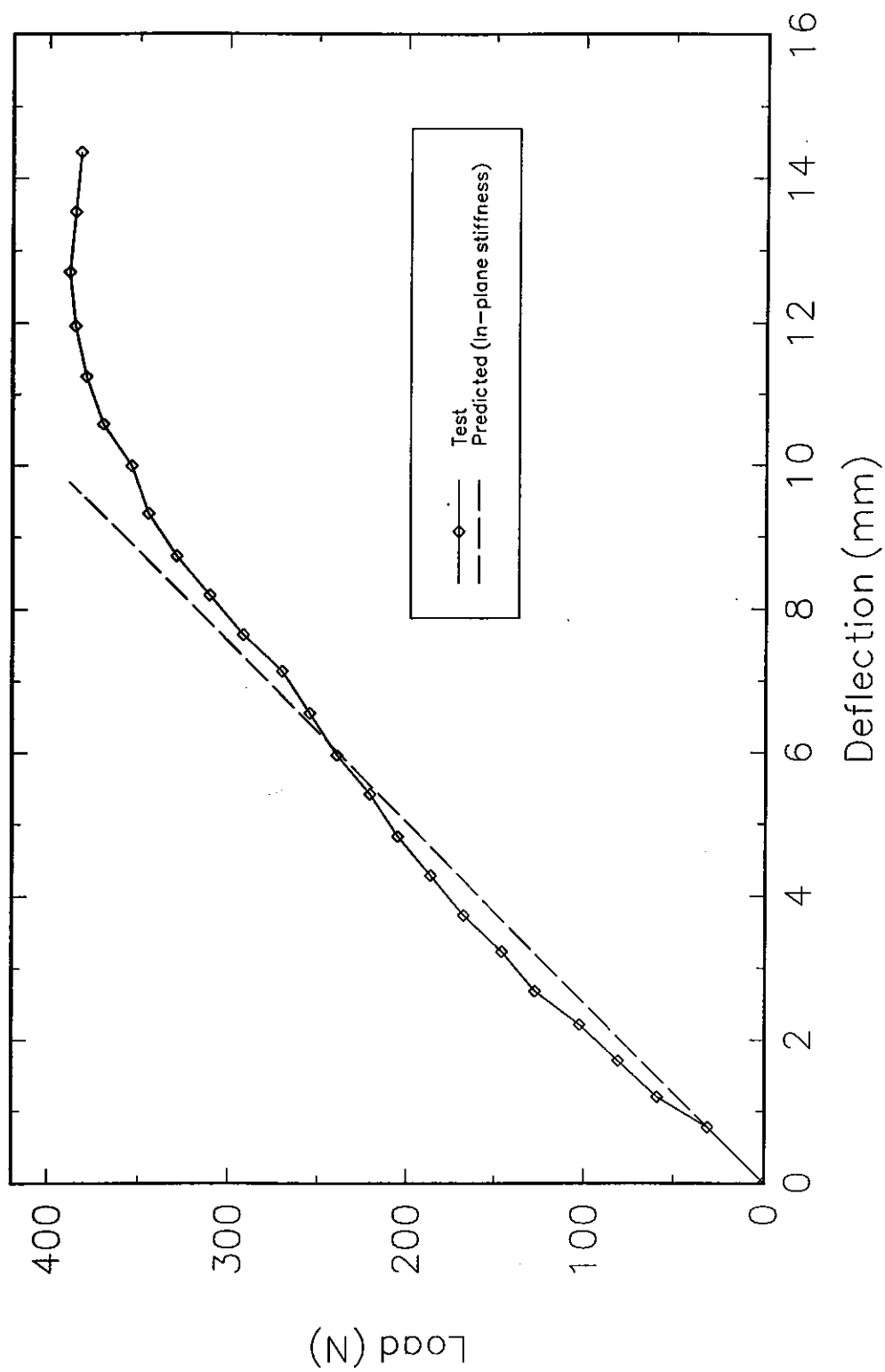
Figure 2.10
Load versus In-Plane Deflection
Model Beam P1
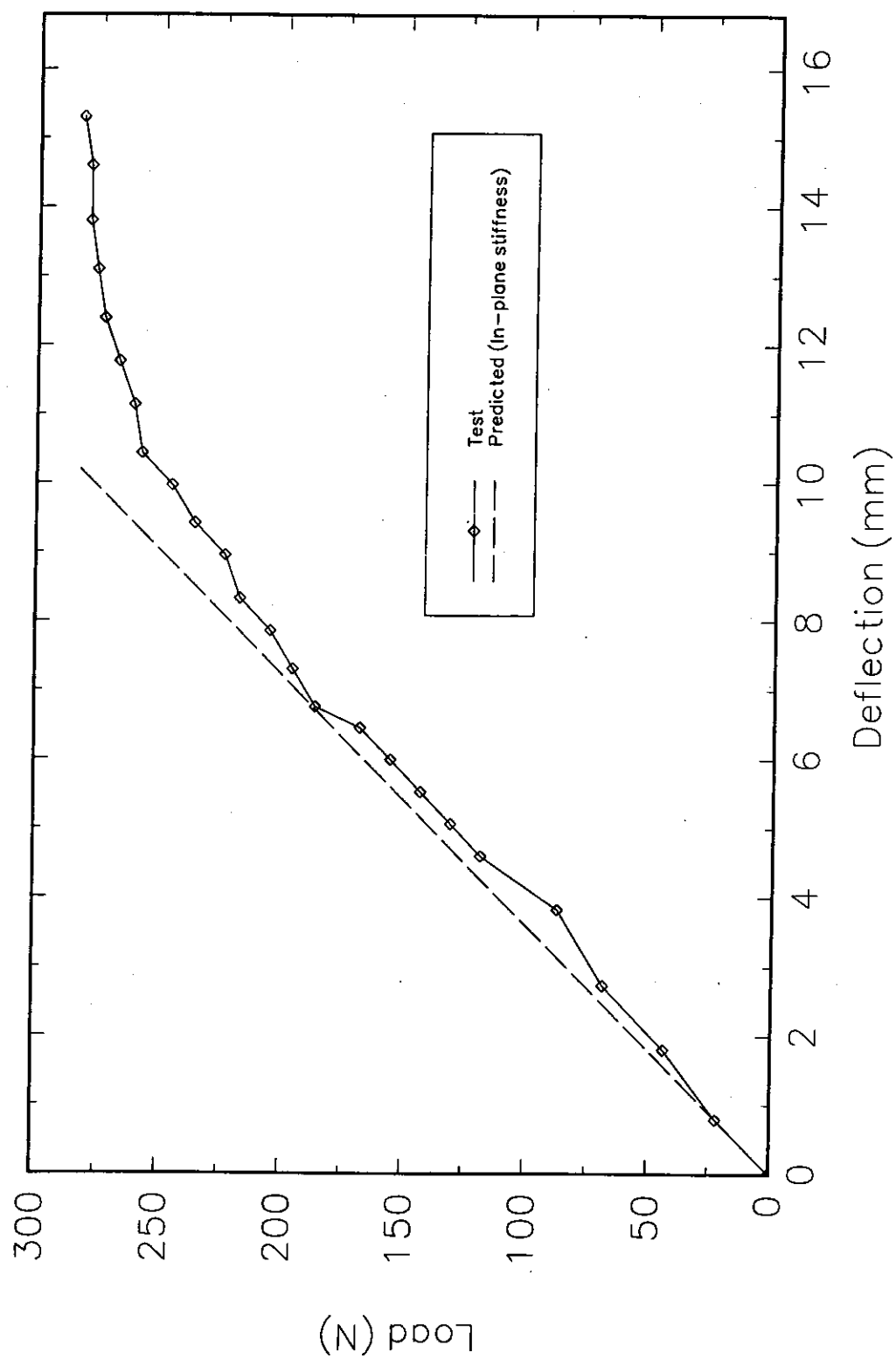
Figure 2.11
Load versus In-Plane Deflection
Model Beam P2
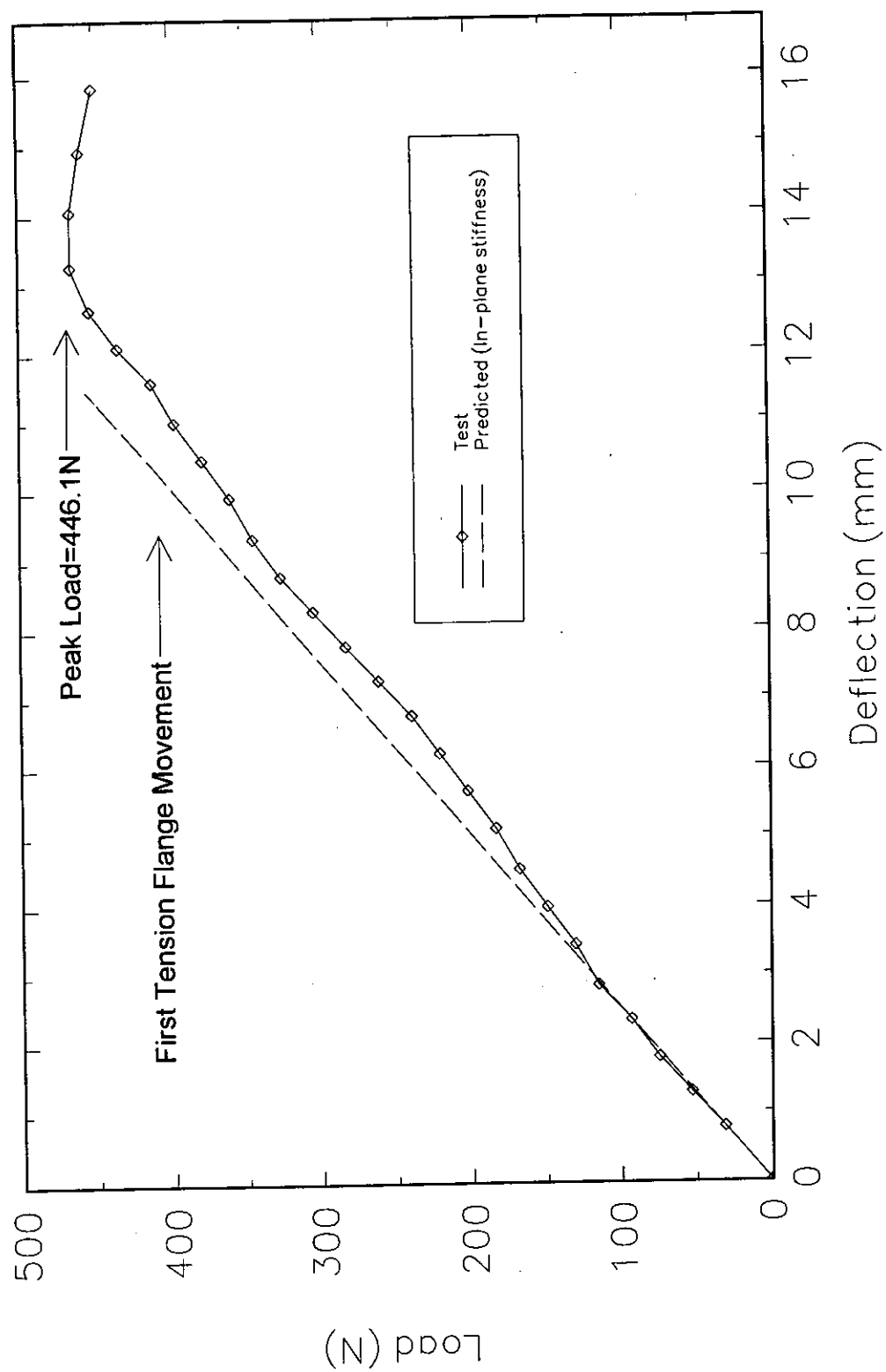
Figure 2.12
Load versus In-Plane Deflection
Model Beam A
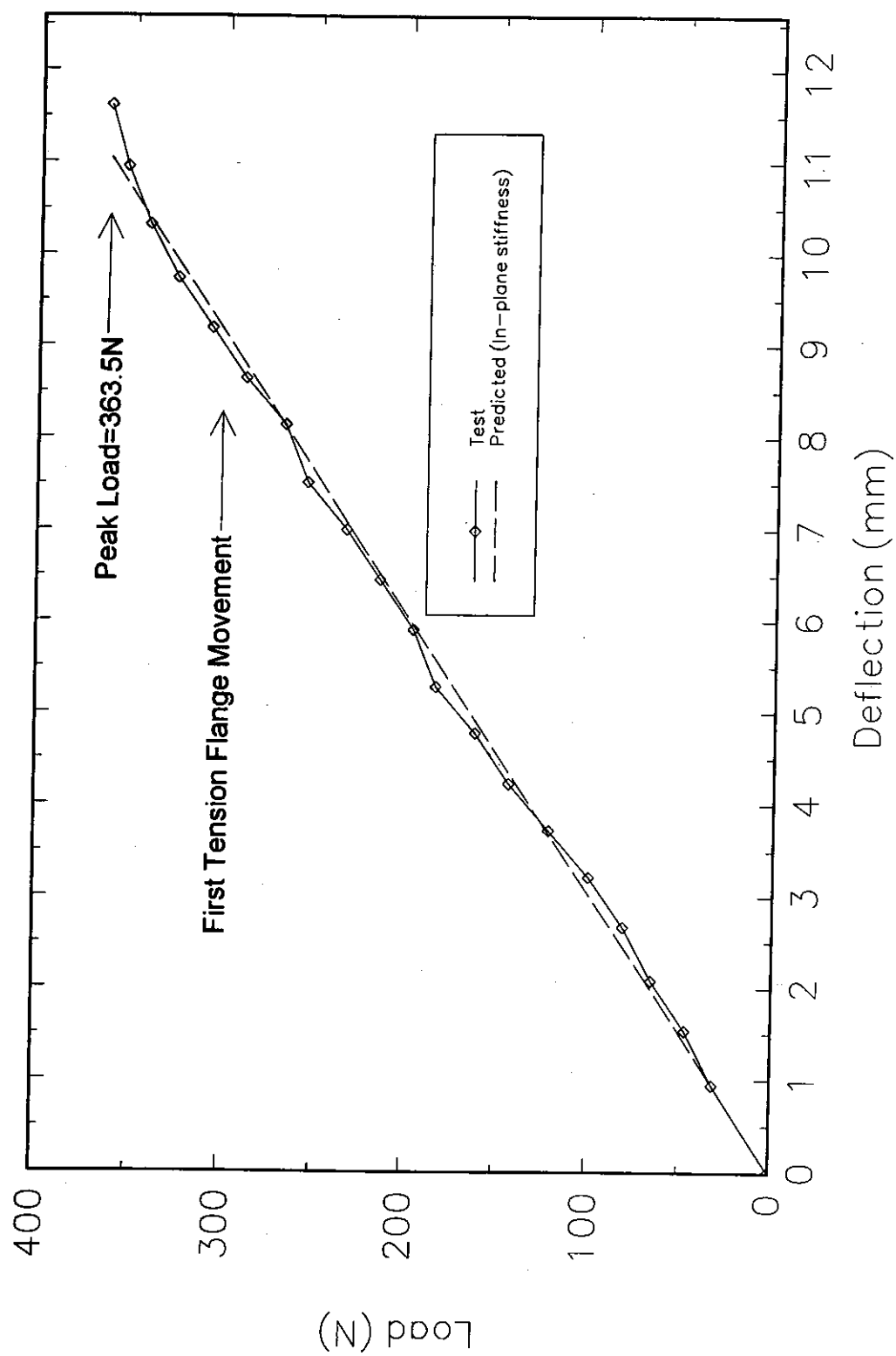
Figure 2.13
Load versus In-Plane Deflection
Model Beam B
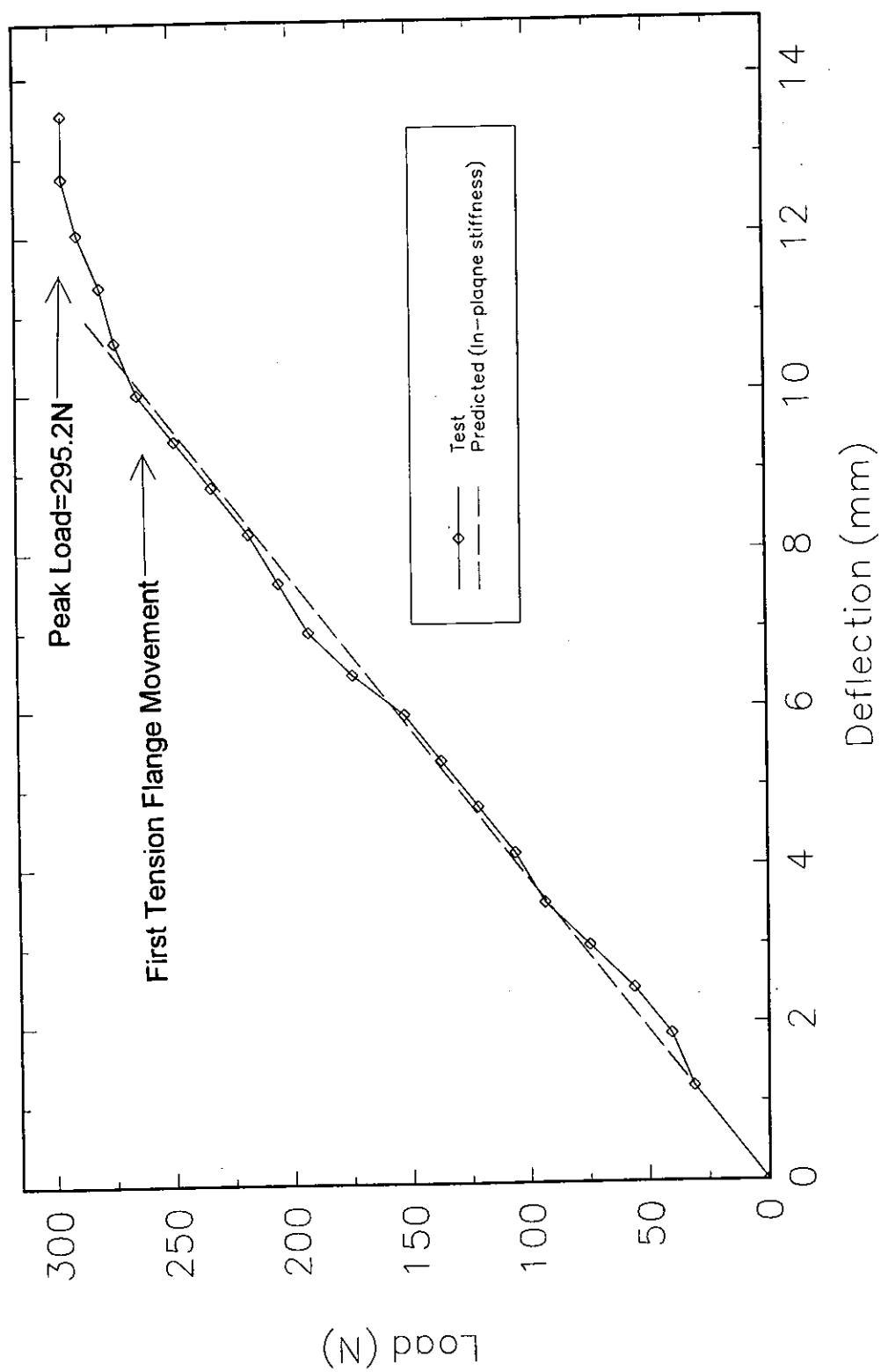
Figure 2.14
Load versus In-Plane Deflection
Model Beam C
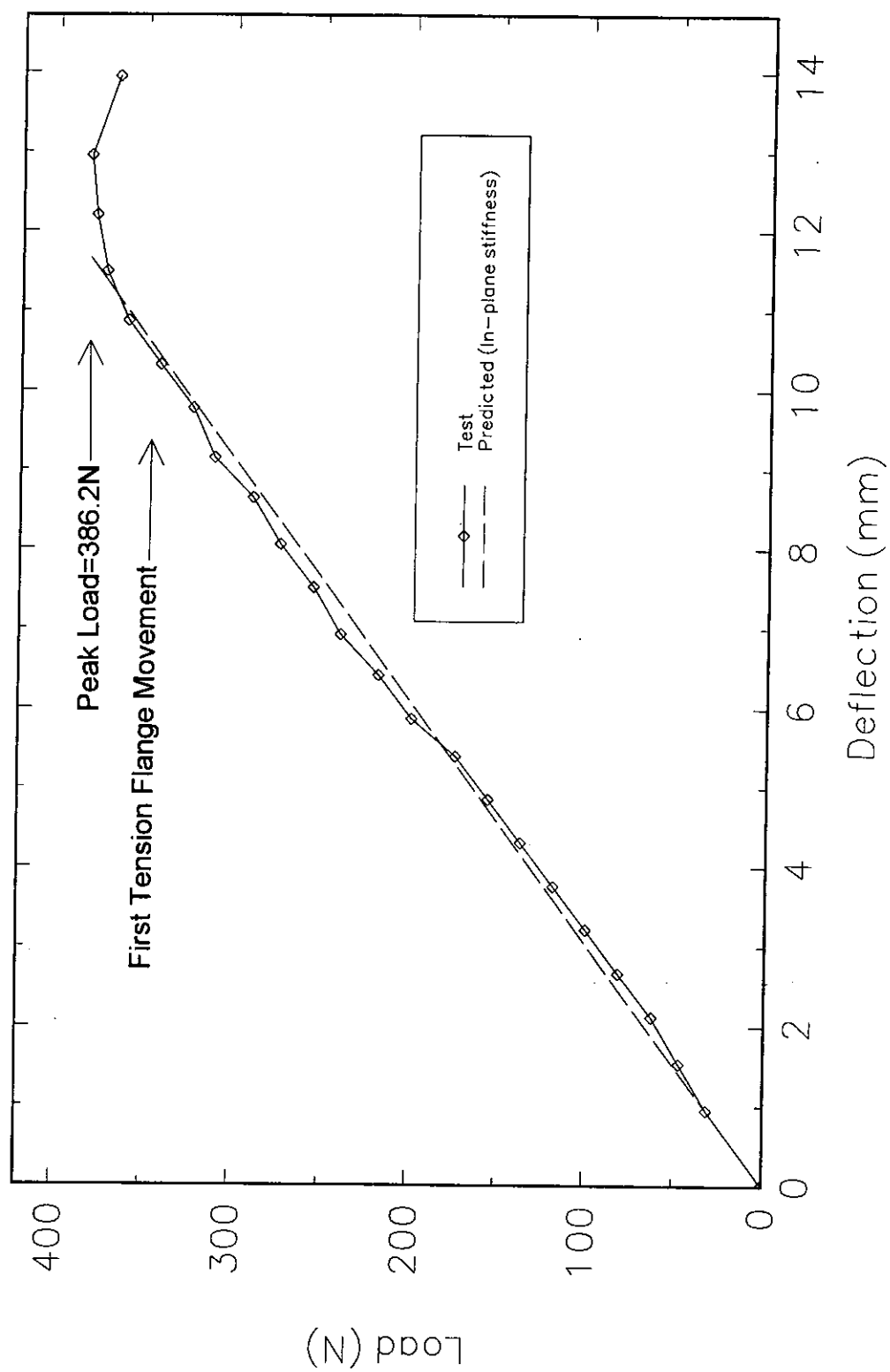
Figure 2.15
Load versus In-Plane Deflection
Model Beam D
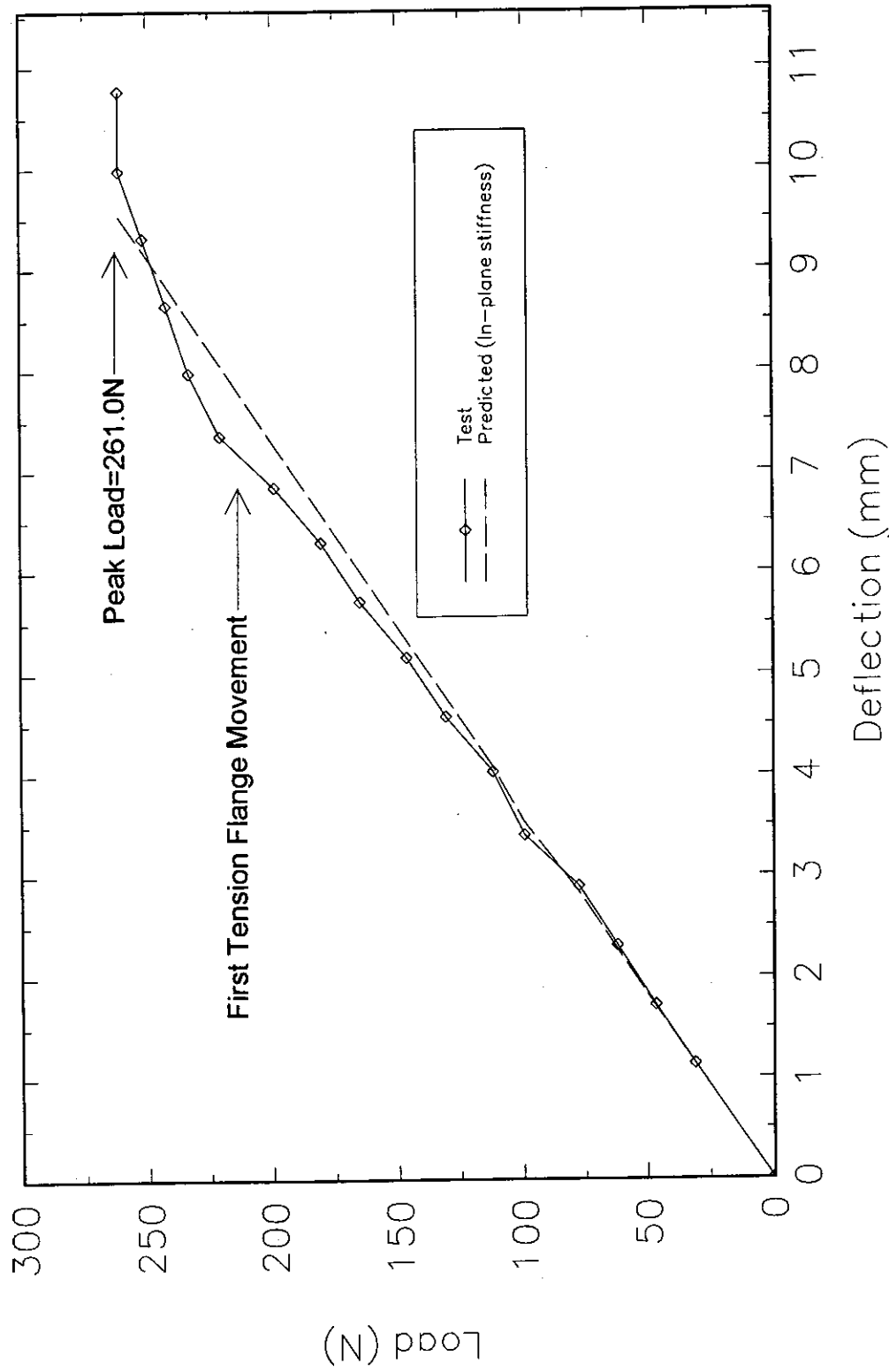
Figure 2.16
Load versus In-Plane Deflection
Model Beam E
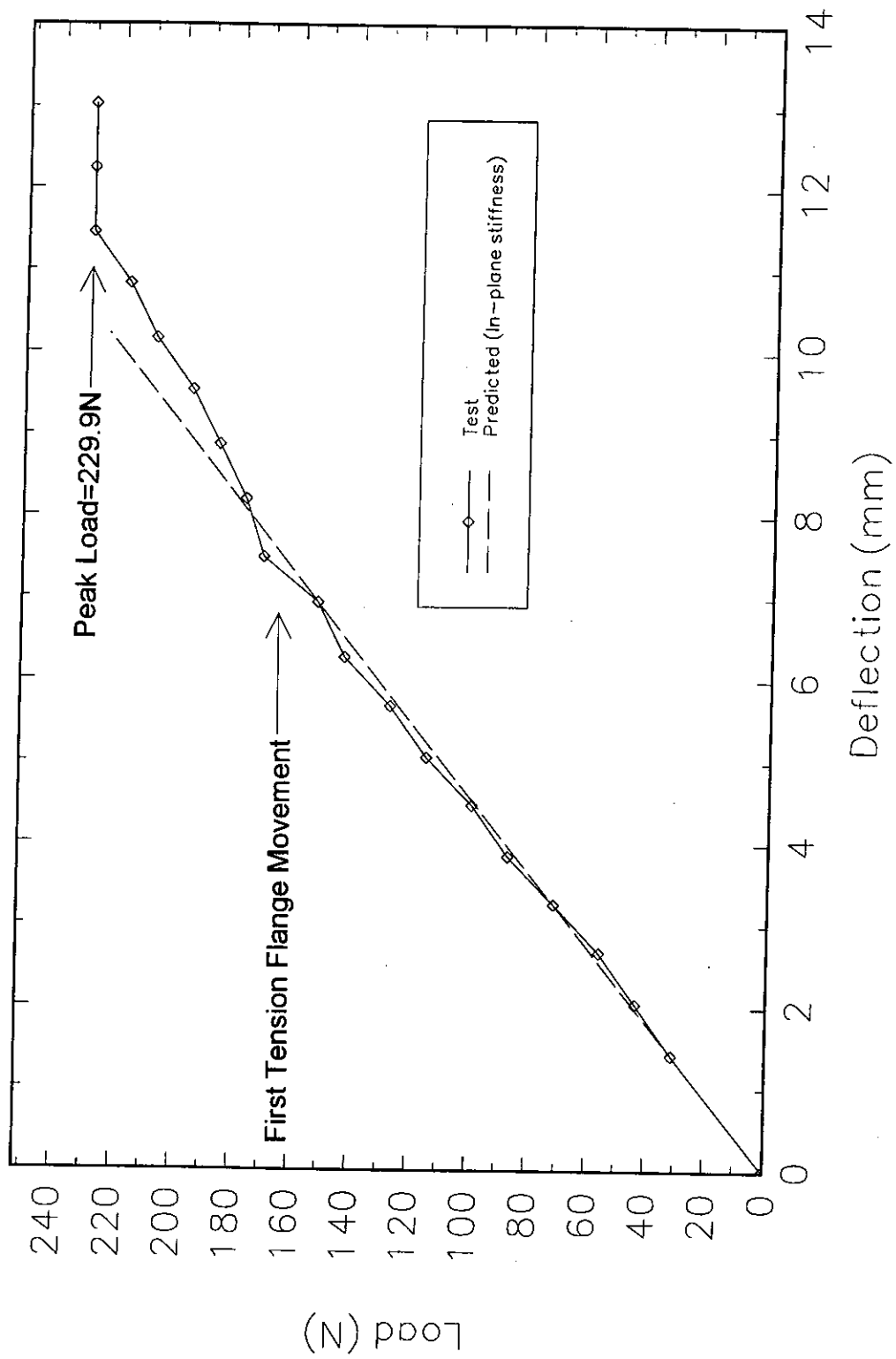
Deflection (mm)

Figure 2.17
Load versus In-Plane Deflection
Model Beam F

Peak Load=229.9N

First Tension Flange Movement

Test
Predicted (In-plane stiffness)

Load (N)
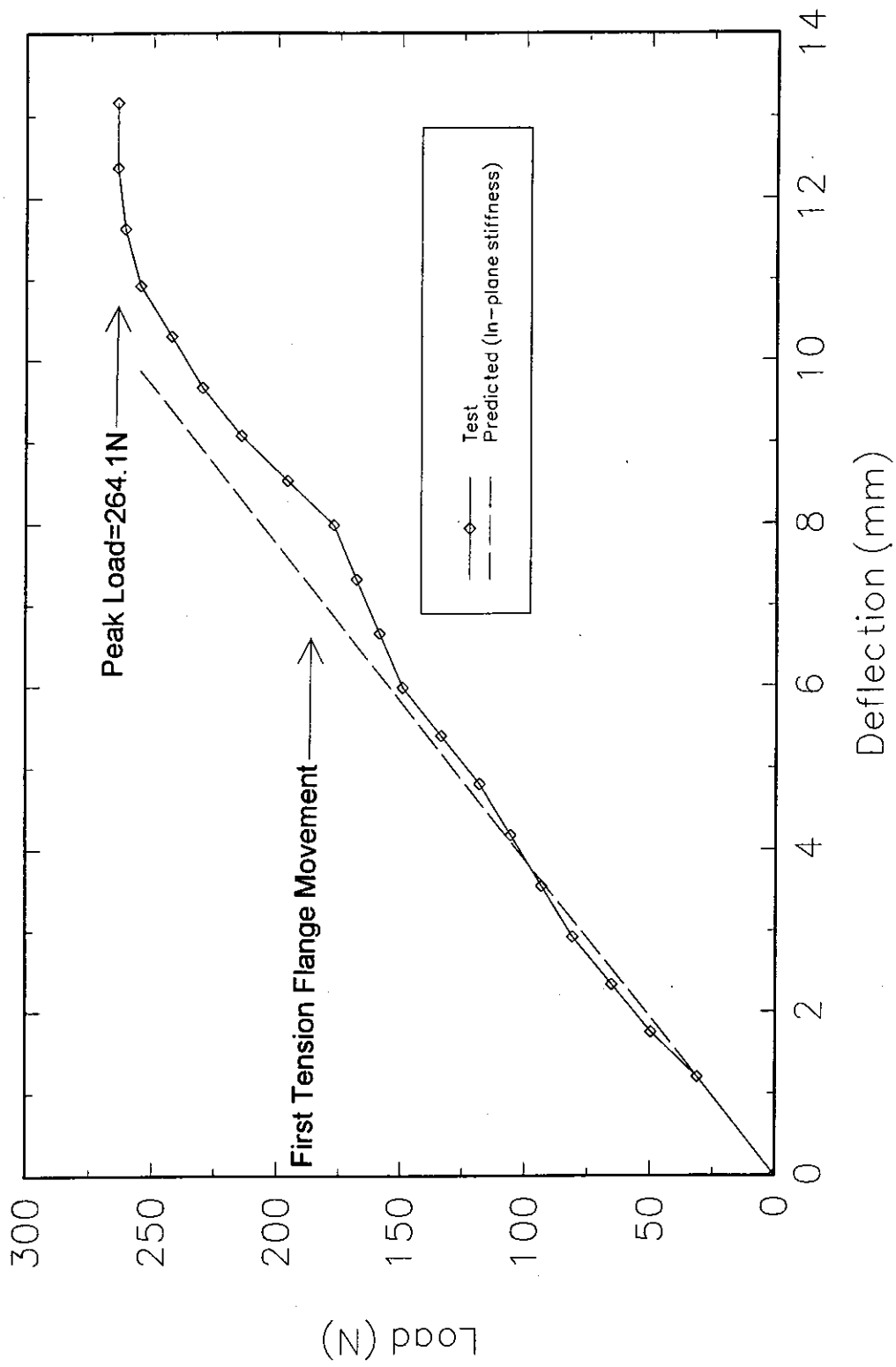
Figure 2.18
Load versus In-Plane Deflection
Model Beam G
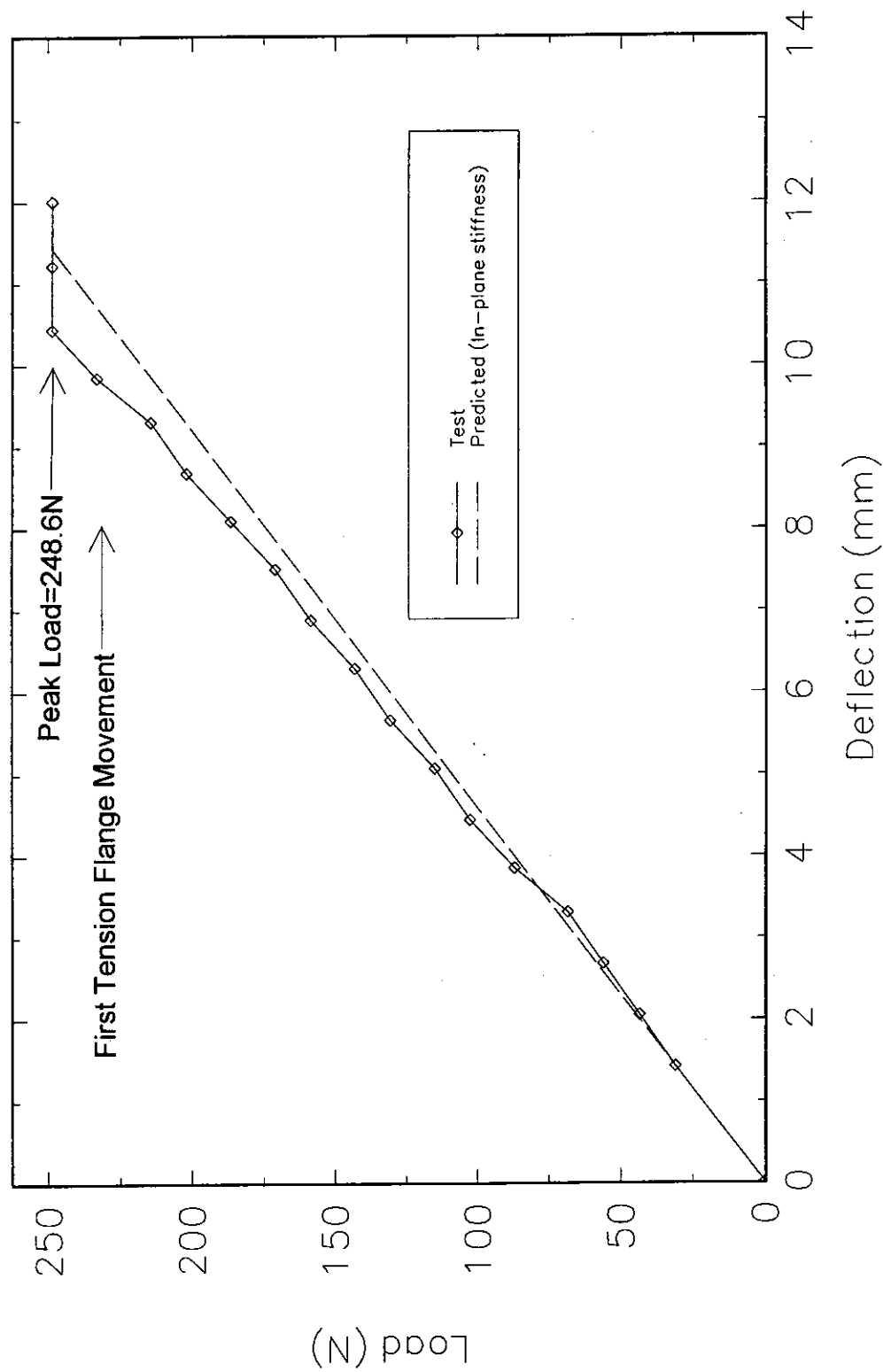
Figure 2.19
Load versus In-Plane Deflection
Model Beam H

Peak Load=233.0N →

First Tension Flange Movement →

Test
Predicted (in-plane stiffness)

Deflection (mm)

Load (N)
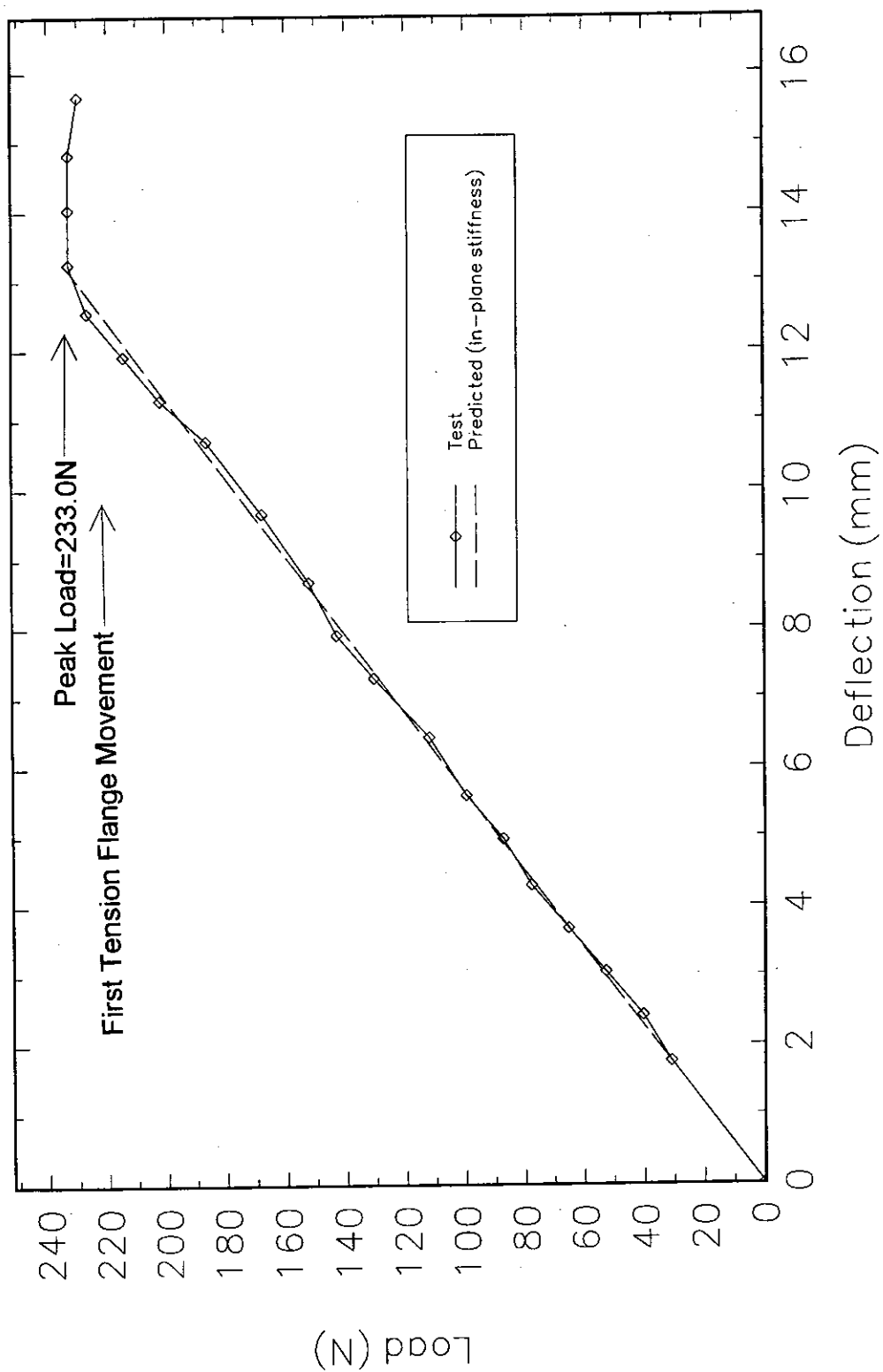
Figure 2.20
Load versus In-Plane Deflection
Model Beam I

3. PRELIMINARY ANALYSIS

Before embarking on a full scale test series, analysis of data collected from the model test series was done. This analysis was done to provide a better understanding of tension flange movement buckling behaviour, to add to the existing data set comprising University of Texas full scale and model tests and finite element analyses and to facilitate the formulation of a simple predictive model to aid in the selection of full scale test specimens. This was necessary because previously proposed models failed to provide reliable predictions of buckling loads. The use of those models in the selection of members susceptible to tension flange movement buckling had the potential to give inaccurate estimates of failure load and allow specimens to fail as a result of other failure modes.

3.1 Finite Element Model

Finite element modelling was performed using the BASP computer program, written by *Akay et al.* (1977) at the University of Texas. The program was selected since it was designed specifically for analysis of I-beams with load and restraint boundary conditions similar to those used in both the styrene model and full scale testing. The results obtained using BASP could be duplicated using almost any finite element program.

Finite element models provided guidance in the design of specimens, gave expectations of failure loads and buckled shapes and allowed comparison of test results to a consistent and reliable theoretical solution technique.

I-beams were modelled using 2-D plate elements to represent the web. Use of several elements through the depth of the web accurately models web distortion

and local buckling of the web. Flange elements are modelled using 1-D beam elements. These elements are assigned flexural stiffnesses about the vertical and horizontal plane, axial stiffness and torsional stiffness about their long axis. This allows accurate modelling of local flange buckling and torsional restraint provided to the web in cases of web buckling. A schematic of a typical beam model is shown in Figure 3.1

The output of a finite element analysis may include any or all of the following data, in graphical or numerical form:

·A map of node numbers, node positions, element numbers and element connectivity.

·Longitudinal stresses at each node along the top chord of the beam model.

·In-plane stresses at each node in the web.

·A normalized buckled shape (an eigenvector) of the beam composed of the out-of-plane deflections of each node.

·A buckling load (eigenvalue) which represents the magnitude of the bifurcation load of the system relative to the input loading. (In this case, input loads were unit loads, thus, the eigenvalue output was numerically equivalent to the buckling load.)

3.2   Analysis of Model Tests

Primary concern in the use of model tests is the validity of the similarity of model behaviour and the full scale structure. Geometric similarity was not an issue since modelling a structure type, namely a doubly symmetric simply supported I-beam, rather than a specific structure was the primary intent of the test program. Similarity of material stress strain relationships was of concern in this case but since both the finite element model and the *Yura* theory use linear elastic stress strain relationships as their foundations, the model tests were, therefore, limited to the linear elastic stress range. A material with a linear stress strain relationship was used for the model test specimens to ensure similarity of material behaviour. Observation of load versus measured in-plane deflection was compared to theoretical predictions to assess the accuracy of measured material properties and specimen geometry. All test specimens were tested entirely in the elastic range and exhibited in-plane stiffnesses as predicted by flexural theory (see Figures 2.10 through 2.20).

In all cases, specimens exhibited gradual development of out-of-plane deflections as the loading progressed. Development of these out-of-plane deflections were accompanied by reduction of the in-plane stiffness of the specimen. Buckling load was taken as the peak load reached during the test.

The magnitude of the failure loads measured in the parametric series are compared to predicted failure loads for the model beams in Table 3.1. The predicted failure loads are calculated using the sources noted in the table.

Qualitative observation of the buckled shapes of test specimens agreed well with the predicted shapes from the finite element models. In all cases, the bottom

flange deflected laterally and formed a smooth sweeping curve along the full length of the beam. The web distorted smoothly along the length of the beam except directly under the load. An area of the web directly below the load point, approximately one web depth wide, displayed significant out-of-plane deflection and developed a large bulge to about 0.5 web depths below the load point. This shape is shown schematically in Figure 3.2

3.3   Proposed Model

To aid in the selection of full scale test specimens, it was decided to formulate a predictive model based on the observations of the finite element model and model test results. This model was intended to draw on work not including the column analogy of the *Basler* and *Yura* theory, but to treat the web buckle as the primary source of the failure. Formulation of a web buckling interaction equation was considered the best method to address the presence of both vertical and horizontal stresses in the area of the web directly below the load point.

Generally, the buckles observed in the model tests and predicted by the finite element analyses all possessed similar dimensions and attributes. A large bulge below the load point extended symmetrically about the load axis to a width of approximately one web depth. Vertically, the web buckle was sharply curved and intersected the perpendicular bisector of the top flange at approximately one-half web depth (see Figure 3.2).

As shown in Figure 3.3, vertical stresses at the top of the web were assumed to be equal to vertical load divided by the product of web depth and thickness. The stresses were assumed to vary linearly from that magnitude at the

top of the web to zero at the bottom. Longitudinal web stresses were assumed to be equal to the web flexural stresses present at the cross section directly below the load. Shear stresses were assumed to play no part in the buckling.

Using observations of buckled shapes and assumptions regarding the magnitude of vertical and horizontal stresses in the web plate, an interaction equation was formulated as follows:

If the web vertical stress distribution is assumed uniform over the buckled web, vertical stresses are defined as:

$$[3.1] \ \sigma_v^T = \frac{P}{dt_w}$$

The horizontal stress distribution is assumed to be flexural, the left and right edge stresses will vary from zero at the web mid depth to the following at the top of the web:

$$[3.2] \ \sigma_h^T = \frac{Md}{2I_x}$$

where   M=moment at the load point,

I_x=strong axis moment of inertia of the beam.

The boundary conditions are assumed pinned on all sides to ensure a conservative estimate of buckling load. The critical buckling stresses for the assumed edge conditions and stress distributions are defined, by the Column Research Committee of Japan, Handbook of Structural Stability (1971), as:

$$[3.3]\ \sigma_{cr}=K\frac{\pi^2 E}{12(1-v^2)(c/t_w)^2}$$

Where, for vertical stresses, K=4.00, and for flexural stresses, K=23.9.

While the expression for critical vertical stress corresponds to a uniform stress through the depth of the web, the expression for estimated vertical stress corresponds to a triangular vertical stress distribution through the web depth. The Column Research Committee of Japan, Handbook of Structural Stability (1971) states that, for pin edged plates, critical uniform vertical stress equals 0.53 of the critical vertical stress for a triangular stress distribution. Doubling the critical vertical stress in the interaction equation, below, provides an estimate of the critical maximum vertical stress under triangular stress distribution consistent with the estimated vertical stress.

Formulating an interaction equation of the form:

$$[3.4]\ 1\geq(\frac{\sigma_v^T}{2\sigma_{cr_V}})^2+(\frac{\sigma_h^T}{\sigma_{cr_H}})^2$$

results in the following expression:

$$[3.5]\ 1\geq(\frac{P/dt_w}{2\sigma_{cr_V}})^2+(\frac{Md/2I_x}{\sigma_{cr_h}})^2$$

Since M is a function of P, the variable P is unique for a given beam geometry and loading and equal to the predicted buckling load of the system, P_{cr}.

The predictions of this interaction equation are compared to finite element solutions, AISC sidesway buckling predictions, University of Texas test results and the results of this parametric study in Chapter 6.

3.4 Discussion

The results of the model test program were interpreted as being significant in that they substantiated the following finite element and Yura theory predictions:

·Tension flange movement can result in abrupt reduction of the in-plane stiffness and strength of a point loaded I-beam.

·Tension flange movement is characterized by a large web bulge directly below the load point and tension flange sweep. This is a combination of local and overall instability.

·Load versus in-plane deflection curves generally display an initially linear response which becomes non-linear and forms a plateau (constant load with continuing in-plane deflection). This is consistent with buckling behaviour.

·Specimens showed no signs of residual deformations after testing. This indicates that specimens were elastic during testing.

·Instability may be caused by the destabilizing effects of vertical compression in the web coupled with the inability of the tension flange to restrain the lateral deflection of the web.

Table 3.1

Model Test Results

Beam	Test Peak (N)	F.E.M. (N)	*Yura (N)	Test/Pred. Ratios	
				F.E.M.	Yura
A	466.1	408.8	321.6	1.139	1.449
B	363.5	399.7	321.6	0.909	1.130
C	295.2	317.0	316.7	0.931	0.932
D	382.6	391.6	273.3	0.977	1.400
E	261.0	365.5	230.7	0.714	1.131
F	229.9	309.9	187.2	0.742	1.228
G	264.1	368.2	147.0	0.717	1.797
H	248.6	347.6	128.6	0.715	1.933
I	233.0	320.4	109.8	0.727	2.122
			Mean	0.841	1.458
			St. Dev.	0.154	0.408

Notes:

* The AISC LRFD simplification of the *Yura* theory was used for predicting failure loads.

Load point

Lateral Brace points = x

Real Structure

Load, P
dx=0
dz=0

dz=0

dz=0

y

x

Finite Element Structure

dy=0
dz=0

dy=0
dz=0

z

o = Node

− − − = 2-D Plate Element

⎯⎯ = 1-D Beam Element

d_i = Deflection in the i direction
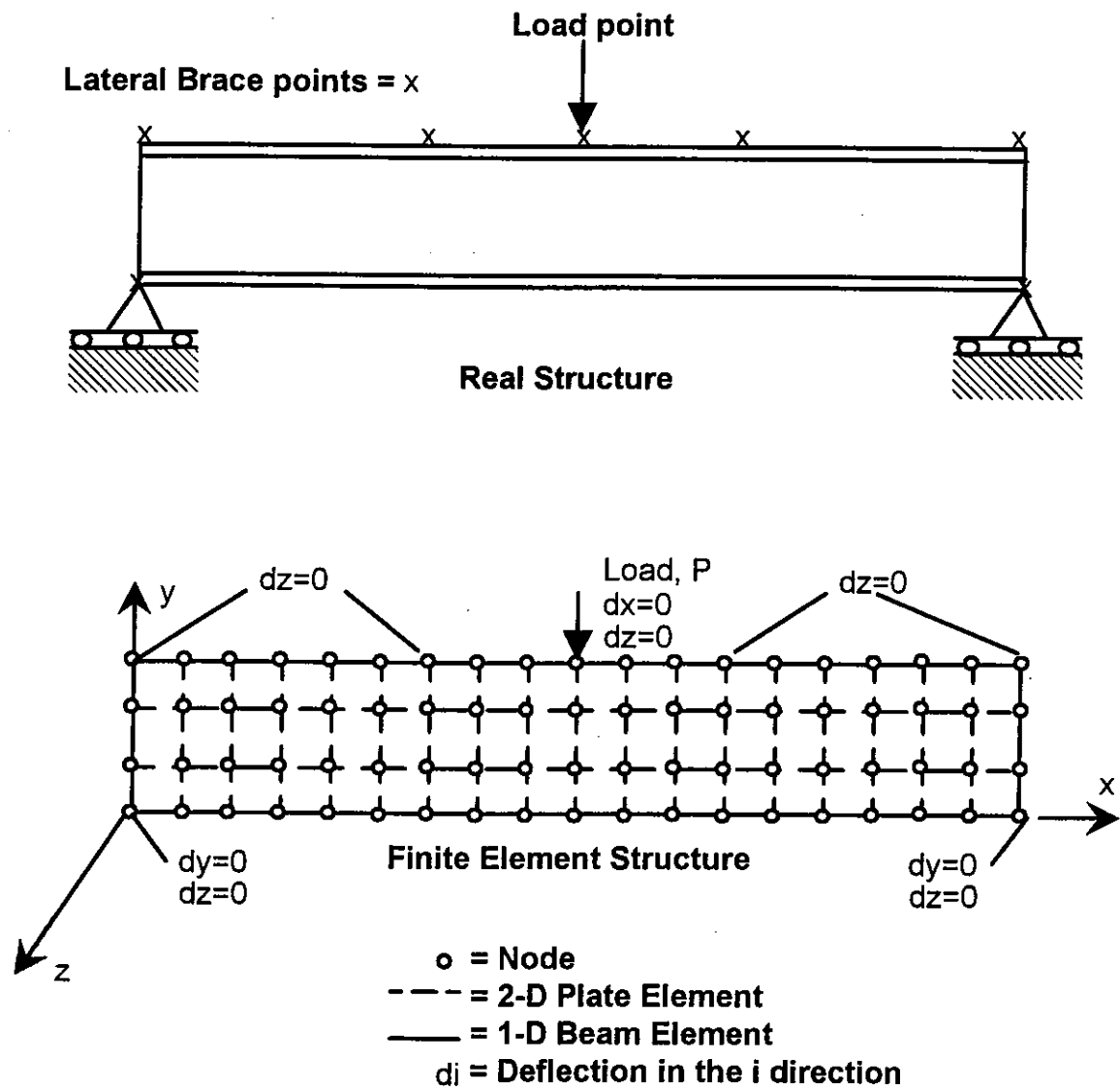
Figure 3.1
Typical Finite Element Model
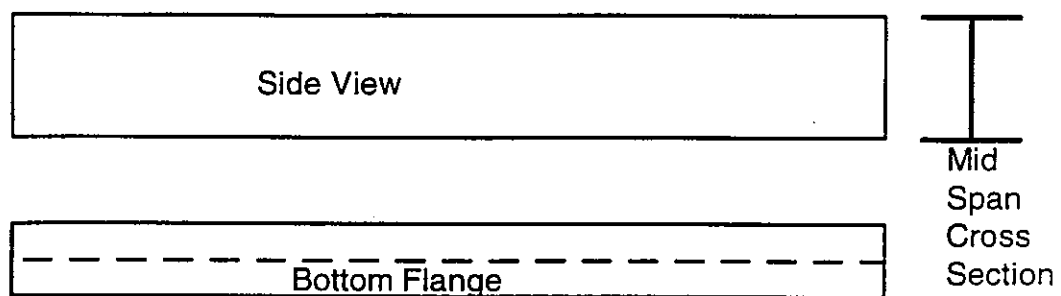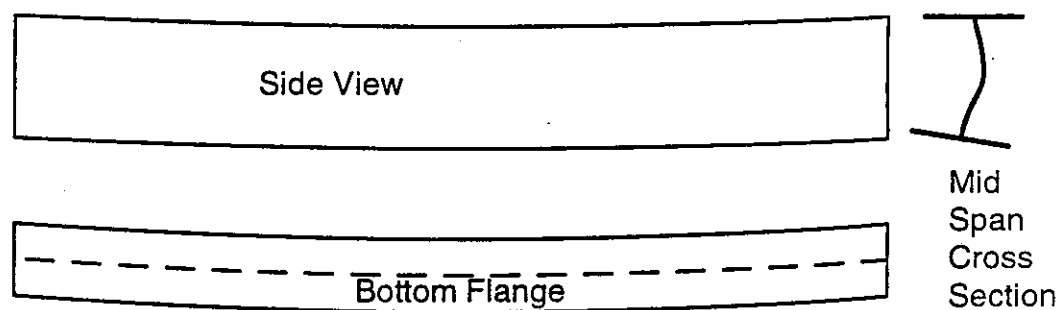
Figure 3.2
Typical Model Test Buckled Shape
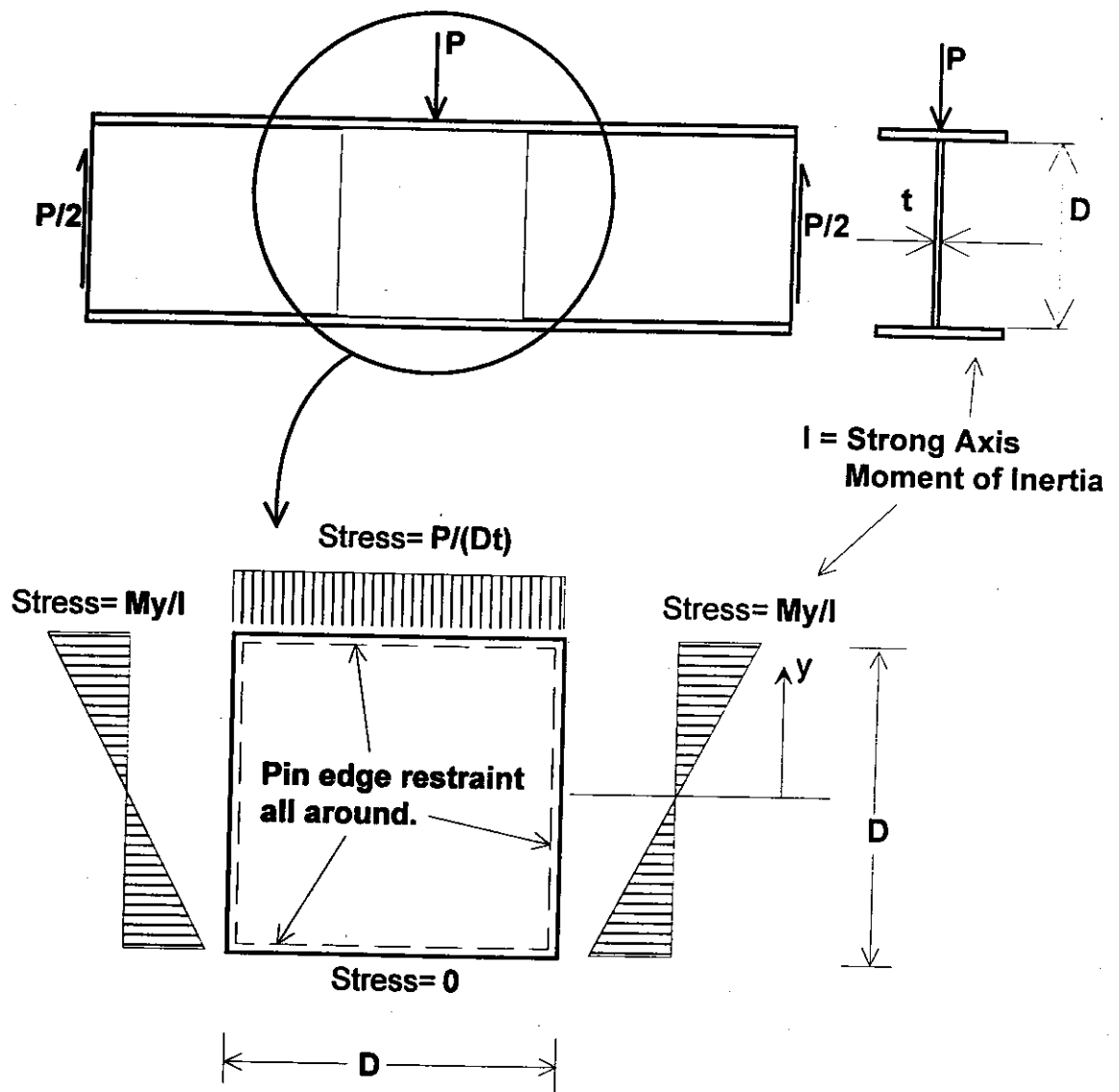
Figure 3.3
Proposed Interaction Equation Assumptions

4   FULL SCALE TESTS

4.1   Specimens

4.1.1   General

The full scale test program was designed to study the lateral tension flange movement behaviour of rolled steel I-beams. Variables studied included beam length, presence of restraining end moments and cross section properties. A total of five full scale tests were conducted in this series.

4.1.2   Dimensions

The five full scale tests were conducted on two different cross sections. The first two tests were on a W360x33 while the last three tests were on a W360x39. The W360x33 specimens were cut from the same rolled beam. The first test specimen (Test 1) was 6261 m long and after the first test, the specimen was cut to 5039 m long for Test 2. The first W360x39 specimen, Test 3, was 7482 m long and after the test was cut to 6261 m long for Test 4. The last W360x39 specimen was 5039 m long and was tested only once (Test 5). The measured dimensions of each specimen are recorded in Table 4.1.

4.1.3   Material Properties

Six coupons were cut from each of the three source members. The six coupons comprise two longitudinal flange coupons, two vertical and two horizontal web coupons. The results of the coupon tests are shown in Table 4.2. The coupon dimensions shown in Table 4.2 are averages of three

measurements taken within the gauge length of each coupon. Nominal coupon dimensions are presented in Figure 4.1. Measured coupon dimensions, shown in Table 4.2, were used for the calculation of yield stress, ultimate stress and modulus of elasticity.

4.2   Apparatus

4.2.1   General

Since the tension flange movement buckling load of a beam is related to the stress state in the web below the loading point and the lateral stiffness of the tension flange, any variation of these two factors will affect a resulting change in the buckling load. For the full scale tests, it was decided to include restraining end moments in the plane of the beam to reduce the buckling load of the system and assure elastic behaviour. By applying negative end moments to the beam, compressive stresses are added to bottom flange of the beam, resulting in a decreased lateral flange stiffness. The presence of these compressive stresses also increases the first yield load of the system and allows greater vertical stresses in the web in the elastic range. Since the Yura theory includes lateral flange stiffness as a variable in buckling load, it was decided to further reduce the lateral flange stiffness in an attempt to reduce failure loads of the beams and assure elastic buckling. Warping restraint at each end of the tension flange was reduced by the use of specially designed end conditions. By reducing the amount of tension flange warping restraint, a reduction in the lateral tension flange stiffness and Yura theory buckling load of the system can be achieved.

4.2.2 End Restraints

To create a structural system particularly susceptible to tension flange movement buckling, an end condition which provided some negative moment in the plane of the beam while not permitting the development of warping stresses in the ends of the bottom flange was constructed. The connection, shown in cross-section in Figure 4.2, was designed to resist the full plastic moment of the strongest section tested, a W360x39. The top flange plate was designed to resist only flexural forces along the top flange and resisted no vertical load. The bottom flange plate resisted both the flexural and vertical reactions.

The bottom plate and bearing assembly allowed rotation about the connection axis (see Figure 4.2) and thereby eliminated warping stresses in the bottom flange. Vertical load reaction was carried through the ball thrust bearings to the bearing housing and finally to the columns. Horizontal forces, previously referred to as flexural forces, were transmitted to the columns through tapered roller bearings, shown in Figure 4.2. To prevent web buckling at the supports, web stiffener plates were placed against both sides of the web, and were bolted to the upper plate and the bearing housing. Knife edge contacts were placed at the interface of web and stiffener to minimize torsion restraint at the connection axis. Stiffener plates can be seen in Figure 4.2 and 4.4.

4.2.3 Load and Brace Frames

The full scale test setup, shown schematically in Figure 4.5, comprised two brace frames and one load frame. The load and brace frames provided appropriate bracing to the top flanges of the specimens and a load path for loading the specimens. Each frame consisted of a moving inner frame and a fixed outer frame. The outer frame bolted to the strong floor and provided two parallel vertical rails for the bearings of the inner frame to travel on. The rectangular inner frame travelled vertically on four roller bearings at each corner of the frame, which bore on the vertical rails of the outer frame. This assembly allowed only vertical translation of the inner frame relative to the strong floor. A schematic of the load frame is shown in Figure 4.6. The same arrangement was used for the two brace frames except no loading assembly or hydraulic jacks were connected. By attaching appropriate boundary conditions to the inner frames, the necessary top flange restraints were established. Boundary conditions are described in detail in Section 4.2.3.

While fulfilling all of the conditions of a brace frame, the load frame included special features to enable load transfer from the actuating jacks to the specimen, as shown in Figure 4.6. The frame members are web stiffened at the specimen load point, on the top horizontal member, and at the two jack attachment points on the bottom horizontal member. The inner load frame was actuated by two jacks beneath the strong floor, attached by two threaded steel rods to the bottom member of the inner load frame.

4.2.4 Boundary Conditions

Each brace point was required to suppress displacements of the top flange perpendicular to the plane of the undeformed web and rotations about the vertical axis. The assembly shown in Figure 4.7 was used to suppress those degrees of freedom. Displacements in the long direction of the test specimens were suppressed at the mid-span of the beam since, by symmetry, the longitudinal deflection of that point would be very small. Top flange boundary conditions were designed to provide a rotational degree of freedom such that the axis of rotation parallel to the beam axis was at the center of the upper surface of the top flange. The combination of two rockers, each rotating about perpendicular axes, and three sets of mutually orthogonal roller bearings permitted displacement or rotation in five of six degrees of freedom. The bearings and rollers, by themselves, suppressed only rotation of the brace point about the vertical axis. The addition of the lateral bracing between the brace point and inner frame suppressed deflection of the brace point perpendicular to the plane of the web. Some compromise was made to ensure constructability of the assembly. The use of tension rods or struts, as shown in Figure 4.8, provides the required restraint for small rotations, but imposes small lateral deflections of the top flange at large flange rotations. Since tests were limited to small top flange rotations (< 20°), the arrangement was considered acceptable. Photographs of the restraint and load frame boundary conditions are shown in Figures 4.8 and 4.9, respectively.

4.3   Instrumentation

4.3.1   Strain Gauges

Strain gauges fulfilled two roles in this test series. They were used to monitor the local stress state in the web, directly below the load point, and they were used to monitor the flexural strains along the length of the beam for the checking of static equilibrium.

Two types of gauges were used in the area of the loading. The layout of the local strain gauges is presented in Figure 4.10. Longitudinal gauges were applied to the top and bottom flange, 12.5 m from the flange tips, at the beam mid-span. Data from these gauges allow calculation of the in-plane beam moment as well as the warping stresses developed by the out-of-plane deflection of the bottom flange. Three rosette gauges were places on each side of the web in a vertical line below the load point. Data from these gauges reflects the stress state in the web as a result of flexural, shear and vertical stresses. By comparing rosettes from opposing sides of the web, strain gradients can be detected in the case of web distortion or buckling. Vertical strains below the load point are of particular importance for validation of stress distribution assumptions made in the previous University of Texas analytical studies.

Twelve strain gauges were placed at four vertical cross sections along the length of the beam, as shown in Figure 4.11. The gauges were oriented parallel to the beams long axis and were placed on the top flange centerline, the mid depth of the web and the top surface of the bottom flange. Gauges

were placed on the top surfaces of the flanges since, to aid alignment of the load axis and the rosette gauges, the specimen was clamped in the load frame prior to application of the gauges. It would difficult to apply the liquid strain gauge adhesive to a downward facing surface. The flexural strain gauges were used to determine in-plane bending moment at the gauge locations, allowing calculation of restraining moments at end conditions and static equilibrium checks during testing.

4.3.2   Displacement Measurement

Vertical deflection of the mid-span of the test beam was monitored by a single cable transducer, attached to the bottom horizontal member of the moving inner load frame as shown in Figure 4.12. Deflections of the inner load frame were accounted for by a process similar to that described in Section 2.6, Model Test Results. Determination of the inner frame stiffness was done using the apparatus shown in Figure 4.13 and schematically in Figure 4.14. A photograph of the deflection measurement at the inner load frame is shown in Figure 4.15. The final overall beam deflection was the deflection measured by the cable transducer minus the deflection of the inner load frame (load divided by inner frame stiffness).

Lateral deflection, vertical deflection and twist of the bottom flange at beam mid-span were measured by two cable transducers attached to each flange tip as shown in Figure 4.12. By knowing the distance between the cable transducer boxes and the flange tips, the position of the flange tips can be determined geometrically. Using the position of the two flange tips, flange lateral and vertical deflections and twist can be determined (relative to the inner frame).

Out-of-plane web deformations were measured at selected load levels using a bank of four linear variable displacement transducers (L.V.D.T.'s) placed in a mounting bracket as shown in Figure 4.16. The bracket contact points were placed against the web at five locations giving a total of twenty web deflection readings. The location of the contact points and the deflection measurement locations, points A1 through D5, are shown in Figure 4.17.

At four or five locations, depending on the length of the specimen, between the load point and the bean support, the lateral deflection of the bottom flange was measured using cable transducers. The position and orientation of these transducers is shown in Figure 4.18. Data from the lateral deflection transducers provides information relating to the buckled shape of the beam and, by estimating the curvature at the end of the bottom flange, the magnitude of the warping stresses at the end of the bottom flange.

4.3.3 Load Measurement

Load measurement was accomplished by positioning a load cell as shown in Figures 4.7 and 4.9. Because of the complexity of the end conditions, it was considered too difficult to include a load measurement device in the end assemblies. The exclusion of redundancy in the load measurement at the ends of the beams required static equilibrium checks to be done indirectly using strain gauges and flexural theory as described in "Section 4.3.1 Strain Gauges".

4.4 Test Procedure

Specimens were fabricated outside of the test frame and then inserted into the frame using an overhead crane. Once positioned, the specimens were

bolted to the end conditions and the bolts were tightened to provide a friction connection. The web stiffener plates were installed and tightened and the support columns were shimmed, if necessary, to prevent any rotation or deflection upon tightening of the floor bolts. Floor bolts were inserted and tightened. This procedure was followed to minimize the erection stresses in the specimen. Once primary assembly was complete, strain gauges were applied (if required) and reconnected to the data acquisition system and the boundary conditions were assembled on top of the beam. Finally, the brace and load frames lowered into place and the hydraulic jacks were positioned below the floor and connected to the load frame.

Testing was begun by taking a full set of twenty web deflection measurements with the LVDT bank. Loading was then commenced in increments of 5 kN until lateral bottom flange deflections exceeded 1 m. Loading then continued under stroke control in vertical deflection increments of 1 m. A one minute wait and stable load readings were required after each load or stroke increment before readings were taken to ensure static loading. Loading of the specimen was halted when a peak load was passed or excessive lateral deflections of the tension flange were observed. The excessive deflection stop criterium was introduced to the test program because of instability of the restraint frame boundary conditions at bottom flange material deflections greater than approximately 15 m. During a preliminary test of the apparatus, one of the assemblies (Figure 4.8) fell from the beam top flange and damaged equipment. To ensure safety and avoid damage in subsequent tests, deflections were limited. Specimens were unloaded in increments of 5 kN to 40 kN, depending on the specimen, load level and behaviour observed.

Table 4.1

Full Scale Test Specimen Dimensions

Test	Beam Length (m)	Web Thickness (m)	Beam Depth (m)	Flange Width (m)	Flange Thickness (m)
1	6261	5.76	349	127	8.18
2	5039	5.76	349	127	8.18
3	7482	6.44	353	127	10.57
4	6261	6.44	353	128	10.57
5	5039	6.57	353	128	10.30

Table 4.2

Full Scale Coupon Test Results

| Designation	Coupon Width	Coupon Thickness	Yield Stress (MPa)	Ultimate Stress (MPa)	E (MPa)
A1F	11.65	8.17	356	526	203 000
B1F	11.60	8.20	356	528	217 000
A1V	11.56	5.80	391	545	212 000
B1V	11.56	5.75	396	544	214 000
A1H	11.57	5.75	376	538	245 000
B1H	11.60	5.75	376	544	214 000
A2F	11.55	10.75	322	552	207 000
B2F	11.58	10.38	325	544	227 000
A2V	11.70	6.40	369	564	227 000
B2V	11.63	6.40	373	565	224 000
A2H	11.58	6.48	371	559	204 000
B2H	11.63	6.50	367	557	205 000
A3F	11.42	10.80	327	547	195 000
B3F	11.50	9.80	323	547	196 000
A3V	11.54	6.65	372	558	207 000
B3V	11.58	6.52	375	561	203 000
A3H	11.54	6.55	374	558	206 000
B3H	11.55	6.55	369	557	202 000

Definition of coupon designations:

A,B - Identifies coupons from the same source member and location

1,2,3 - Identifies the source member (1=Tests 1 & 2, 2=Tests 3 & 4, 3=Test 5)

H,V,F - Identifies the location of the coupon on the source member :

F = Flange, V = Web (Vertical Orientation), H=Web (Horizontal Orientation)
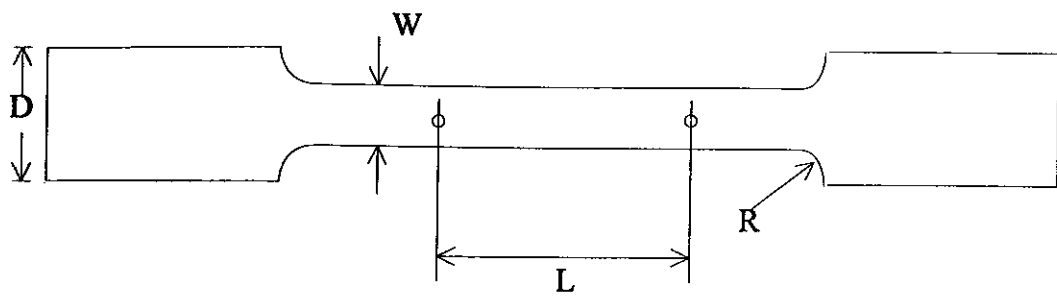
t = Thickness
D = 24.5 mm
W = 11.5 mm
L = 50.0 mm
R = 10 mm

Figure 4.1
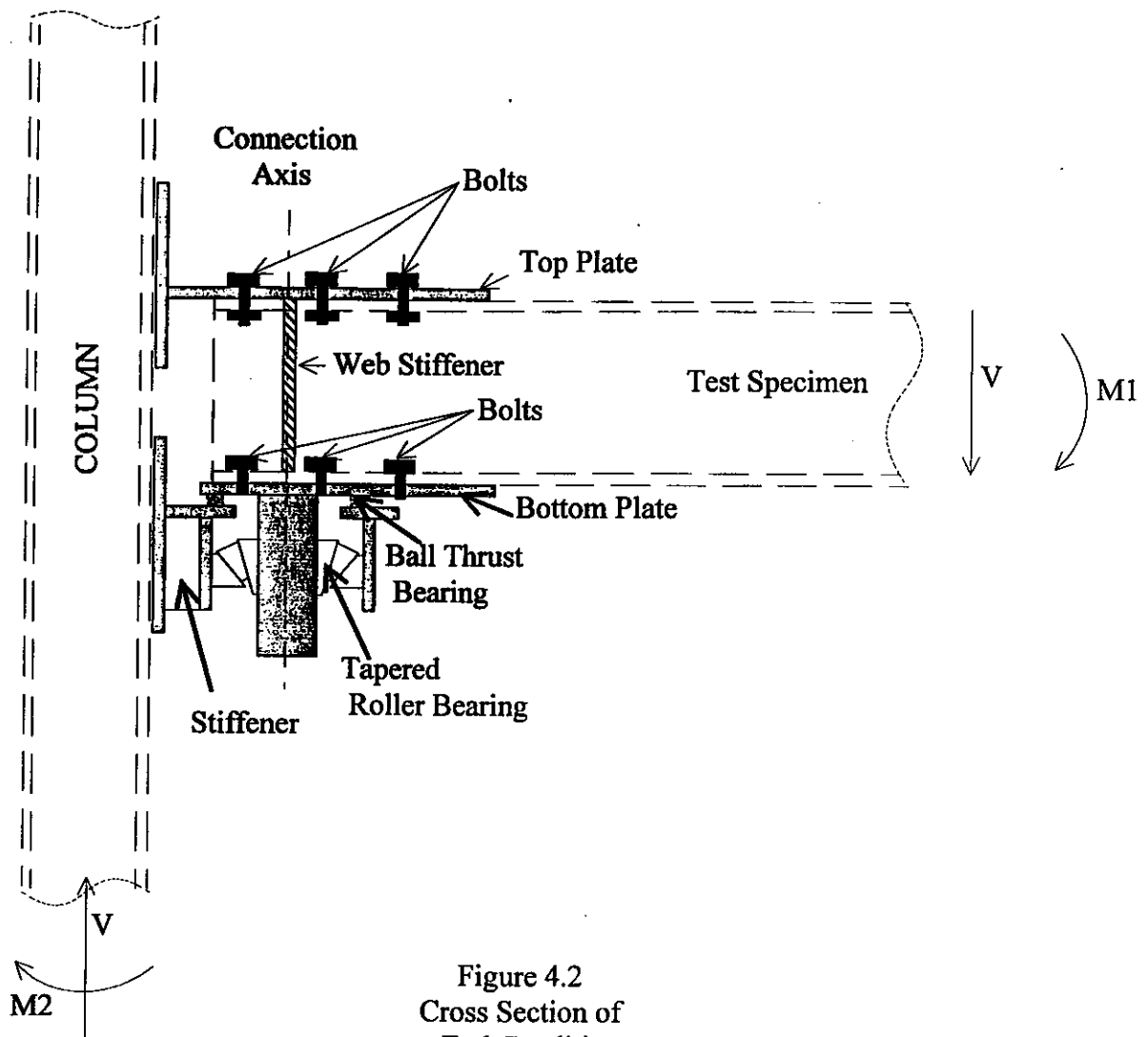Nominal Coupon Dimensions

Figure 4.2
Cross Section of
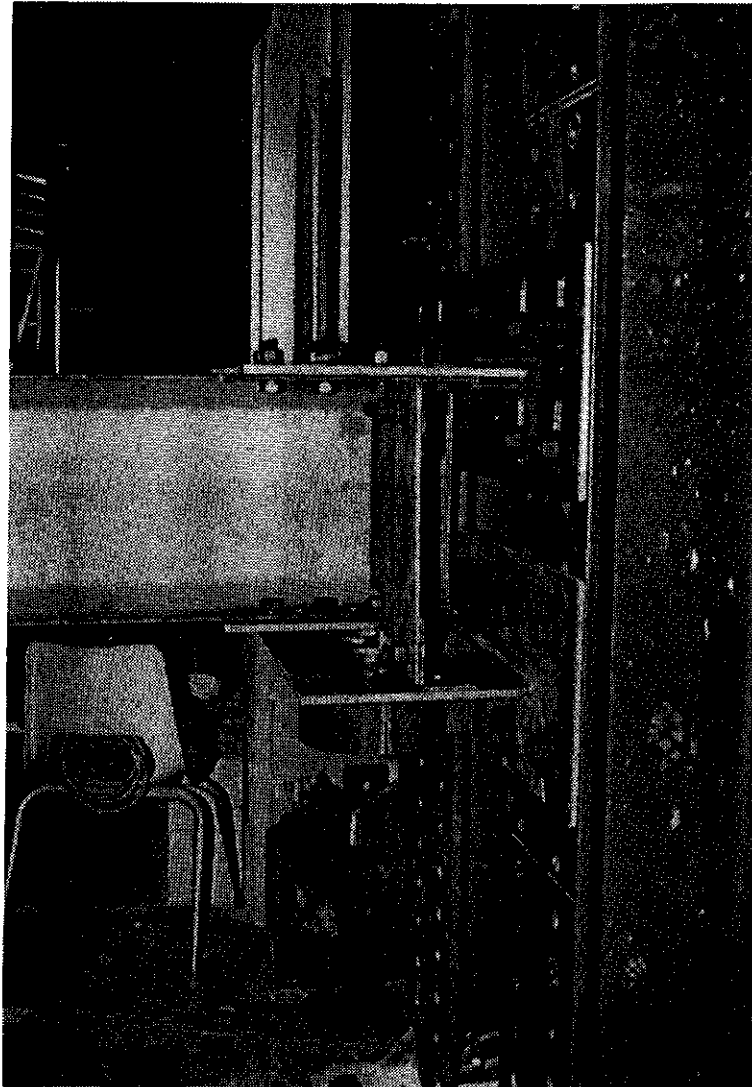End Condition

Figure 4.3
End Condition (Without Web Stiffener)

Figure 4.4
End Condition (With End Stiffener)
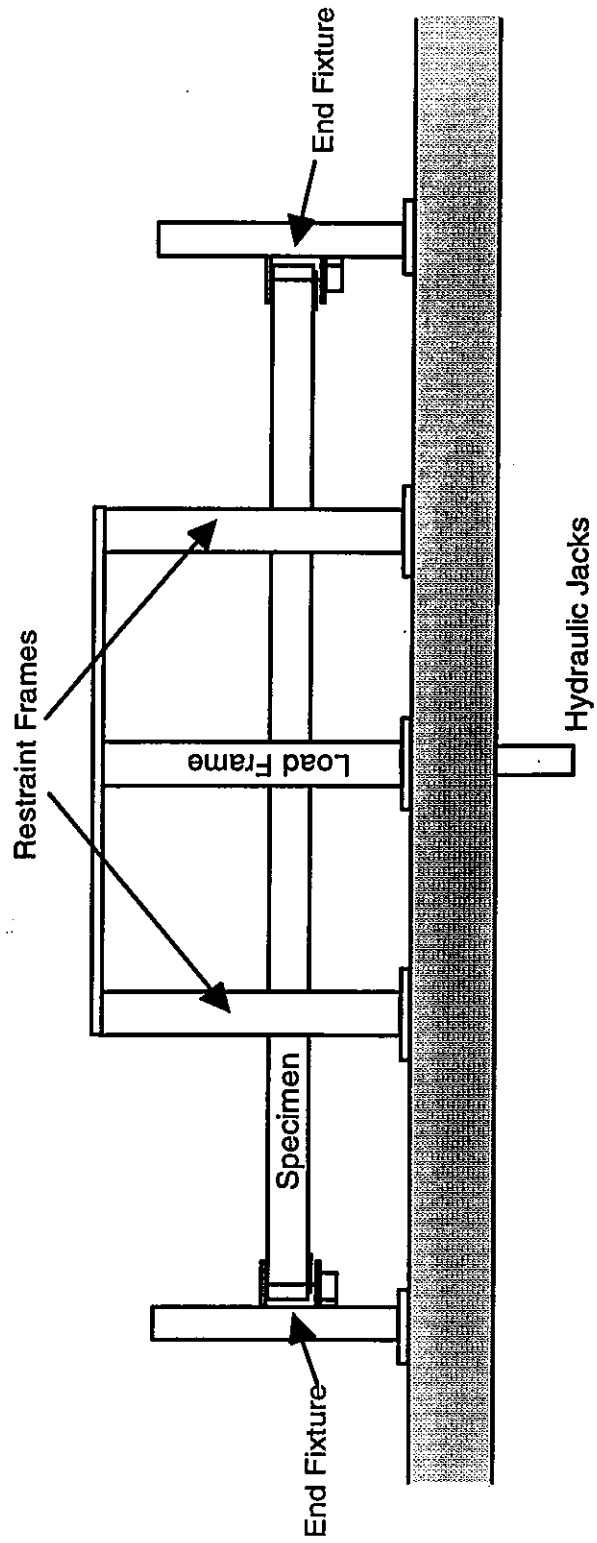
Figure 4.5
Schematic of Full Scale Test Apparatus

75
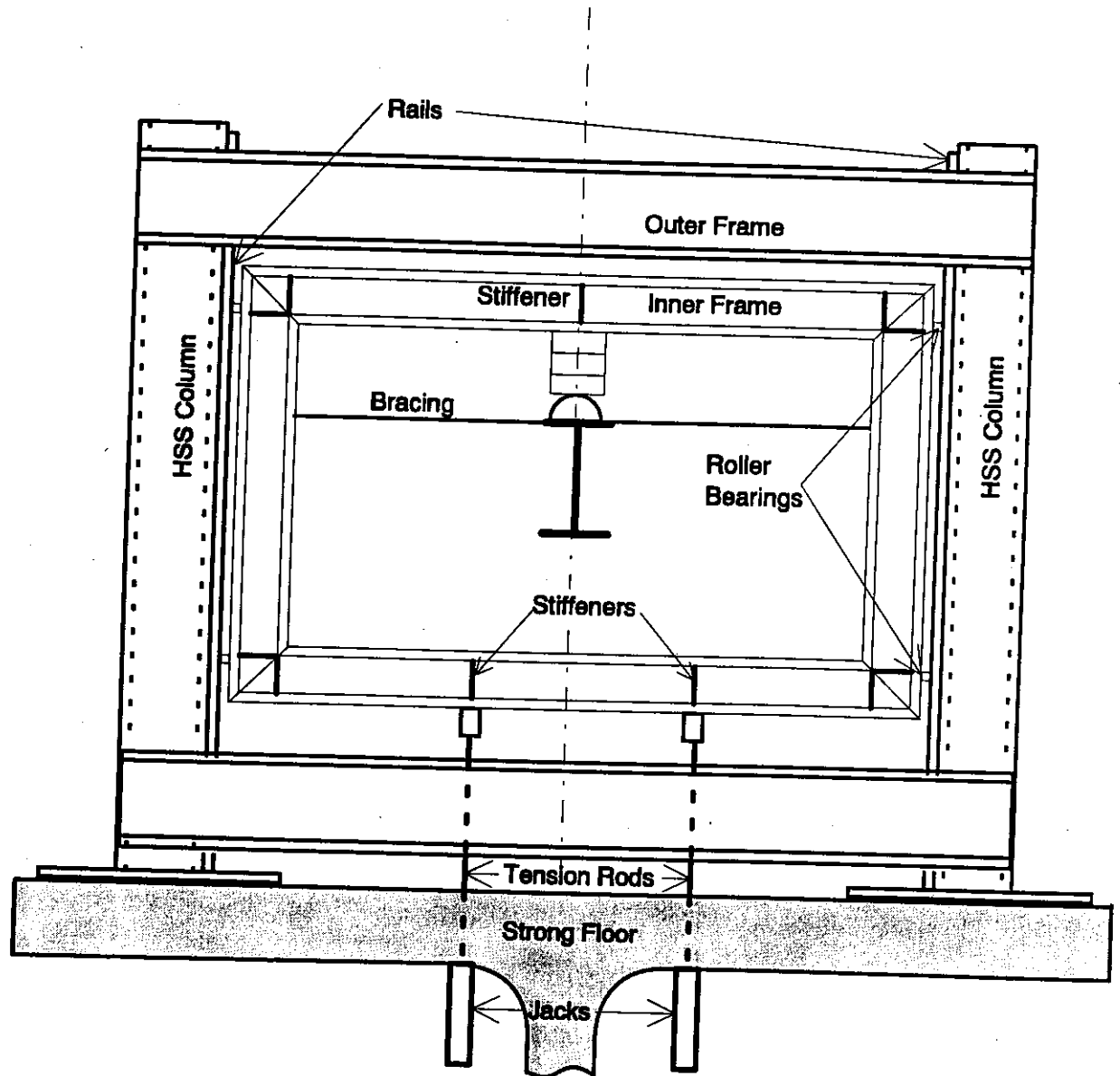
Figure 4.6
Loading Frame Schematic

Brace Frame Top Horizontal

Roller Bearing

Hemi-cylindrical Rocker

Bracing

Specimen

Restraint Frame

Stiffeners

Load Cell

Bracing
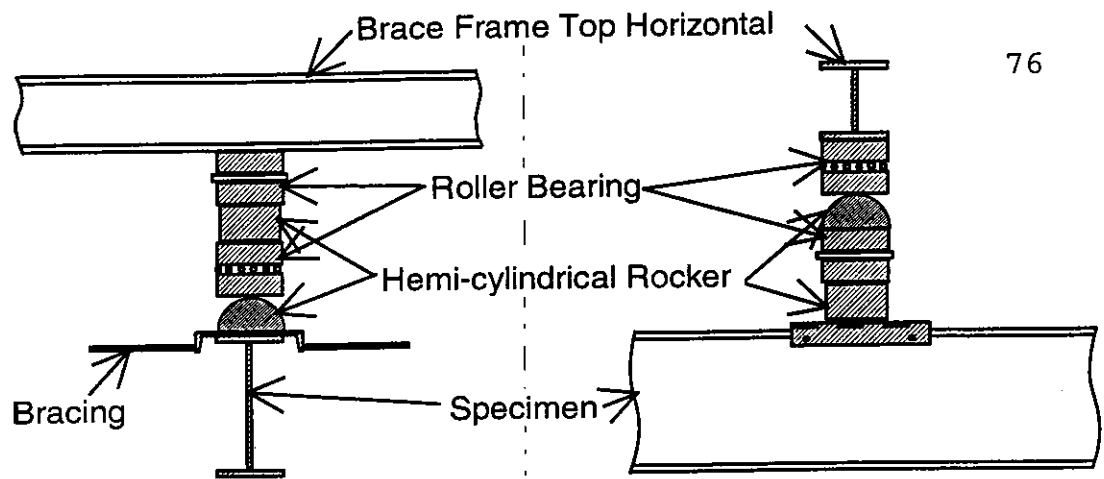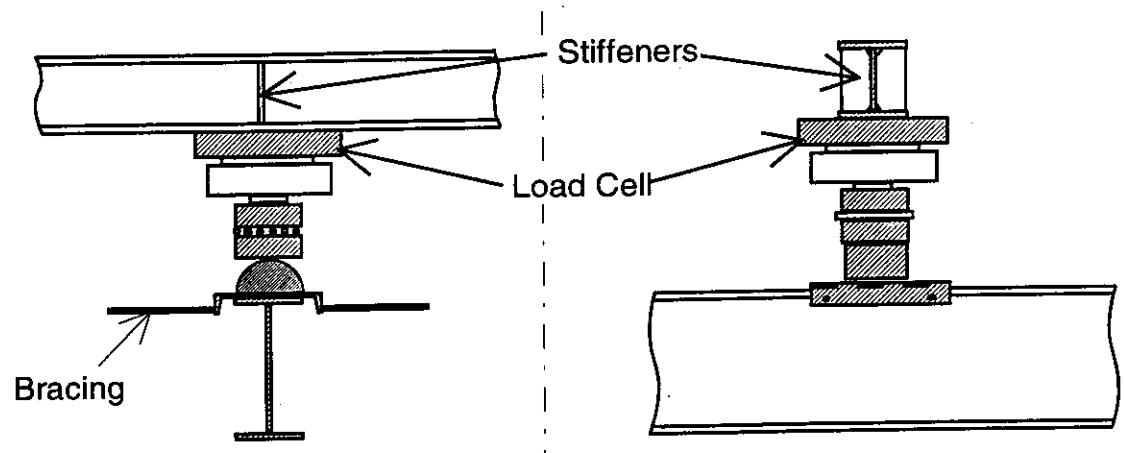
Load Frame

View Looking South

View Looking East

Figure 4.7
Boundary Conditions
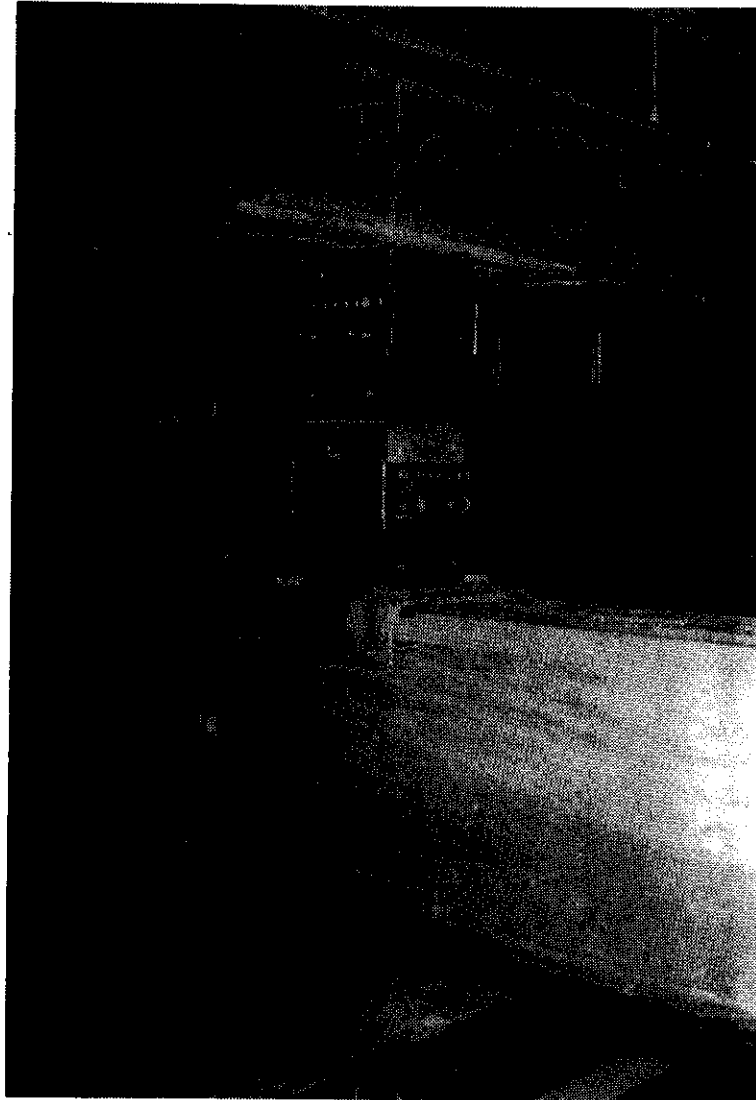
Figure 4.8
Test Apparatus
Restraint Frame Boundary Condition
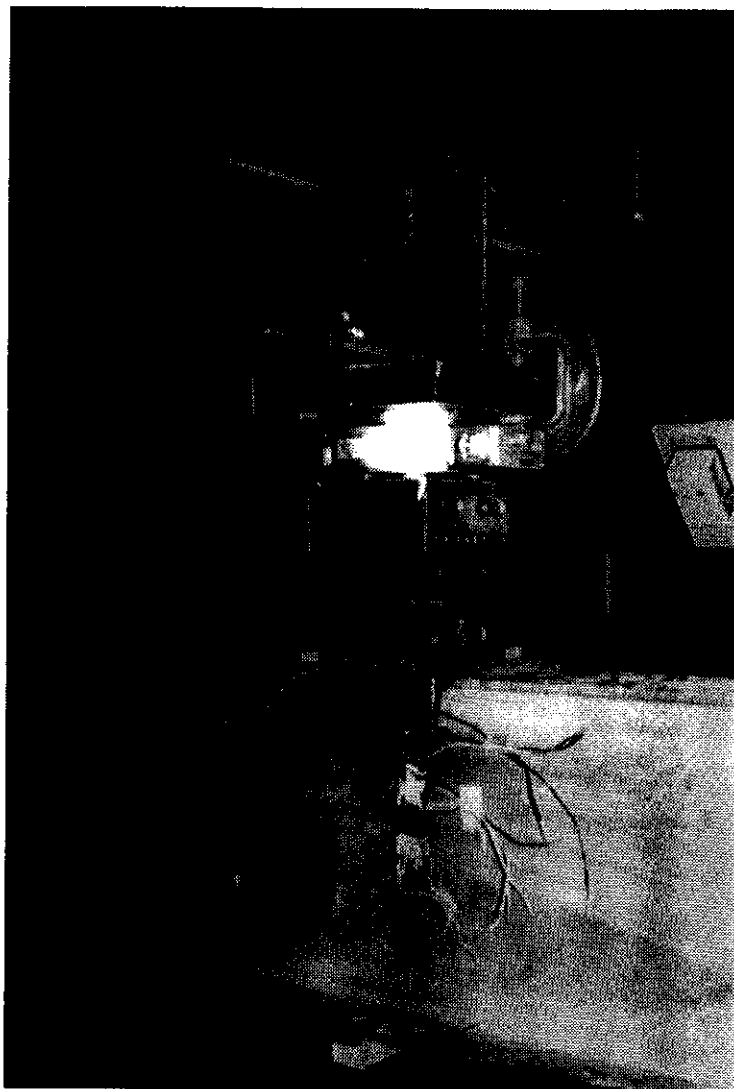
Figure 4.9
Test Apparatus
Load Frame Boundary Condition
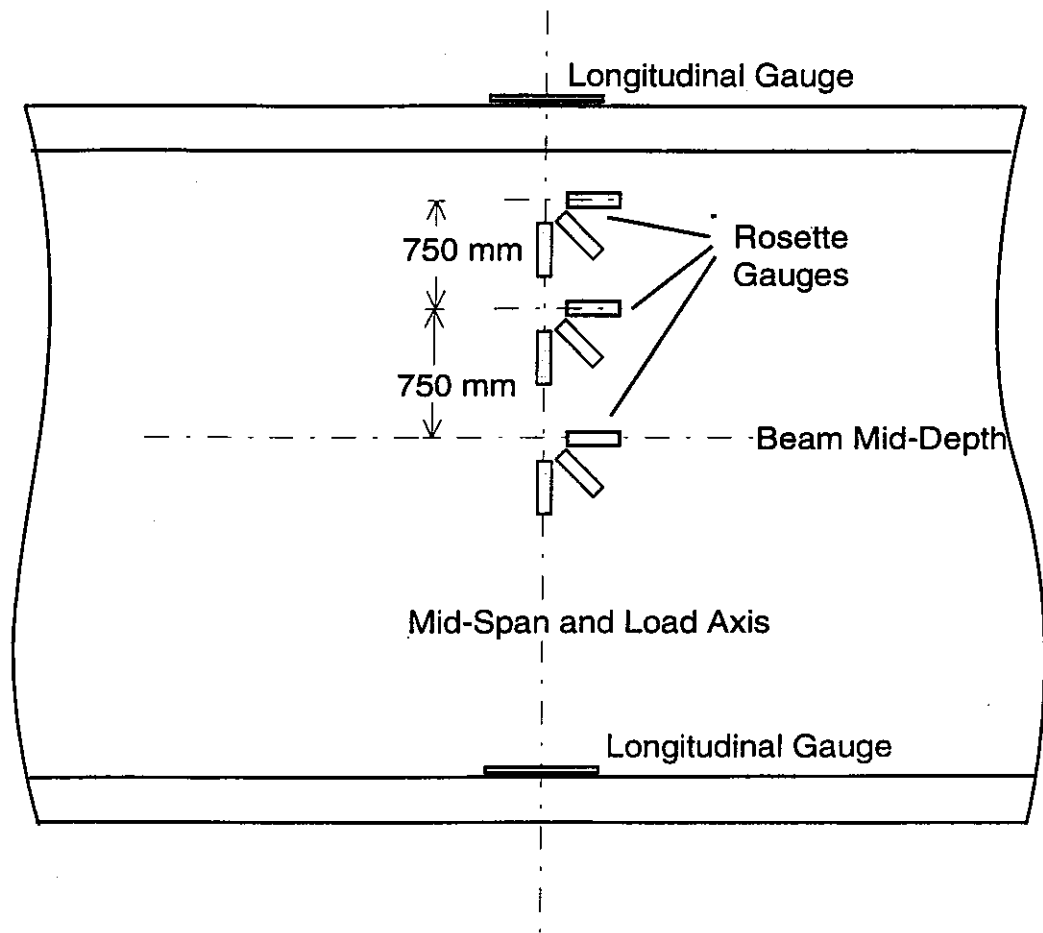
Figure 4.10
Strain Gauges Below the Load Point

Strain Gauge
Locations

Mid span

Specimen

4 @ 916 mm
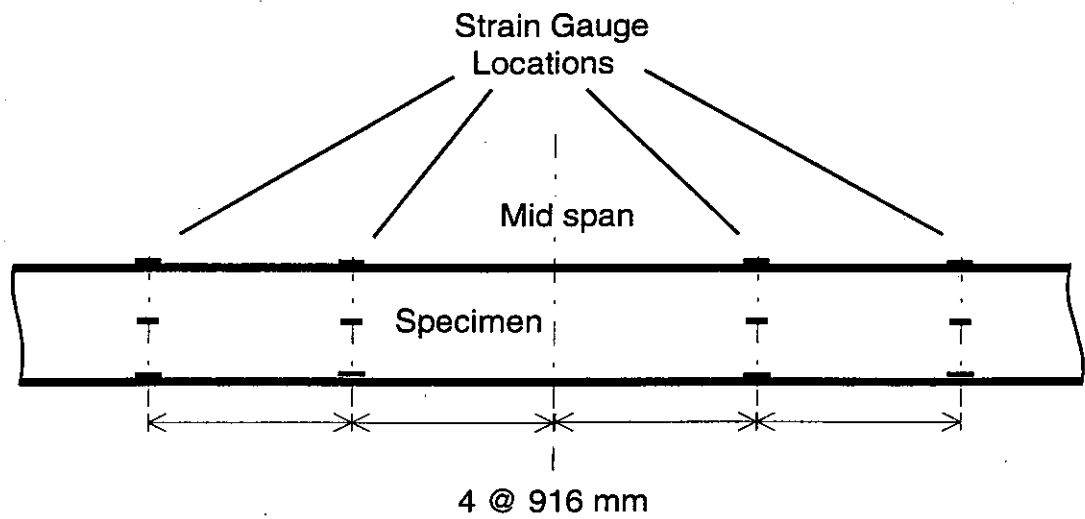
— Strain Gauge

Figure 4.11
Flexural Gauges
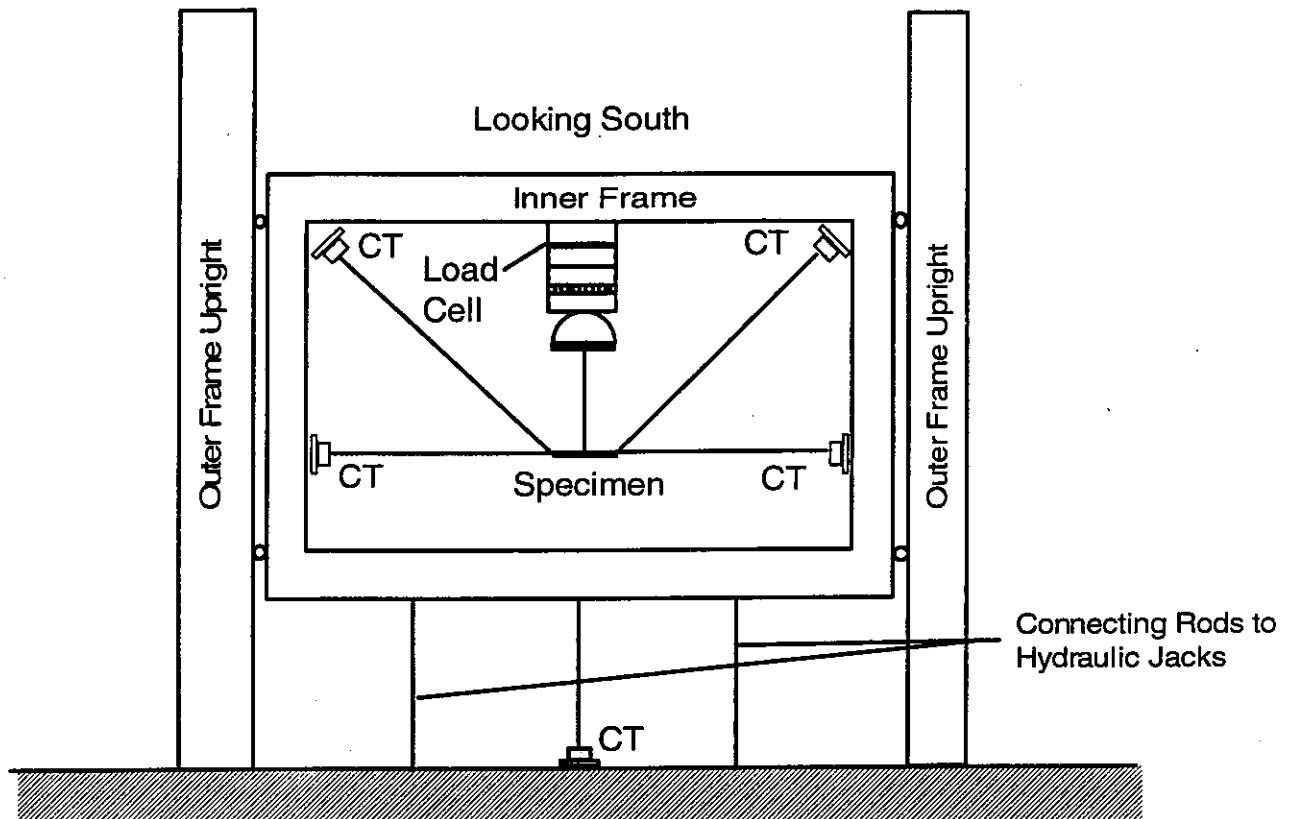
Figure 4.12
Inner and Outer Frame

Dial Gauge Δ_1

Inner Load Frame

Load Cell

Hemisperical Head

Jack

Dial Gauge Δ_2
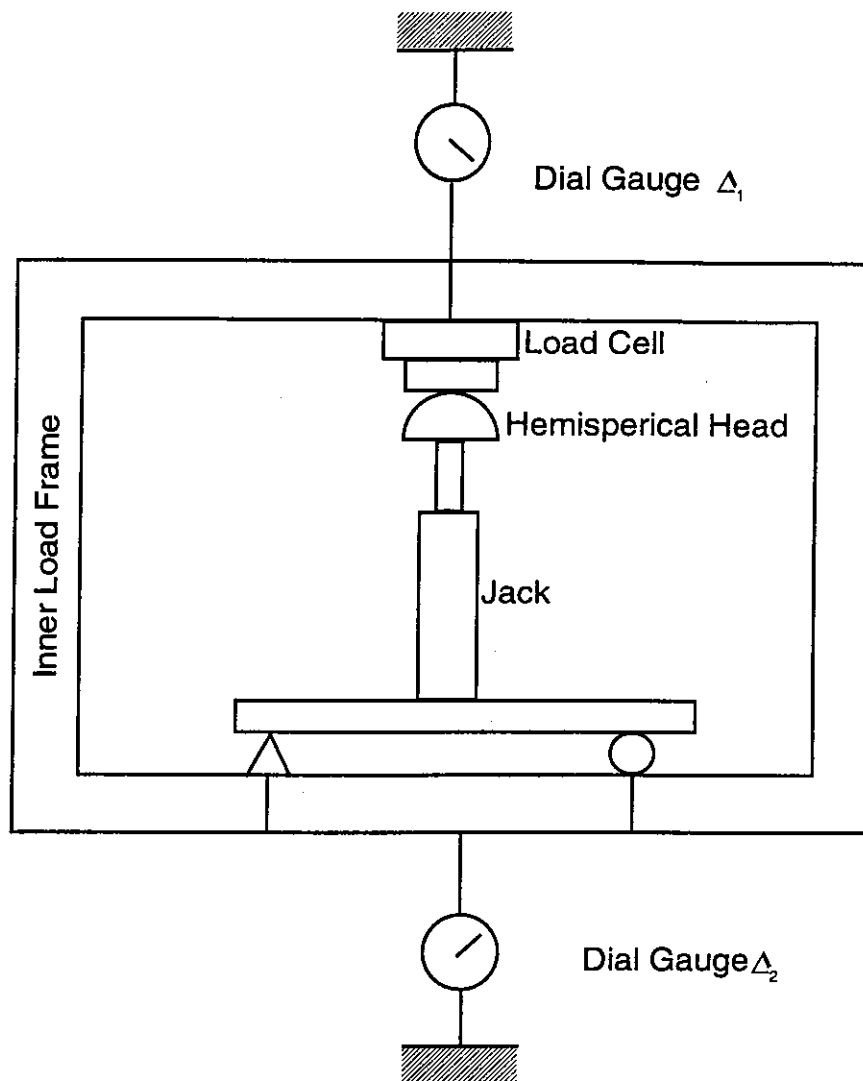
Figure 4.13
Inner Load Frame
Deflection Measurement

Δ_1

P

P/2   P/2

Δ_2
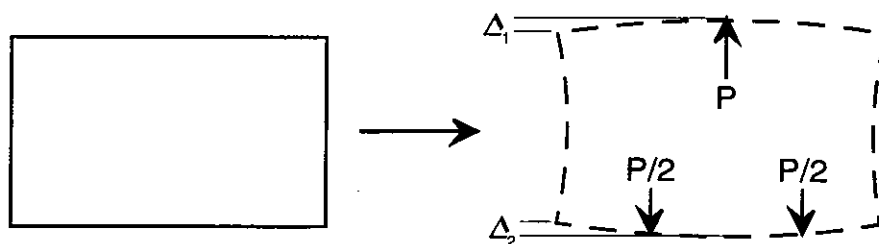
Figure 4.14
Schematic of Deflection Measurement
Inner Load Frame
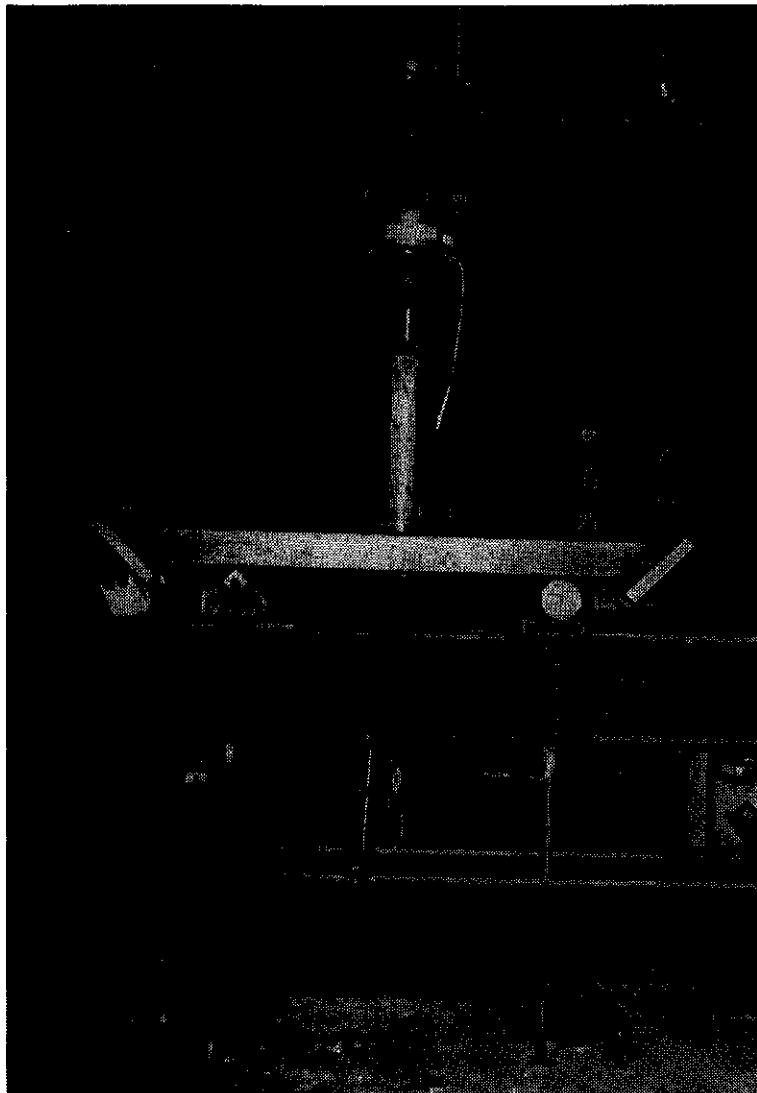
Figure 4.15
Deflection Measurement
Inner Load Frame
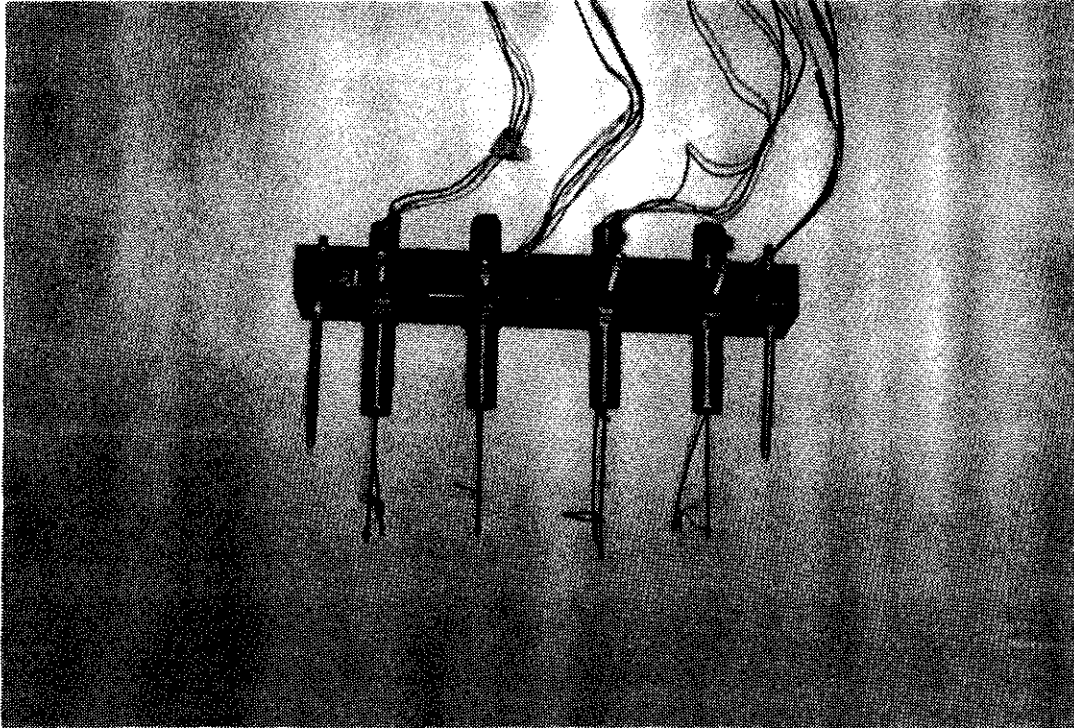
Figure 4.16
LVDT Bank
Web Deflection Measurement

= Contact Points, n = Measurement number with arrows to indicate
direction.
n

x = Deflection measurement location.

Designations, e.g. A3 refer to a measurement made by L.V.D.T. "A" during
measurement number 3.
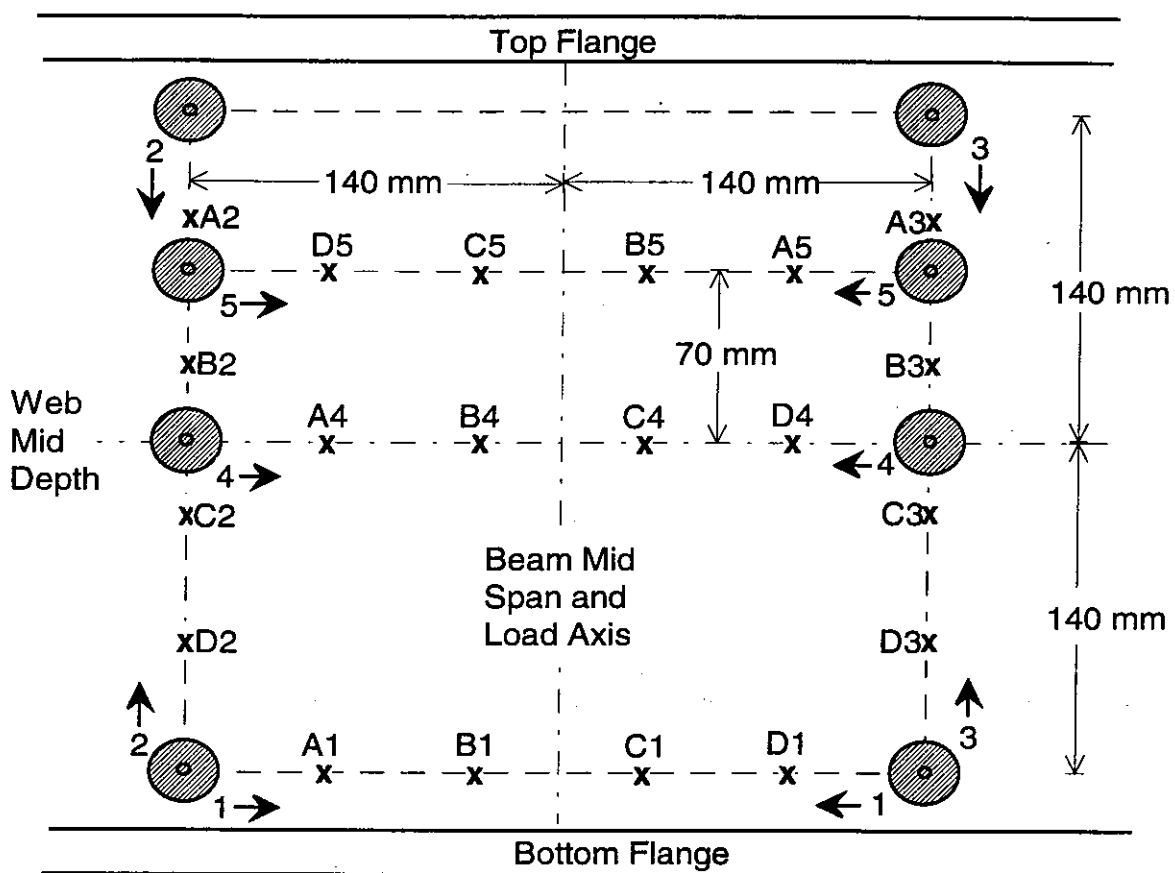
Figure 4.17
Web Deflection Measurement Grid

Plan view of bottom flange

N

Beam Mid-Span and Load Axis

Bottom flange

CT1 CT2 CT3 CT4 *CT5

5 @ 611 mm

Inner load
frame

Cable transducer support beam
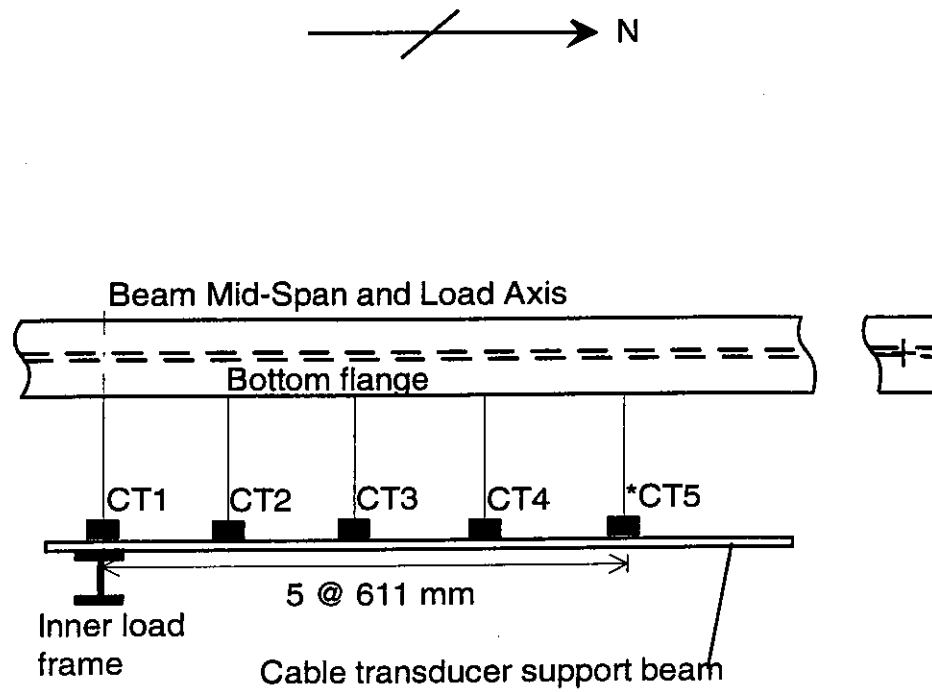
* CT5 was removed for tests 2 and 5 since the specimen
   was too short for attachment.

Figure 4.18
Location of bottom flange
cable transducers

5. FULL SCALE TEST RESULTS

5.1 General

Data presented in this chapter represents raw data from the full scale testing program. Only minor mathematical data manipulation was done to reach results presented here. In depth analyses are performed in Chapter 6.

Different data reveal different aspects of a specimens behaviour and can provide insight into local, overall or combined effects in a structural system. In this case, in-plane data relate primarily to behaviour related to vertical stiffness and reveal little about buckling behaviour. Out-of-plane behaviour relates primarily to buckling mechanisms and can provide more insight buckling behaviour. Bottom flange half shapes will be used to illustrate the effectiveness of roller bearings at the end of the beam at preventing the development of warping stresses.

5.2 In Plane Data

Load versus in-plane mid-span deflection curves for each of the five full-scale tests are presented in Figures 5.1 through 5.5. After an initial linear seating portion of the test, the system stiffened and all specimens exhibited linear load deflection relationships with small out-of-plane deflections. As load levels approached 75% to 80% of the maximum test load, out-of-plane deflections increased at a greater rate and nonlinear in-plane behaviour was noted.

Test 1 was halted as a result of a sudden lateral tension flange movement of approximately 25 m, coupled with a 10% decrease in the vertical load carried and a 4 m increase in the in-plane vertical mid-span deflection. Other tests did not exhibit sudden failure but were characterized by lateral tension flange movements increasing with each load increment. Larger out-of-plane flange deflections were coupled with decreasing in-plane stiffness and a increasing rate of out-of-plane tension flange deflections with loading. Tests 3 and 4 (Figures 5.3 and 5.4) were stopped as a result of a peak load being passed. The tests were not taken far into the descending branch of the load versus in-plane deflection, since, in both cases, the specimens were to be used for further testing and could not be taken into the inelastic range. Test 5 (Figure 5.5) was halted at load of approximately 170 kN due to the observation of whitewash flaking below the load point at the base of the top flange fillet. While the test 5 specimen was not required for subsequent testing, further loading into the inelastic range was not pursued. This decision was made since, with so much energy stored in the system, the collapse of a restraint frame boundary condition was a concern.

5.2.1 Moment Diagrams

Strain gauges, located at the beam mid span and spaced at 916 m and 1832 m on either side of the beam mid-span, were used to calculate bending moments in the specimen. Moments were calculated by using elastic stress strain relationships and the equation for flexural stresses in a linear elastic prismatic beam. The derivation of the relationship used as follows:

$$[5.1] \quad M = \frac{\sigma I}{y} = \frac{\epsilon E I}{y}$$

where M=in-plane moment

y=distance from the neutral axis

I=moment of inertia of the cross section about the neutral axis.

E=Modulus of elasticity

σ=Flexural stress

ϵ =Flexural strain

Moment could be calculated using each of the measured flange strains. An average of the two results was taken to provide the final moment calculation. The in plane bending moment calculated at cross sections other than the center line used measured strain from the flanges. Top flange strain gauges were located along the flange center line and bottom flange gauges were offset from the flange center line by 10 m and placed on the top of the bottom flange. Strain gauges were placed on the specimens subsequent to placement of specimens in the load and brace frames. This made it necessary to place the bottom flange gauges on the top surface of the bottom flange since it is difficult to apply strain gauge adhesive to a bottom surface. Since the neutral axis of out-of-plane bending coincides with the flange center lines, out-of-plane bending had the potential to affect inaccurate in-plane bottom flange bending strain measurements since bottom flange strain gauges were offset from the bottom flange center line. All flange strain readings used to calculate in-plane moment were taken at load levels corresponding to small lateral tension flange deflections to minimize the effects of tension flange movement on the accuracy of calculated in-plane bending moments.

At the mid-span, flange strains were measured near the flange tips. Each measured strain represents the sum of the in-plane and out-of-plane bending strains at the gauge location. The sum of the measured flange tip strains should equal twice the in-plane bending strain, regardless of the out-of-plane moment, given that all strains are elastic. The averages of the measured strain from the flange tips were used in lieu of single measured values for the calculation of mid-span moment.

Moment diagrams for all full scale tests are presented in Figures 5.6 through 5.10 for each of the five full scale tests, respectively. Several partial moment diagrams are shown in each plot. Each curve represents moments calculated at a specific load level, as shown in the legend. The horizontal axis extends to the full length of each beam.

The family of curves can be used to estimate the location of the inflection point (I.P.) of the beam, as shown in Figures 5.6 through 5.10. If the end moment is a result of elastic restraint, the location of the inflection point should remain constant throughout the linear elastic loading of the specimen. Full scale tests can be generalized as behaving as a simply supported beam at very low load levels. As the end condition columns and other bolted connections seat, restraining stresses develop and the inflection points migrate toward the beam mid-span. With further loading, specimens developed larger out-of-plane deflections and reduced in-plane stiffness. As in-plane stiffness of the test specimens decreased, the stiffness of the end restraint remained constant and the ratio of the end restrain stiffness to the member stiffness increased. With the changing stiffness of the member relative to its' restraint, further migration of inflection points toward the beam mid-span was observed.

Moment diagrams corresponding to approximately 0.5 of the test peak load were used to calculate the location of the inflection points shown in Table 5.1.

Moment diagrams corresponding to larger out-of-plane deflections were omitted from Figures 5.6 through 5.10. This was done to clarify the location of the inflection points.

Knowing the location of the inflection points allows calculation of the rotational stiffness of the end conditions and the magnitude of the beam end moments as a function of load. Comparison of the north and south end condition, presented in Table 5.1, indicates that they provided similar restraint to each ends of each beam for all tests.

A theoretical comparison of short beams to longer beams of the same cross section and end restraint stiffness reveals that, for a given mid-span moment, shorter beams experience smaller restraining moments than longer ones. As beam length decreases, flexural stiffness increases. As beam flexural stiffness increases and end restraint stiffness remains constant, the ratio of restraining stiffness to member stiffness decreases. This results in a relocation of the inflection points toward the end of the beam and a corresponding decrease in the magnitude of the end moment to mid-span moment ratio. This was not observed in the full scale tests (Tests 4 and 5 specifically) and can be attributed to the presence of the initial seating portion of the tests. During initial seating, in-plane mid-span moments increase without substantial increase in end moment, thereby modifying the ratio of mid-span to end moment throughout the test.

End moments, inflection point locations and in-plane stiffnesses are summarized in Table 5.1.

5.2.2 In-Plane Stiffness

In-plane mid-span deflections of the test beams were measured throughout the tests and can be compared to the theoretical in-plane mid-span deflections for verification of test validity. Theoretical mid-span deflections were calculated by superposition of the deflection corresponding to the mid-span load and deflection corresponding to the negative end moment determined using the inflection points identified in Figures 5.6 through 5.10). The superposition results in an in-plane deflection given by (eq. 30, Beam Diagrams and Formulae, CISC Steel Design Handbook, (1991)):

$$[5.2] \quad \Delta = \frac{Pl^3}{72EI}(2-3\alpha)$$

where:

P = In-plane mid-span point load

Δ=In-plane beam deflection (at mid-span)

l = Beam length

E = Modulus of elasticity

I = Strong axis moment of inertia

α = Restraining moment/(Pl/4)

The theoretical deflection curve is shown with the experimental in Figures 5.1 through 5.5. The theoretical deflection curve depends on measured values of modulus of elasticity, specimen dimensions and restraining moment to mid-span moment ratio. Poor agreement between measured in-plane

deflections and theoretical deflections can be attributed to the measured restraining moment to mid-span moment ratio. During the test, the ratio varies while a value representative of behaviour between specimen seating and loss of in-plane stiffness was used for the calculation of the theoretical curve.

5.3   Out-of-Plane Data

Out-of-plane data are available from two sets of apparatus. The half deflected shape of the bottom flange is available from the cable transducer data, taken at several locations along the bottom flange. The shape of the mid-span cross section can be assembled by locating the bottom flange in space using cable transducer data, and combining local web deflections, measured by LVDT, to provide a composite of the web cross section shape at selected load levels.

5.3.1   Lateral Tension Flange Movement

Figures 5.11 through 5.15 present the load versus out-of-plane deflection curves for the east and west tip of the bottom flange mid-span. Test 1 (Figure 5.11) exhibited very abrupt lateral movement of the tension flange which can be clearly seen in the figure. Test 2 and Test 3 were characterized by gradually increasing deflections as shown in Figure 5.12 and Figure 5.13.

Test 4 (Figure 5.14), unlike other tests displayed a relatively linear load versus out-of-plane tension flange movement curve. Test 4 was halted because a peak load had been attained.

The load versus out-of-plane deflection curve of the mid-span flange tip for test 5 (Figure 5.15) has a short, almost vertical portion at loads from approximately 133 kN to 160 kN. This was likely caused by dirt or debris interfering with the smooth operation of the boundary conditions at one or more of the brace points. At a load of approximately 165 kN, the out-of-plane deflection of the tension flange continued until unloading commenced at a load of approximately 170 kN.

The half shapes of the deflected bottom flanges are shown in Figures 5.16 through 5.20. Each plot presents several curves. Each curve represents the out-of-plane deflected shape of the bottom flange, from the load axis (at the right of the figure) to the support (at the left of the figure), at a specified load. Different load levels and their corresponding line types are shown in the legend.

Figures 5.21, 5.22 and 5.23, photographs of the loaded beams, clearly show the presence of the web sweep and cross section rotation at the beam center. The photographs also indicate the lack of out-of-plane web deflection.

5.3.2   Mid-Span Cross-Section Distortions

The array of twenty deflection measurements collected from the LVDT bank placed in the area below the load point were assembled to produce contour plots of web deflections relative to the two flange roots. Finite element solutions indicated that the beam bucked shape would have maximum web deflections greater than the mid-span tension flange deflection (see Figures 6.13 through 6.17). The full scale test data shows that the largest measured web distortion for all tests was less than 0.3 m, much smaller than the measured

tension flange movement, which was typically greater than 10 m. Contour plots of web distortions showed that there was no observable trend in web distortions over the area of the web. The web bulge expected from the finite element modelling and the model testing was not observed in the any of the full scale tests. One contour plot is shown in Figure 5.24. Others were omitted since they showed similar results.

5.4   Stresses and Strains

5.4.1   Vertical Stresses Below the Load Point

The six rosettes placed on each side of the web were used to calculate the vertical stresses below the load point. Vertical stresses were calculated using horizontal and vertical strain measurements from the rosettes and an assumed Poissons ratio = 0.3 as follows:

$$[5.3]\ \sigma_x = E(\epsilon_x - \nu\epsilon_y)\ ;\ \sigma_y = E(\epsilon_y - \nu\epsilon_x)$$

where:

E = Modulus of elasticity

ϵ_i = Strain in the i direction

σ_i = Stress in the i direction

ν = Poissons ratio (assumed = 0.3)

Strain readings from the 45° rosette gauge were eliminated from the calculation since near zero strain readings were reported for all load levels on all tests (corresponding to the lack of shear strain along the load axis). Plots of the stresses at mid span load P=50 kN are shown in Figure 5.25. The stresses

shown in the plot are an average of the vertical stresses on opposite sides of the web of all beams sharing the same cross section. This was done to remove web bending effects and to report stresses below the load point for beams sharing cross-section dimensions, regardless of their length. The plots also present the Yura theory assumption of stress variation below the load for comparison.

The disagreement between the *Yura* theory triangular vertical stress distribution assumption and measured vertical stresses in the full scale tests was first identified by *Summers* (1982) when comparing finite element predictions of stresses below concentrated loads to the *Yura* assumption. The use of a triangular stress distribution is conservative and would lead to low estimates of failure load (as observed in the model tests). This discrepancy was acknowledged in earlier research, but was not eliminated from the model to ensure conservative failure load estimates. The Revised *Yura* Theory, presented in Figure 1.7, included a vertical web stress distribution similar to that measured in the full scale tests.

5.4.2 Strain in the Bottom Flange

In the initial stages of loading, the two flange tips of the bottom flange mid-span have similar load-strain relationships. As loading progresses, the bottom flange develops out-of-plane deflections. The out-of-plane sweep in the bottom flange superimposes bending strain on the strain observed as a result of in-plane flexure. The presence of this out-of-plane flexural strain can be observed as a splitting of the load versus bottom flange tip strains. The observed variation between flange tip strains is very small (except in cases of flange tip yield (Figure 5.28, Test 3, Top East). To rationalize the observed

strain variation between flange tips, consider a flange, 6000 m long by 127 m wide, bent in an arc such that the mid-span deflects 30 m (approximately equal to test 1 at maximum lateral deflection). The resulting radius of curvature is approximately 150 000 m. The difference in strain between the flange tips can be estimated by using the following relationship:

$$[5.4] \quad \Delta\epsilon \approx 1 - \frac{r - 0.5w}{r + 0.5w}, \quad r \gg w$$

where: $\Delta\varepsilon$ = difference in strain between the flange tips

r = the radius of curvature of the flange

w = the flange width

The difference in strain between the flange tips is approximately 846 microstrain. This value corresponds with the observed difference in strain of the bottom flange of test 1 (Figure 5.26) which deflected laterally approximately 31 m. Tests 2 through 4 (Figures 5.27 through 5.30) were stopped at smaller lateral tension flange deflections and, therefore, exhibit smaller differences between flange tip strains

Flange tip strains are shown in Figures 5.26 through 5.30.

5.4.3   Strain in the Web

Throughout testing, the strain state on opposite sides of the web was recorded. Any difference between opposing web strain measurements would indicate bending in the web caused by cross section distortion, web buckling or the combined effects of the two. Both finite element analysis and model

testing indicated that web buckling could be expected part of the tension flange movement failure mode

Figures 5.31 is load versus measured vertical strain for all six vertical web strain gauges in test 1. While load versus vertical strain curves are divergent, there are no observed asymptotes and no discernible divergence of strain on opposite sides of the web to indicate an overall bending of the web or the development of a buckle. This observation correlates with the lack of significant measured out-of-plane distortion of the web throughout the loading histories of all full scale specimens. Other vertical web strain plots were omitted since they also exhibited no asymptote or divergent trends.

Table 5.1

End Moments

TEST	L (m)	I.P. N (m)	I.P. S (m)	L2 (m)	α	k (kN/m)
Test 1	6261	2539	2402	4940	0.210	3.54
Test 2	5039	2350	2350	4700	0.067	5.25
Test 3	7482	2160	2070	4230	0.435	5.12
Test 4	6261	2910	2870	5780	0.077	3.43
Test 5	5039	2280	2196	4476	0.112	7.00

Where

L = Beam Length

I.P. N = Distance of inflection point from the beam north support

I.P. S = Distance of inflection point from the beam south support

L2 = Length of beam between inflection points

α = Restraining moment / (PL/4)

k = In-plane beam stiffness

Note: All end moments were calculated at load $\approx$ 50% test peak load
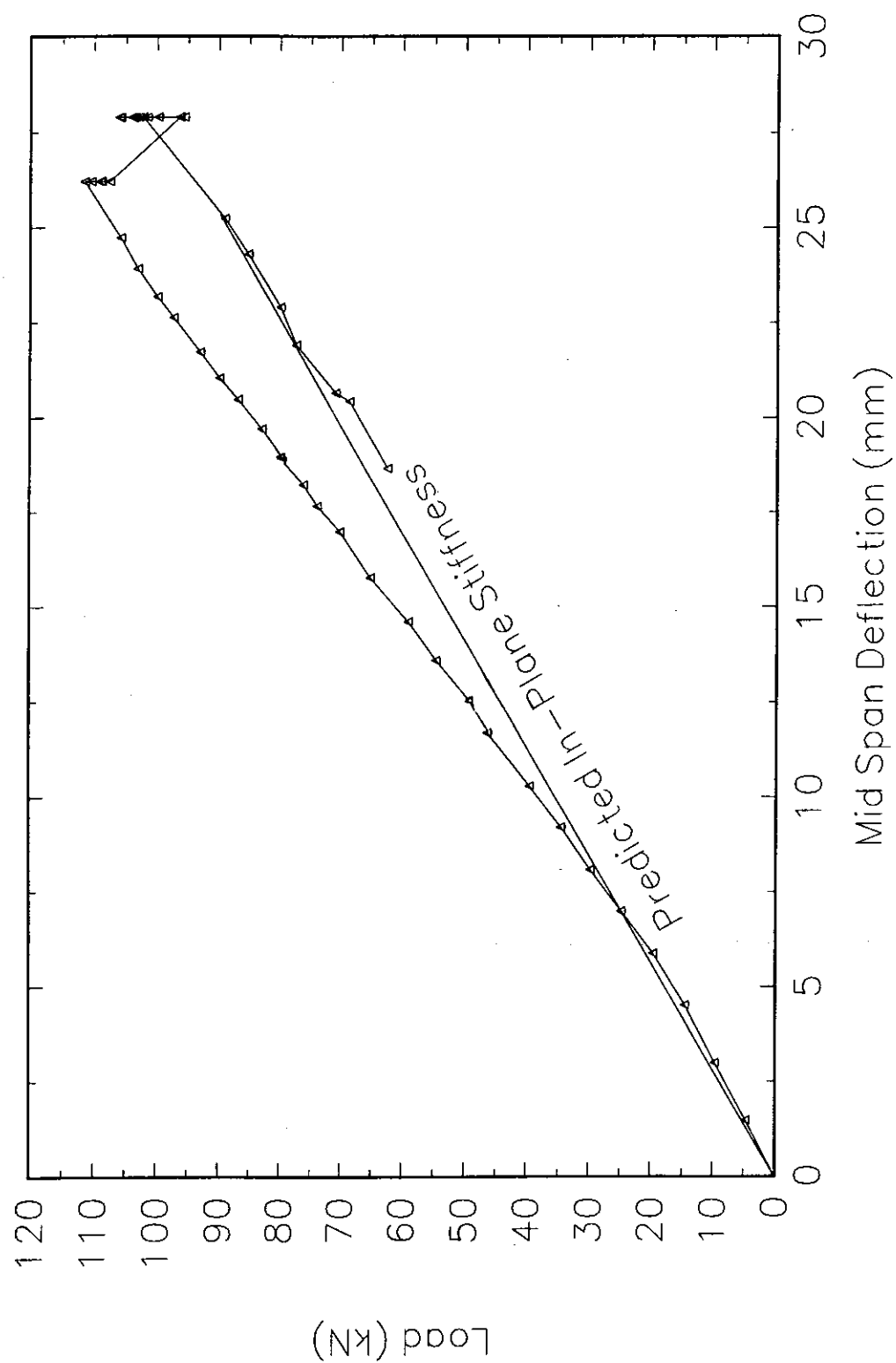
Figure 5.1
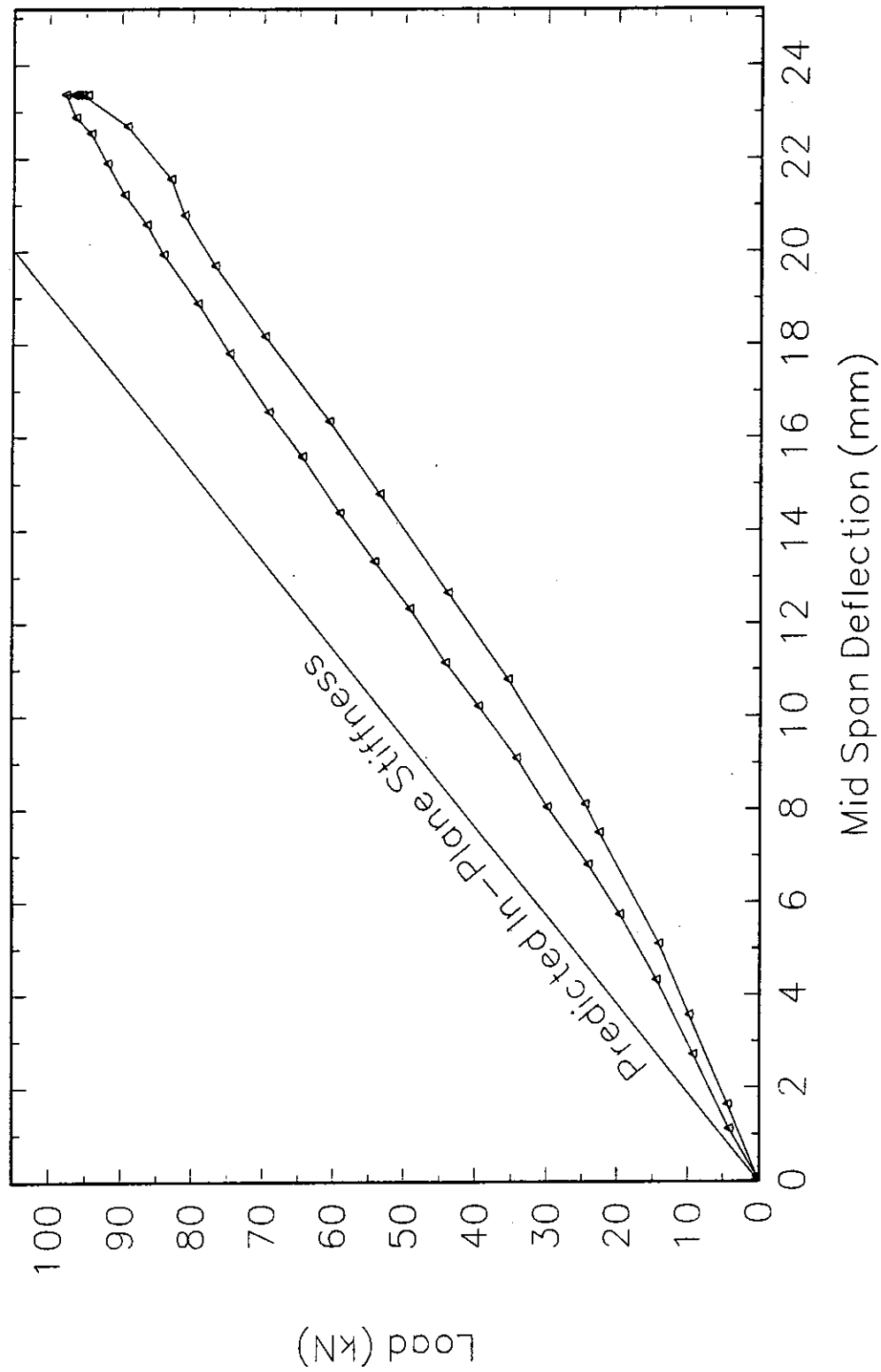Load versus Mid-Span Deflection
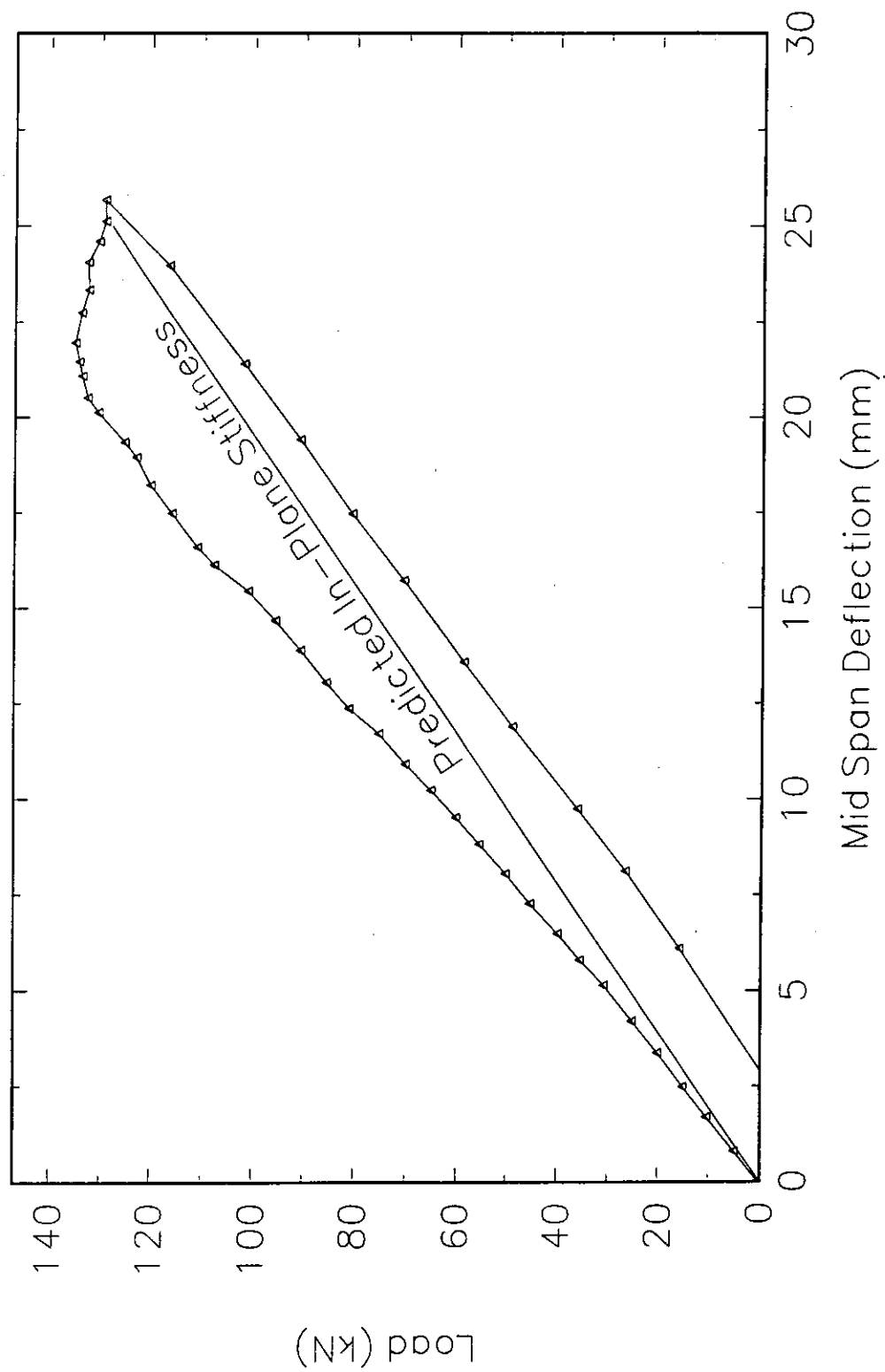Test 1

Figure 5.2
Load versus Mid-Span Deflection
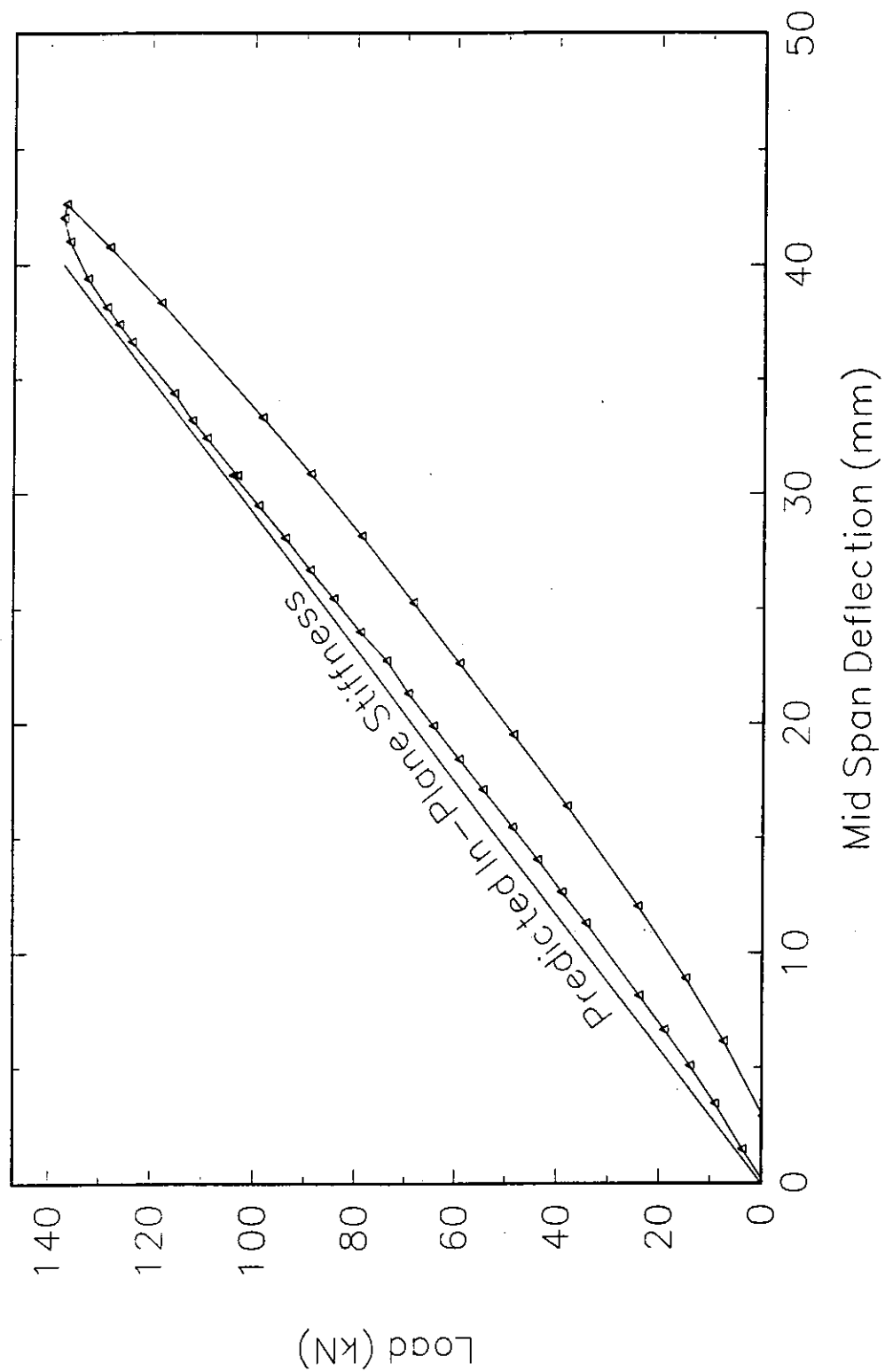**Test 2**

Figure 5.3
Load versus Mid-Span Deflection
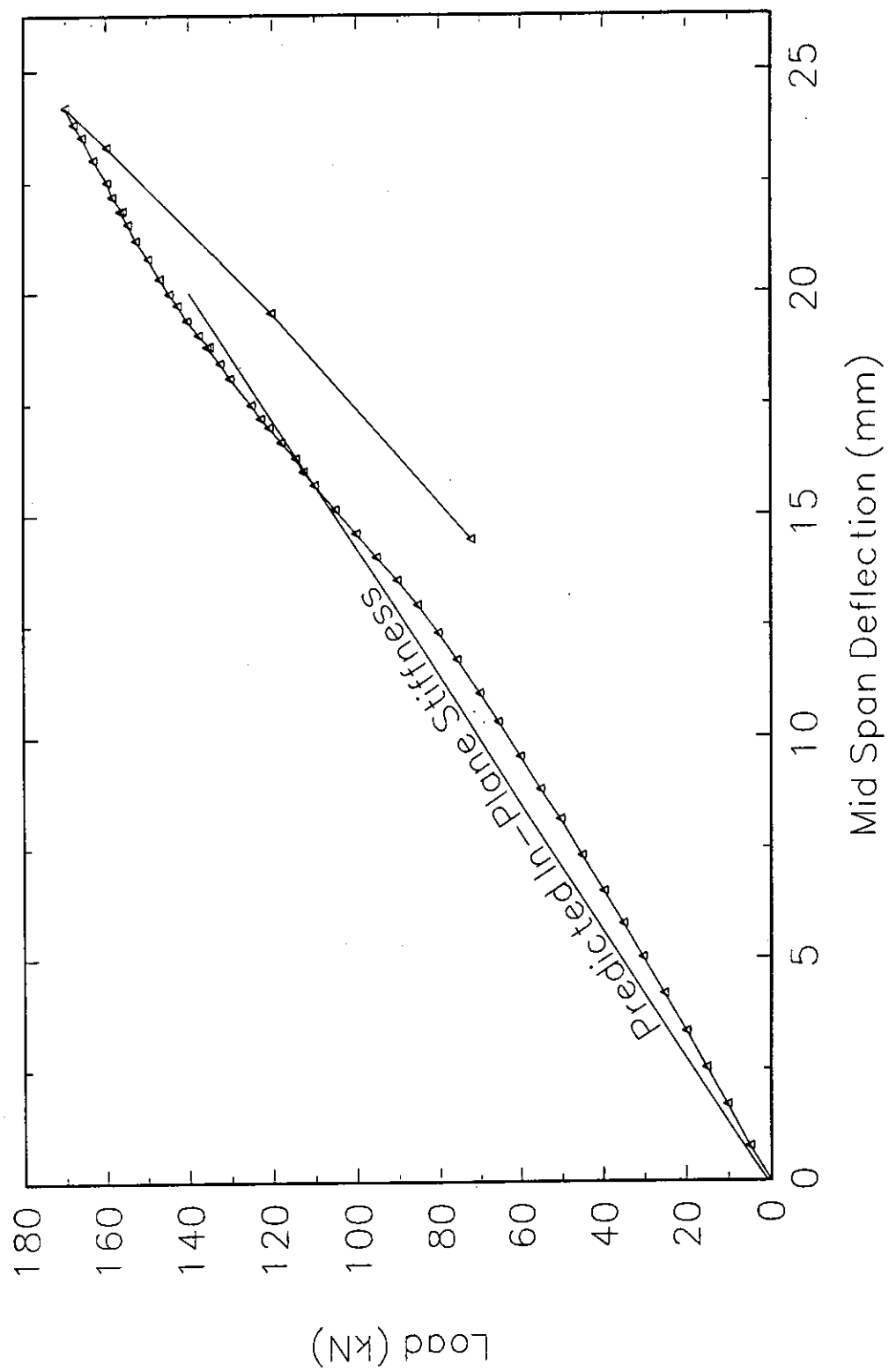Test 3

Figure 5.4
Load versus Mid-Span Deflection
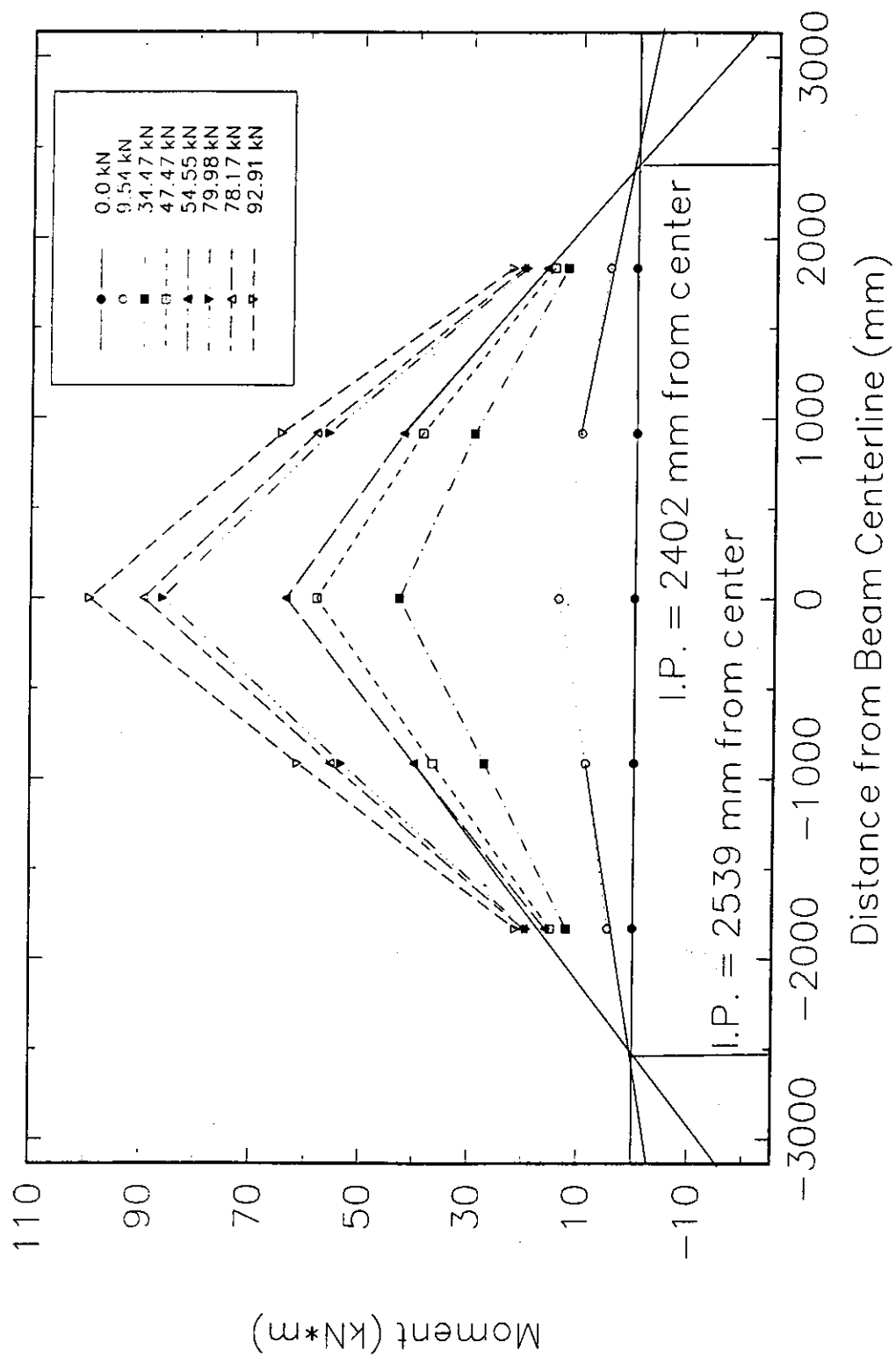**Test 4**

Figure 5.5
Load versus Mid-Span Deflection
Test 5

Figure 5.6
In-Plane Moment Diagram
Test 1
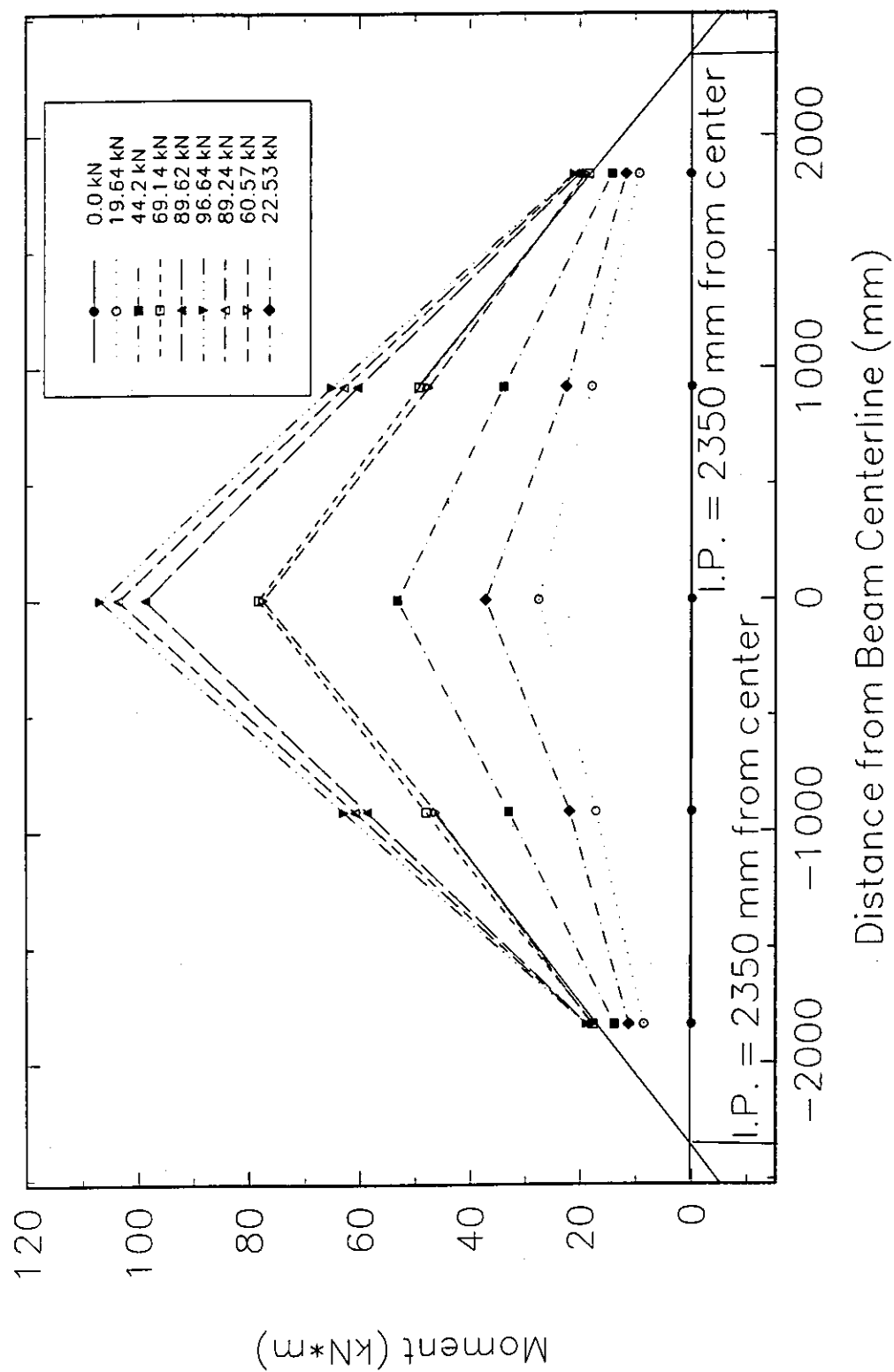
Figure 5.7
In-Plane Moment Diagram
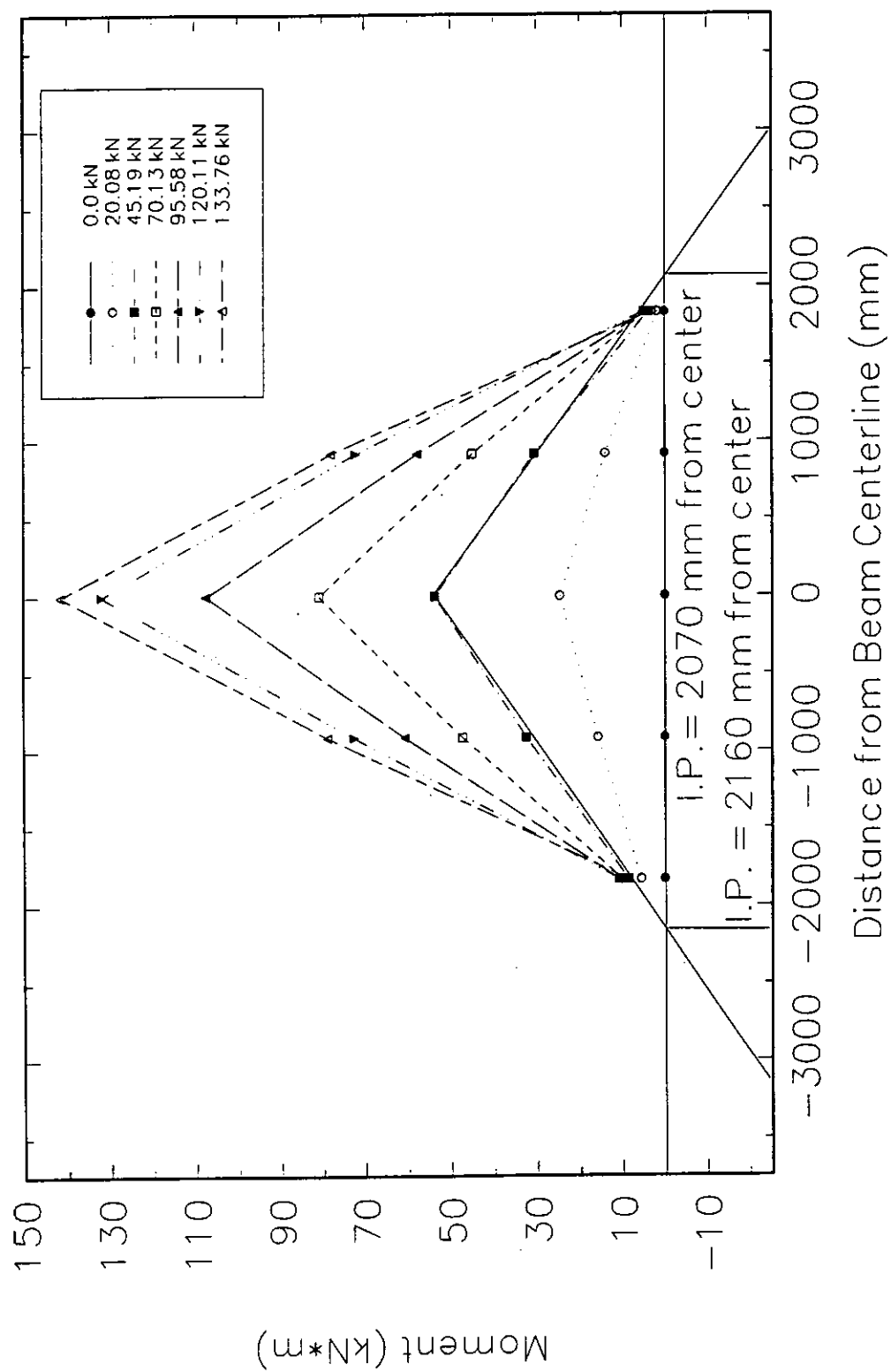**Test 2**

Figure 5.8
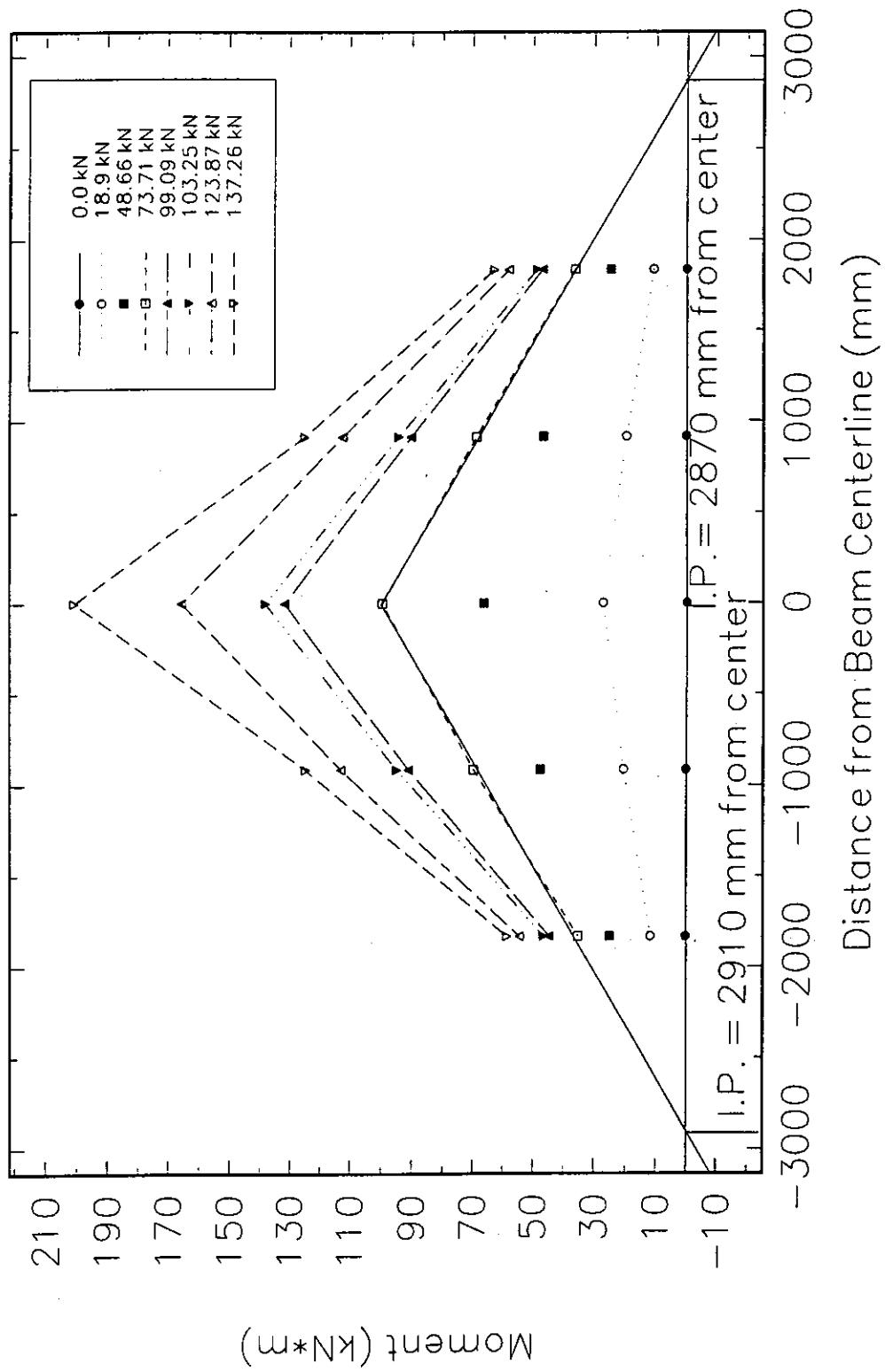**In-Plane Moment Diagram**
Test 3

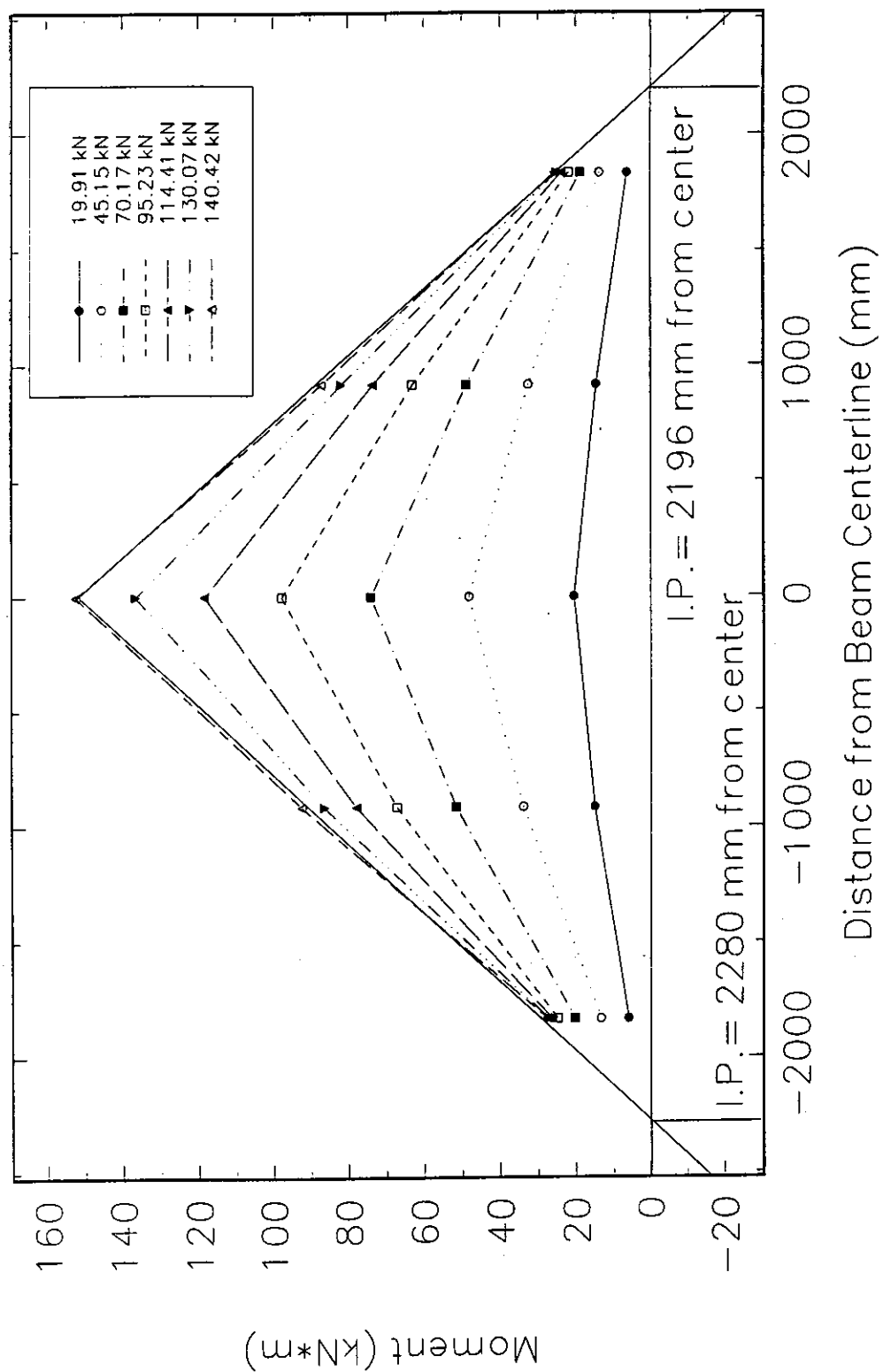**Figure 5.9**
In-Plane Moment Diagram
Test 4

Figure 5.10
In-Plane Moment Diagram
Test 5

Figure 5.11
Load versus Lateral Tension Flange Movement
Test 1

Figure 5.12
Load versus Lateral Tension Flange Movement
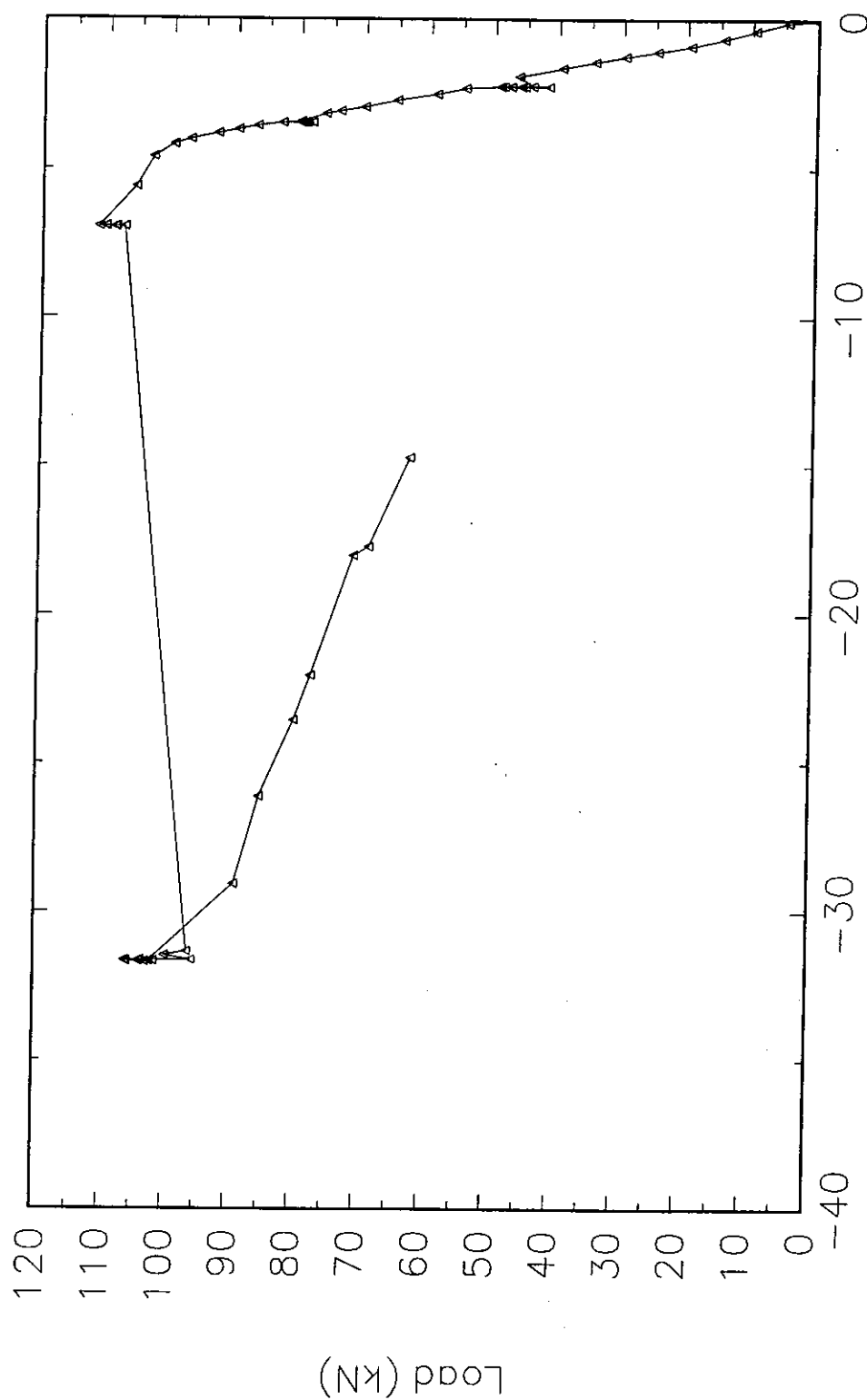**Test 2**

Lateral Tension Flange Displacement (mm)
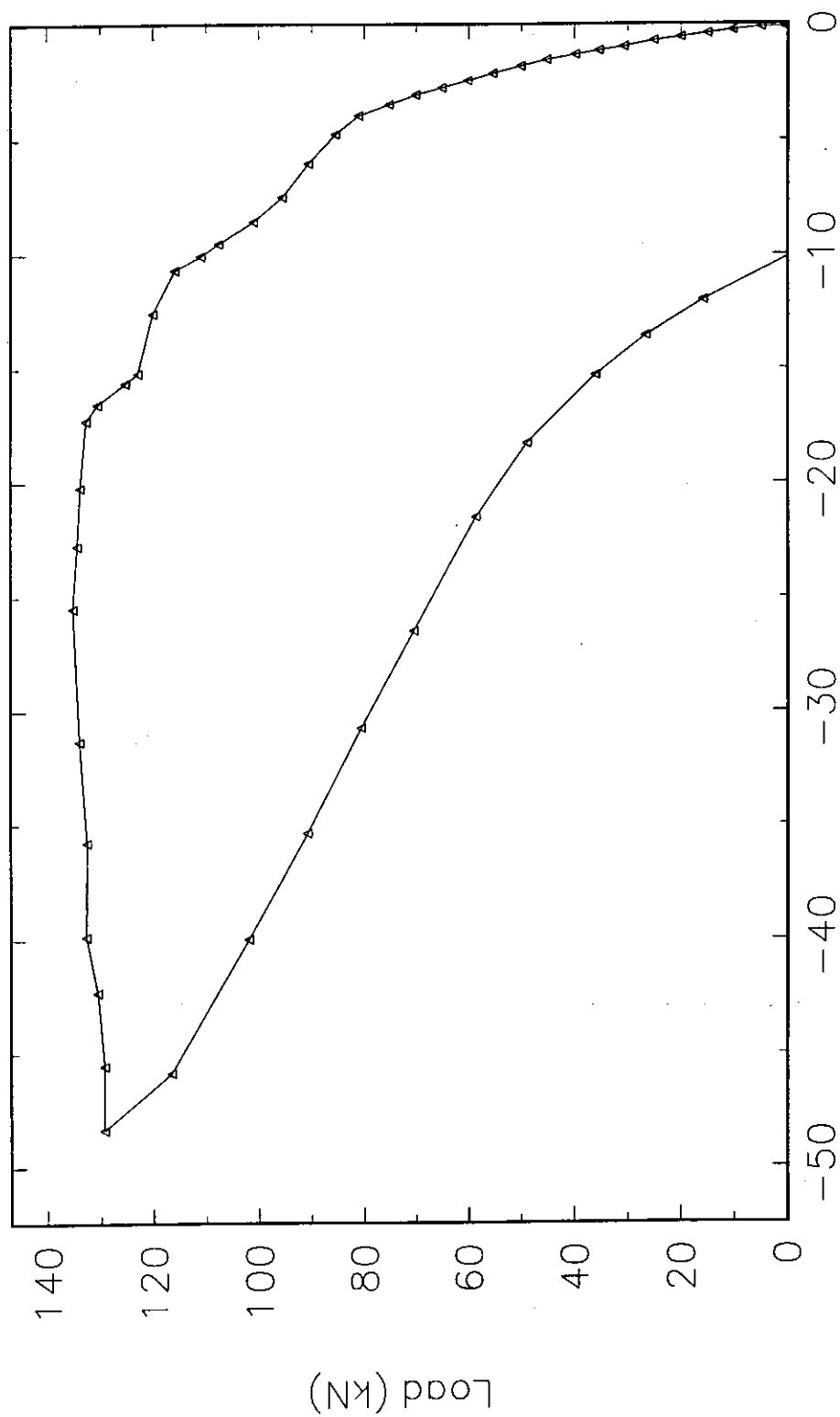
Figure 5.13
Load versus Lateral Tension Flange Movement
Test 3

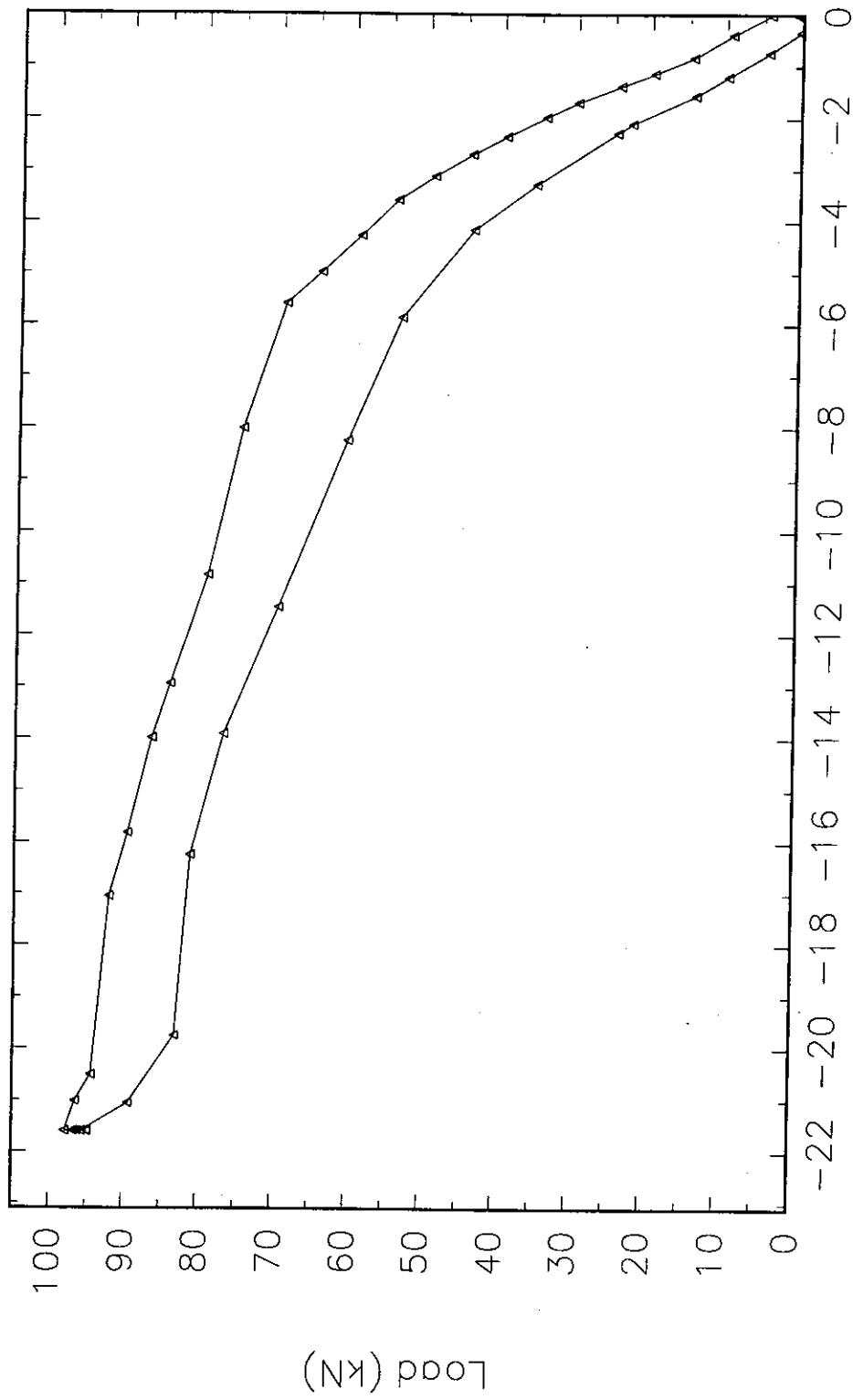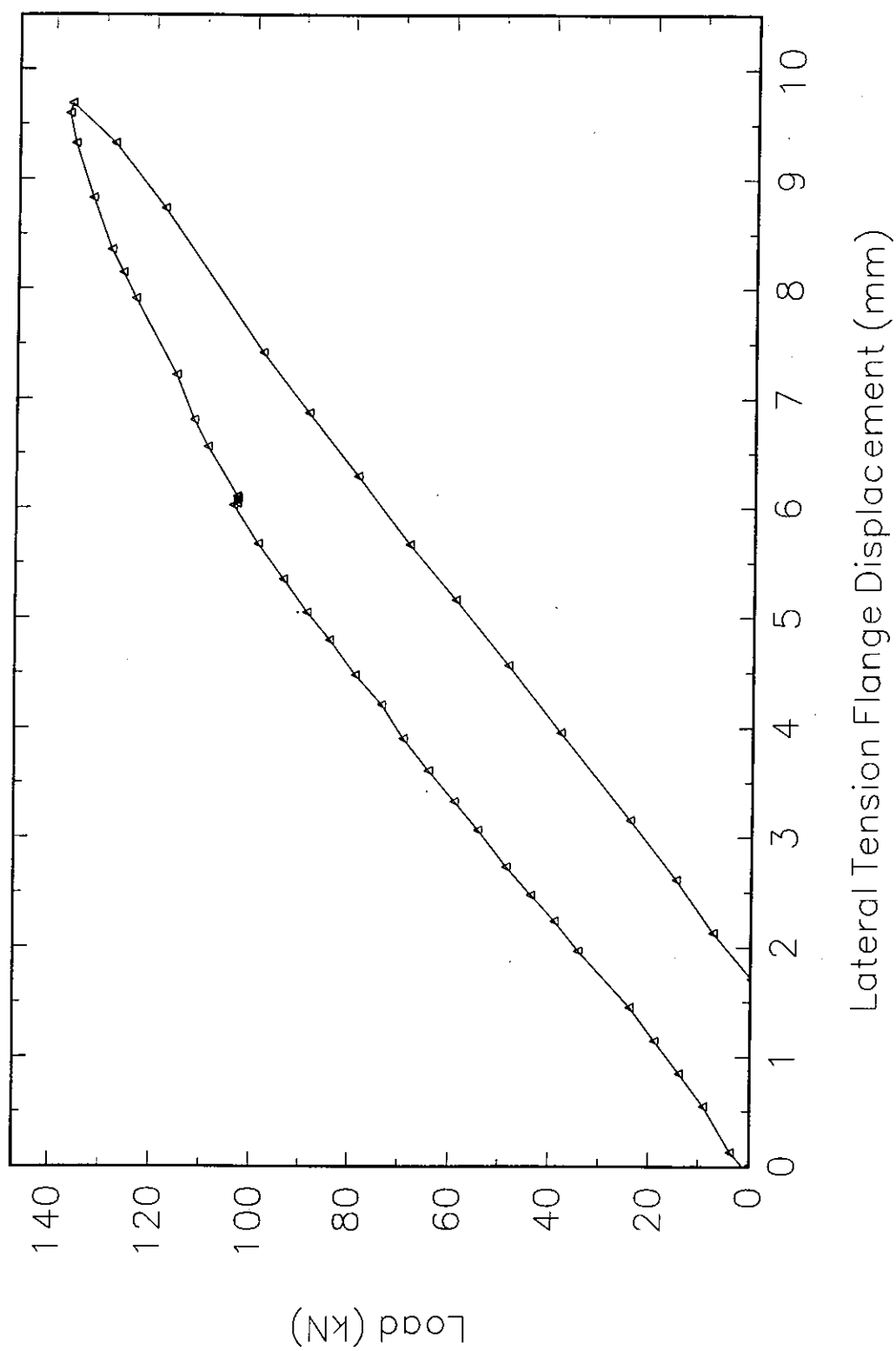**Figure 5.14**
Load versus Lateral Tension Flange Movement
Test 4
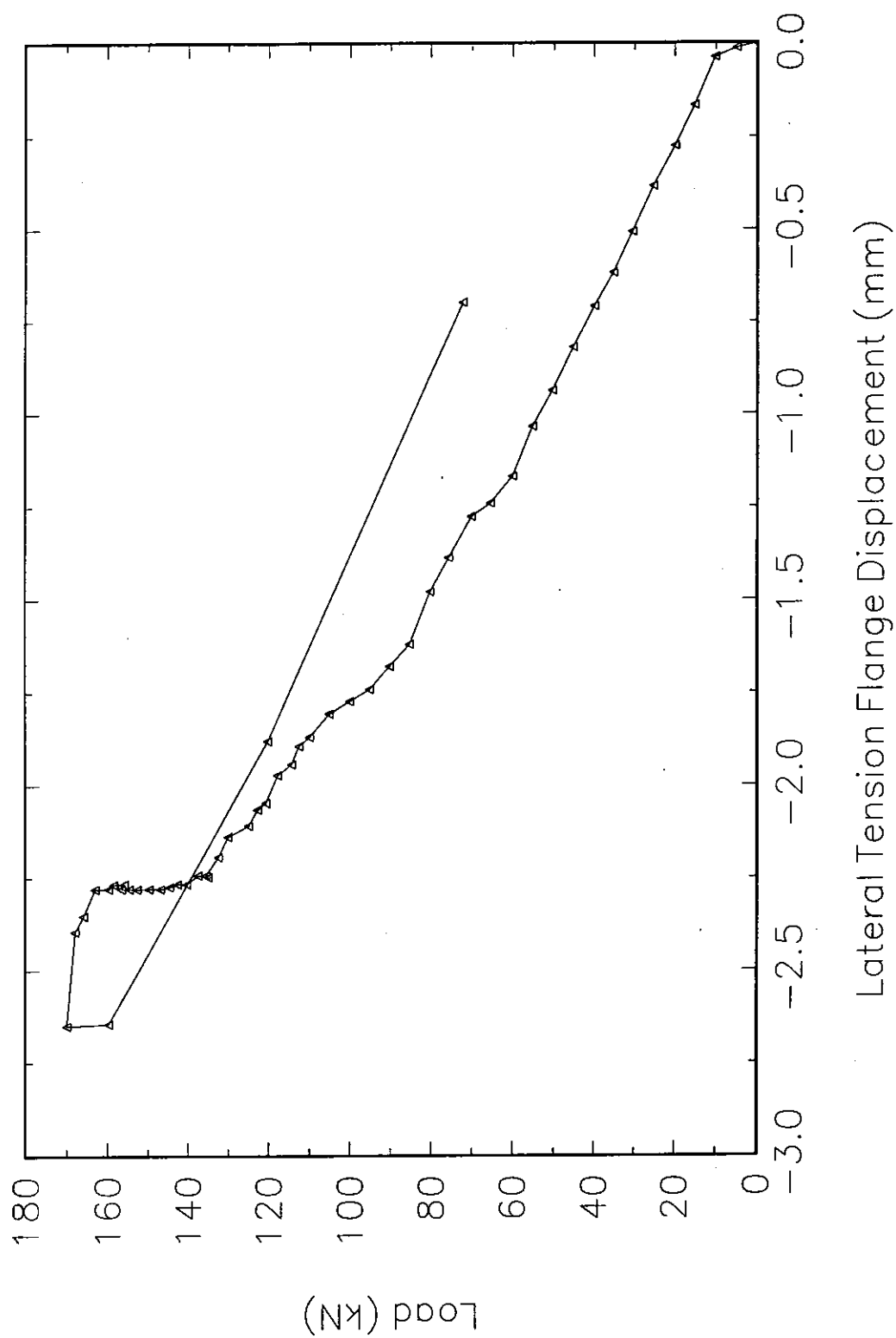
Figure 5.15
Load versus Lateral Tension Flange Movement
Test 5
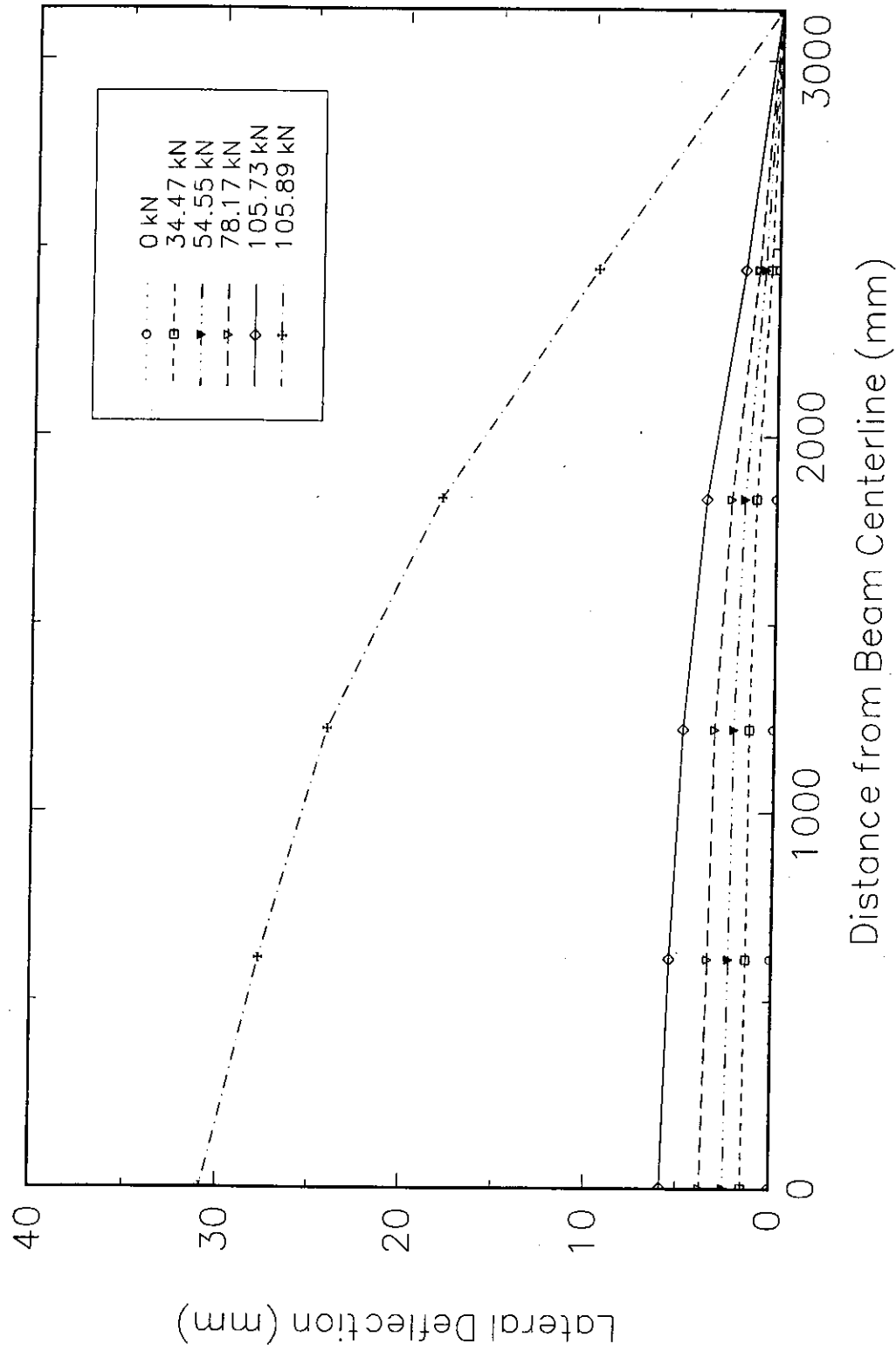
Figure 5.16
Bottom Flange Half Shape
Test 1

Legend:
- ○ 0 kN
- ▣ 34.47 kN
- ▼ 54.55 kN
- ✧ 78.17 kN
- ◇ 105.73 kN
- + 105.89 kN

Distance from Beam Centerline (mm)

Lateral Deflection (mm)
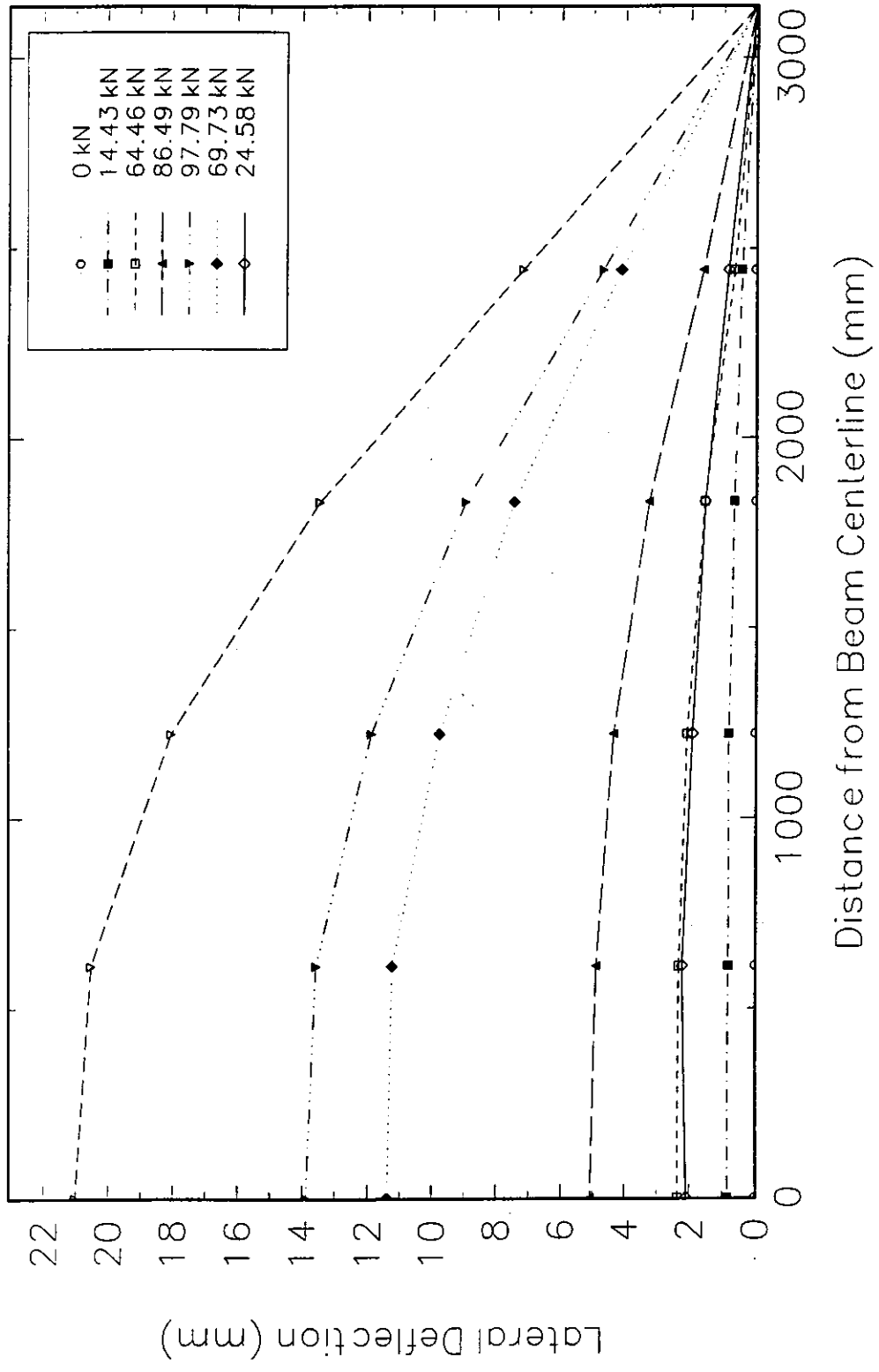
Figure 5.17
Bottom Flange Half Shape
Test 2
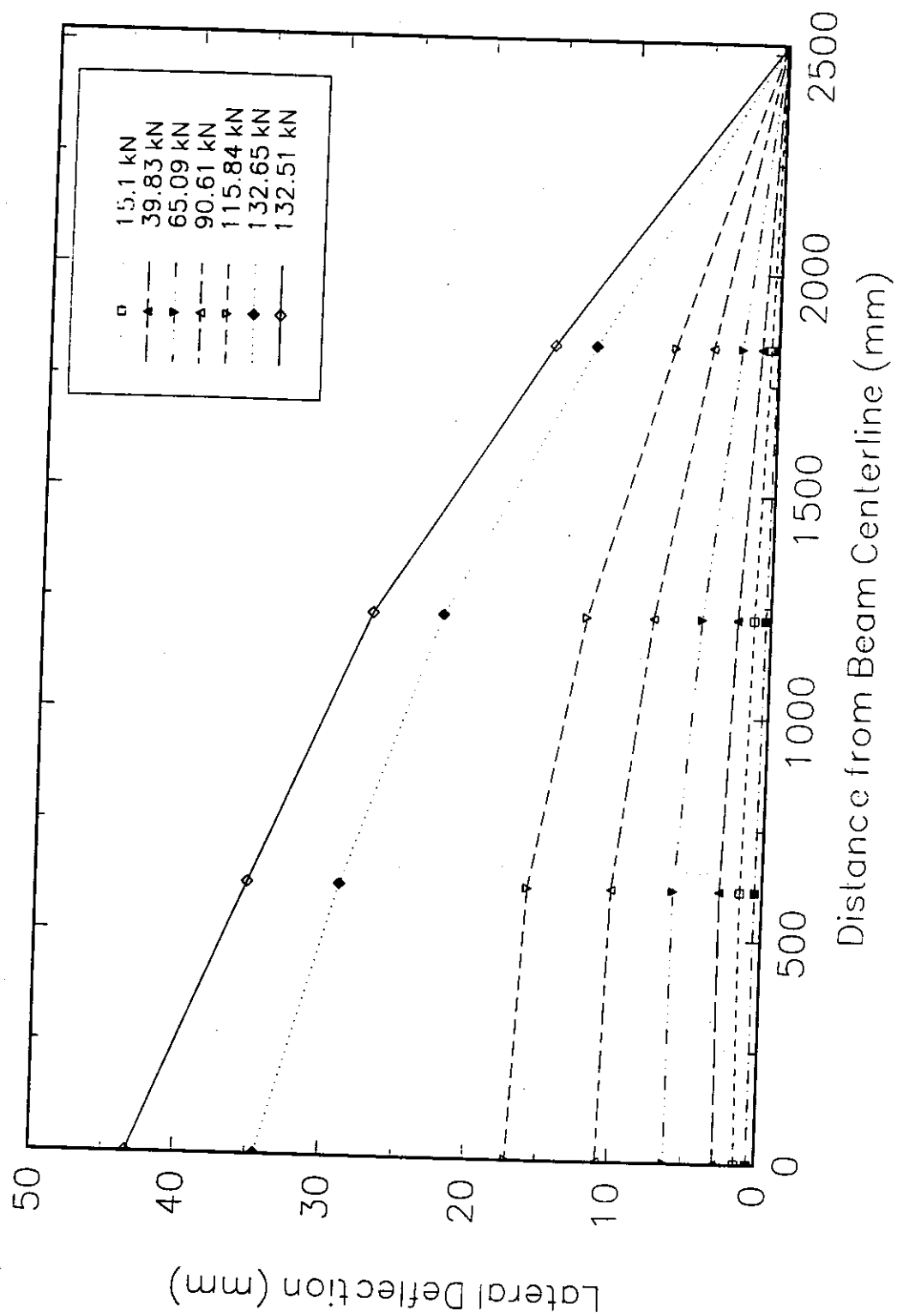
Figure 5.18
Bottom Flange Half Shape
Test 3
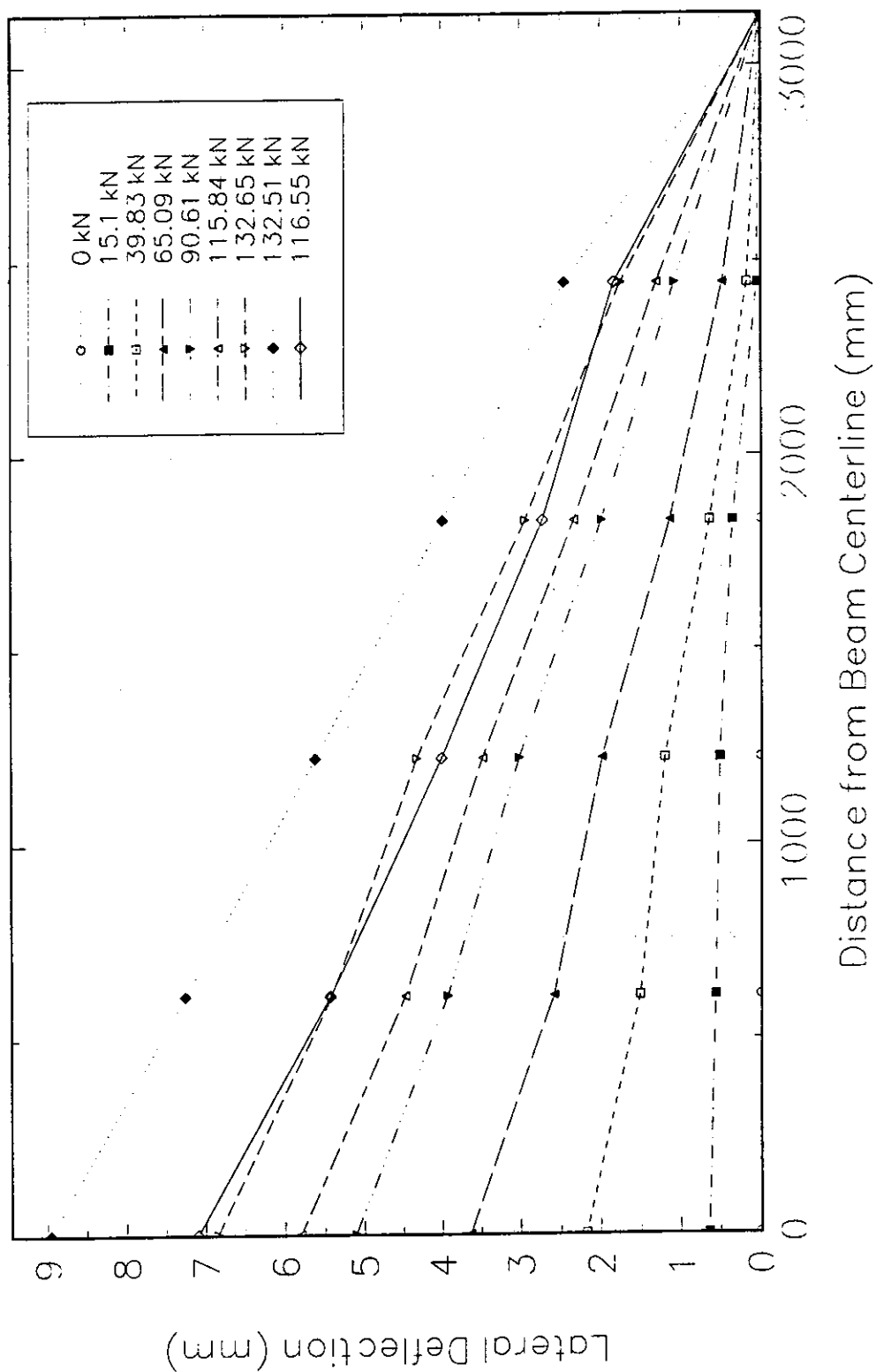
Figure 5.19
Bottom Flange Half Shape
Test 4
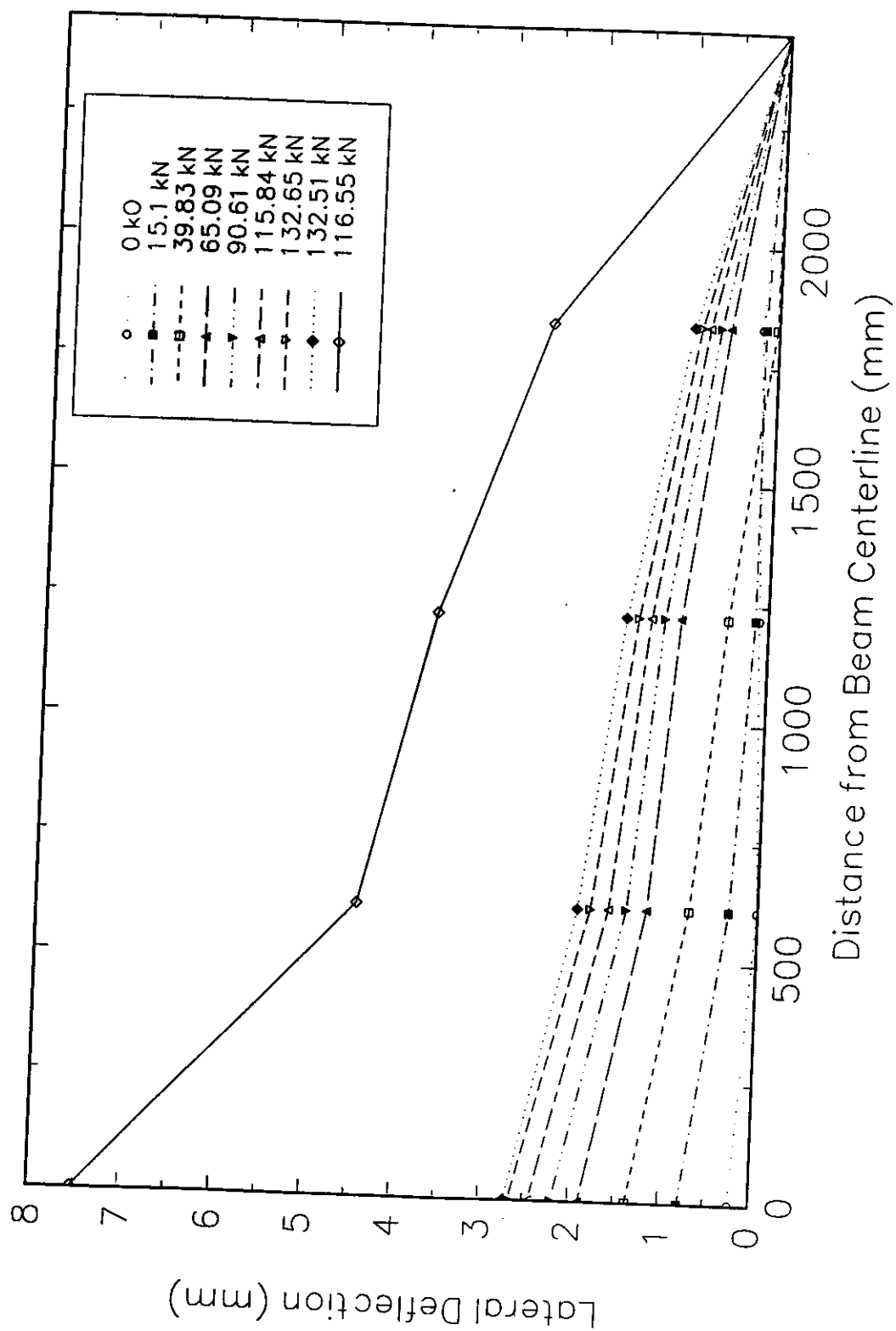
Figure 5.20
Bottom Flange Half Shape
Test 5

Legend:
- o — 0 kO
- ■ — 15.1 kN
- □ — 39.83 kN
- ▲ — 65.09 kN
- ▼ — 90.61 kN
- △ — 115.84 kN
- ▽ — 132.65 kN
- ◆ — 132.51 kN
- ◇ — 116.55 kN

X-axis: Distance from Beam Centerline (mm)

Y-axis: Lateral Deflection (mm)
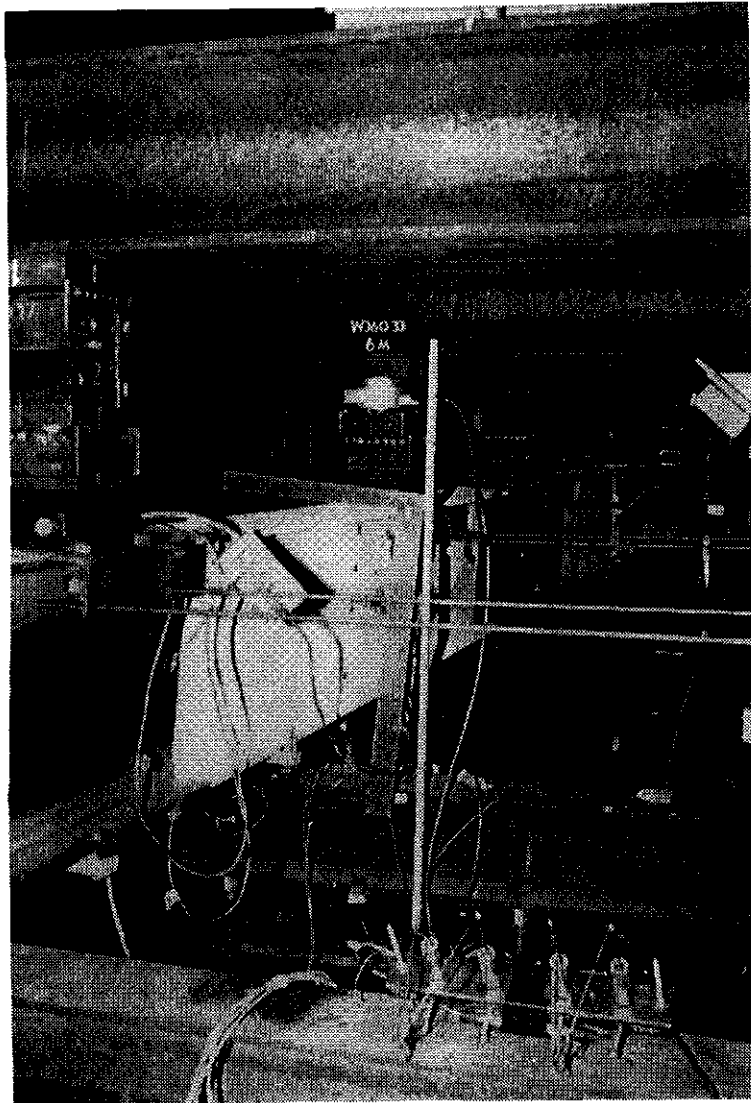
Figure 5.21
Test 1 at Maximum Lateral Tension Flange Deflection (31 mm)
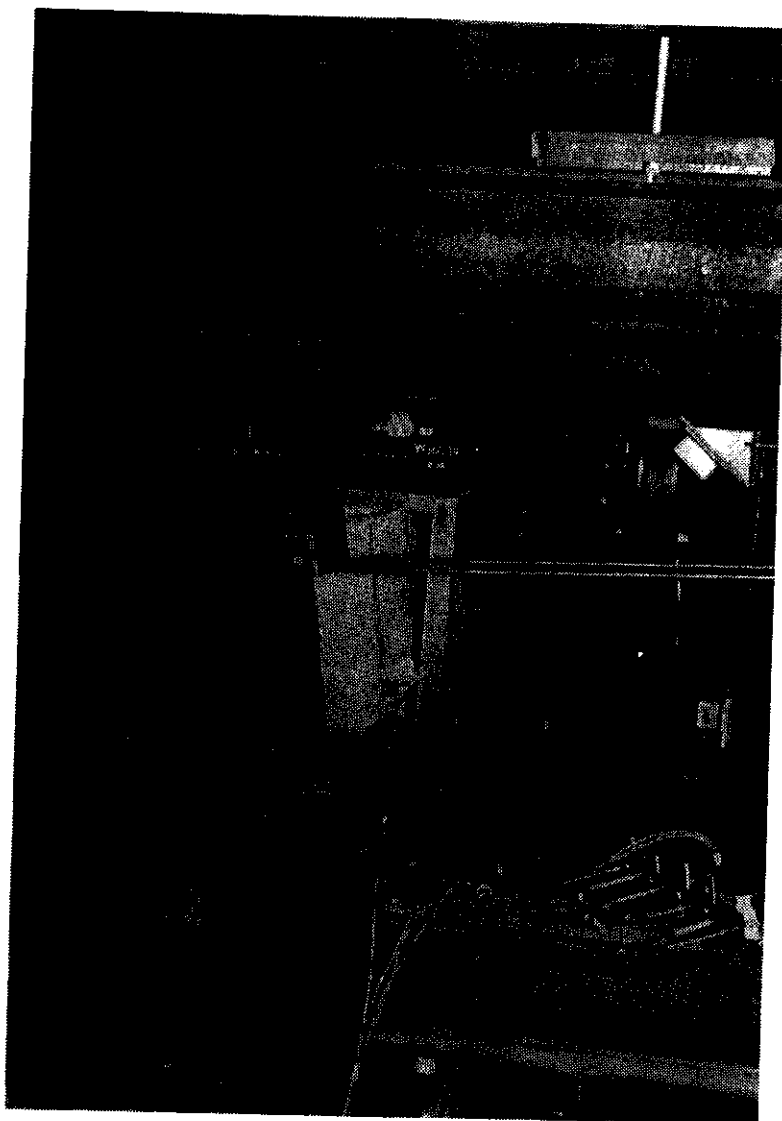
Figure 5.22
Test 4 at Maximum Load, P = 137 kN
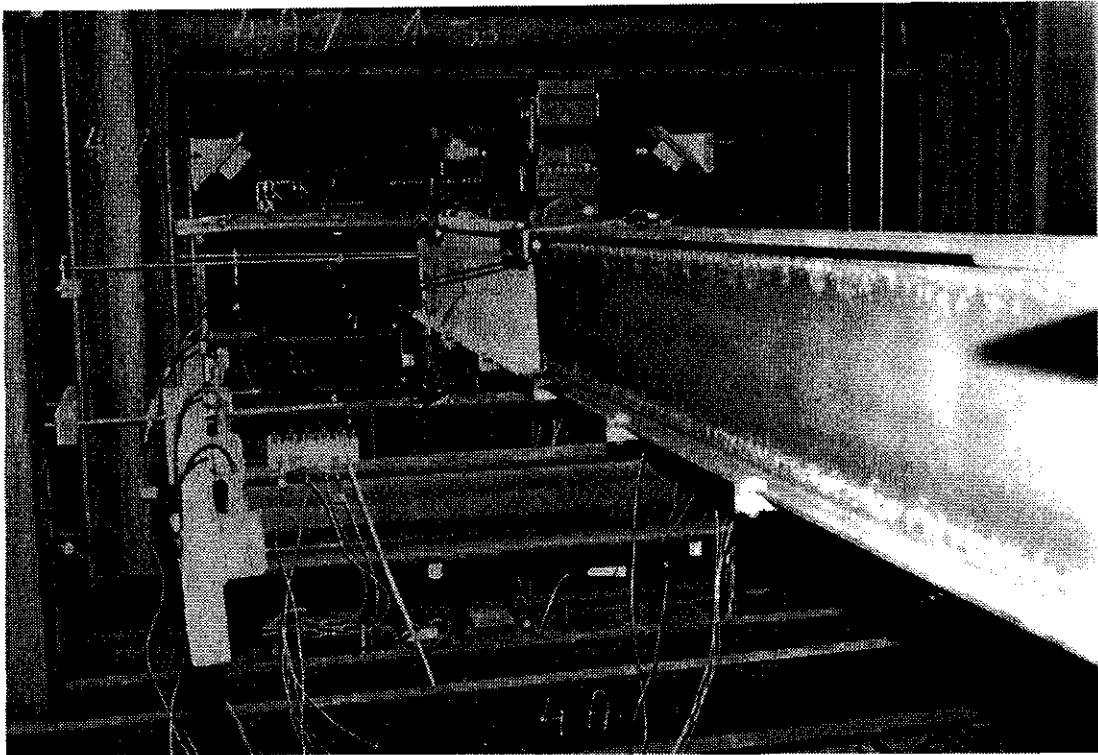
Figure 5.23
Test 4 at Load = 120 kN
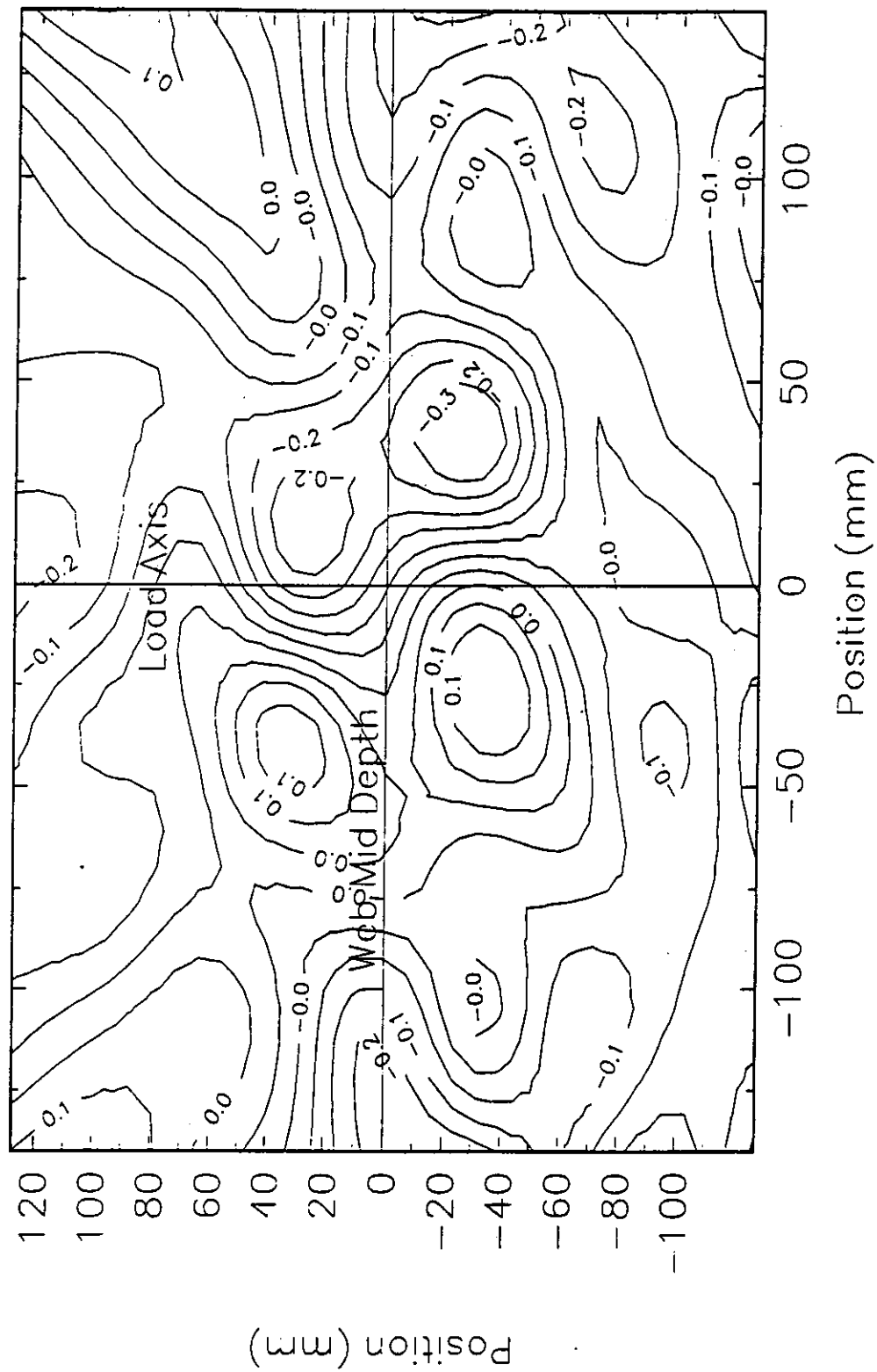
Figure 5.24
Web Deflection Contours (mm)
Test 1, Load = 109 kN
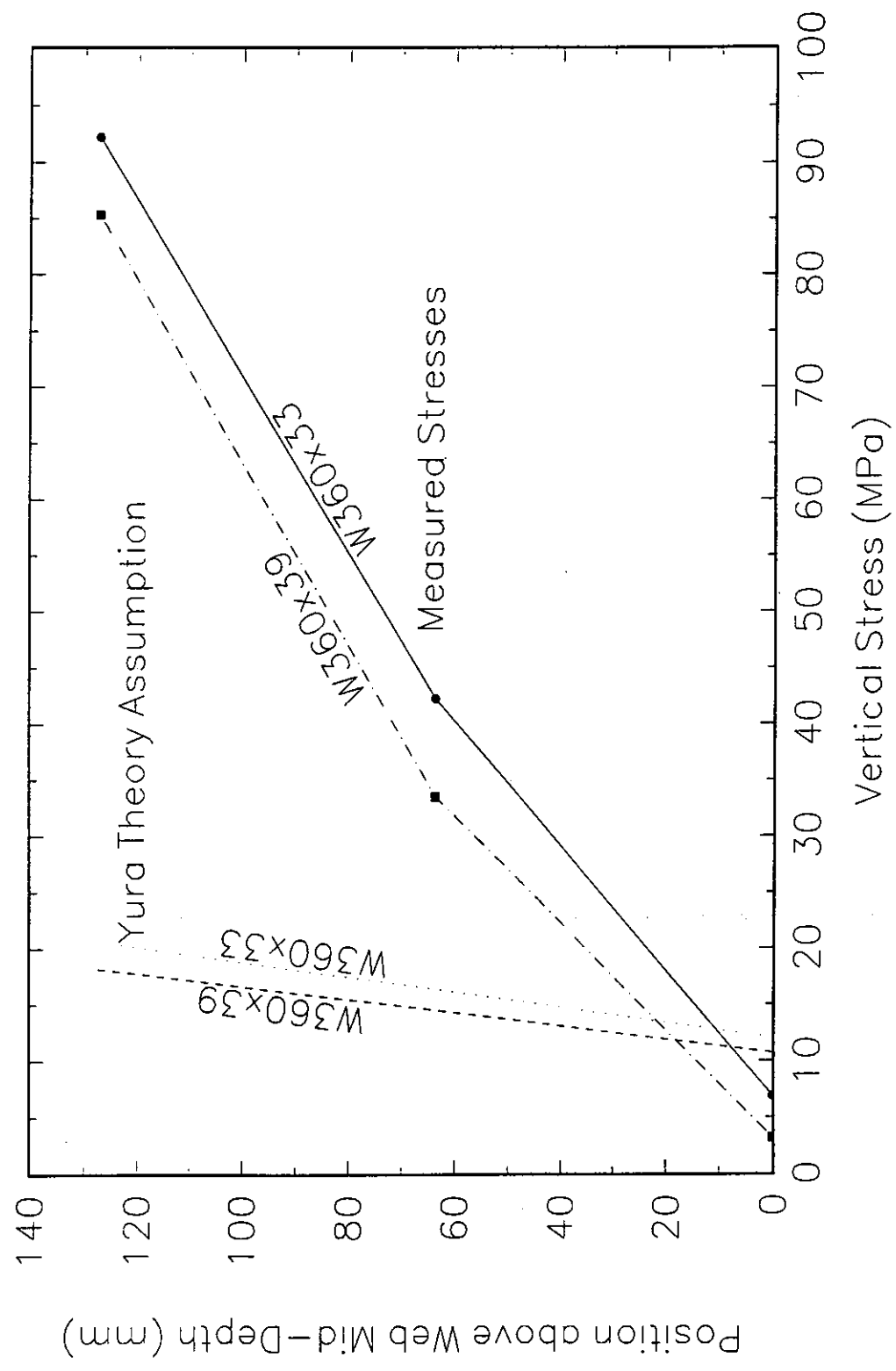
Figure 5.25
Vertical Stresses Below the Load Point
Load = 50 kN
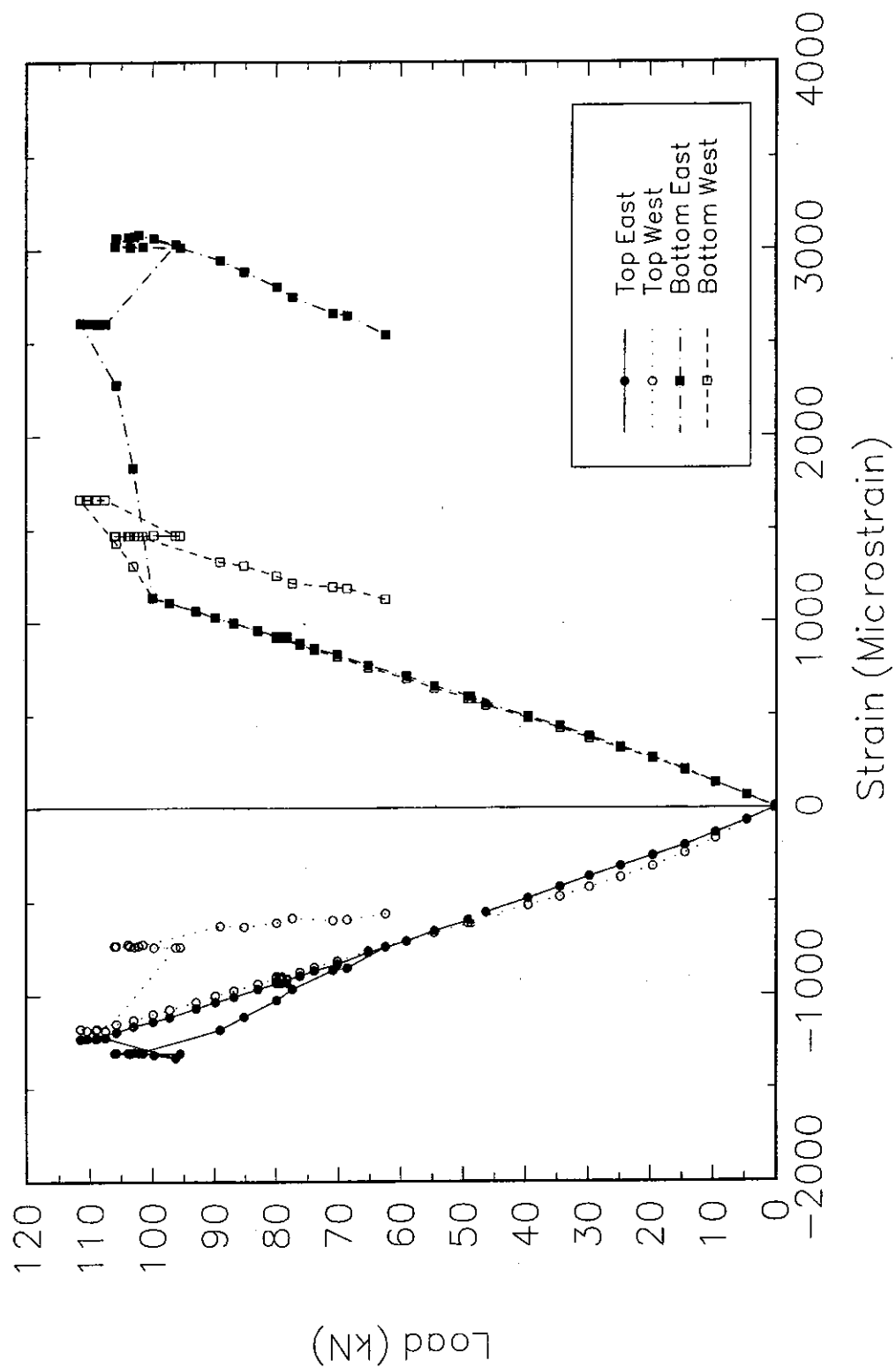
Figure 5.26
Load versus Flange Tip Strains
Test 1
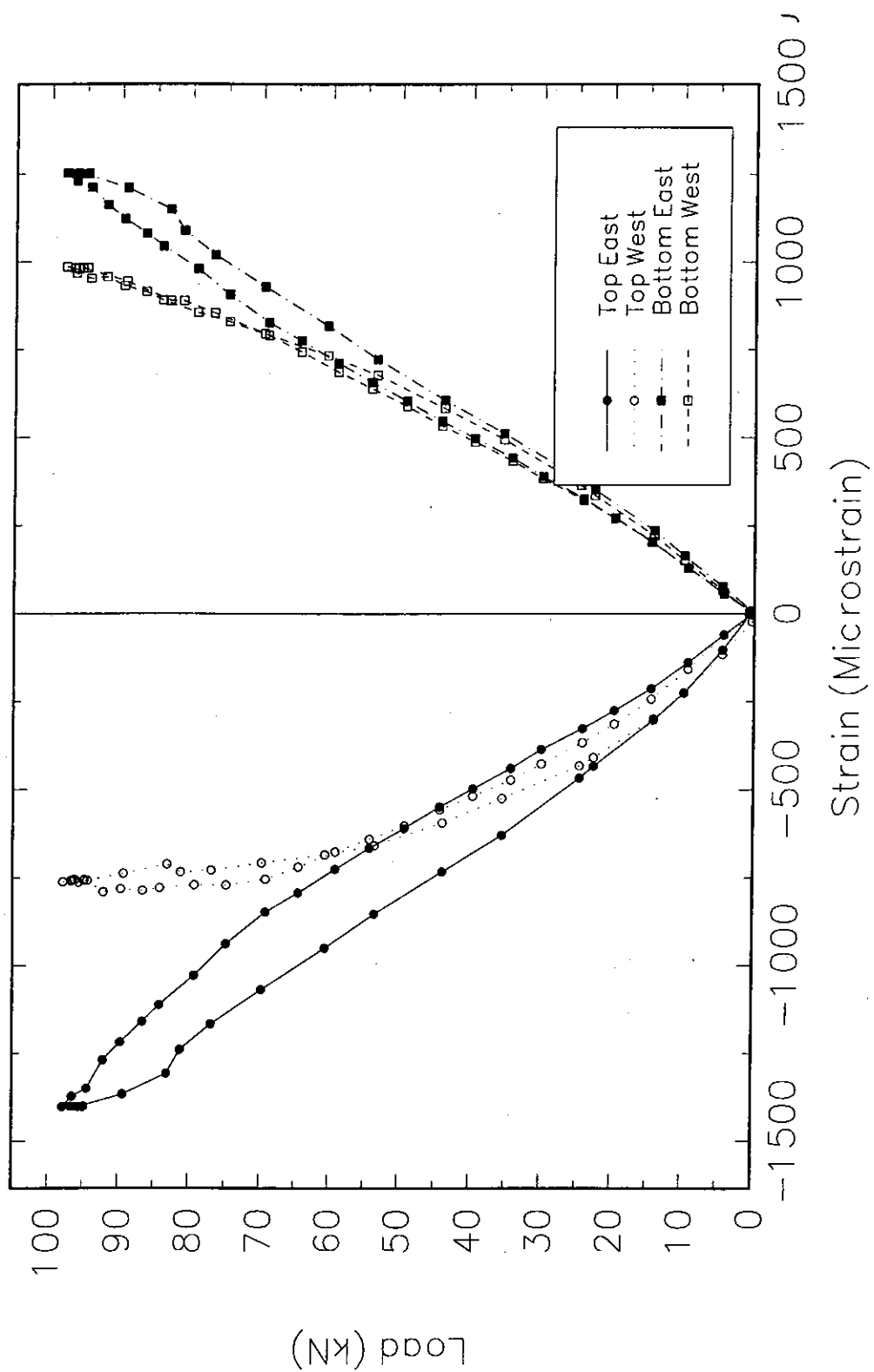
Figure 5.27
Load versus Flange Tip Strains
Test 2
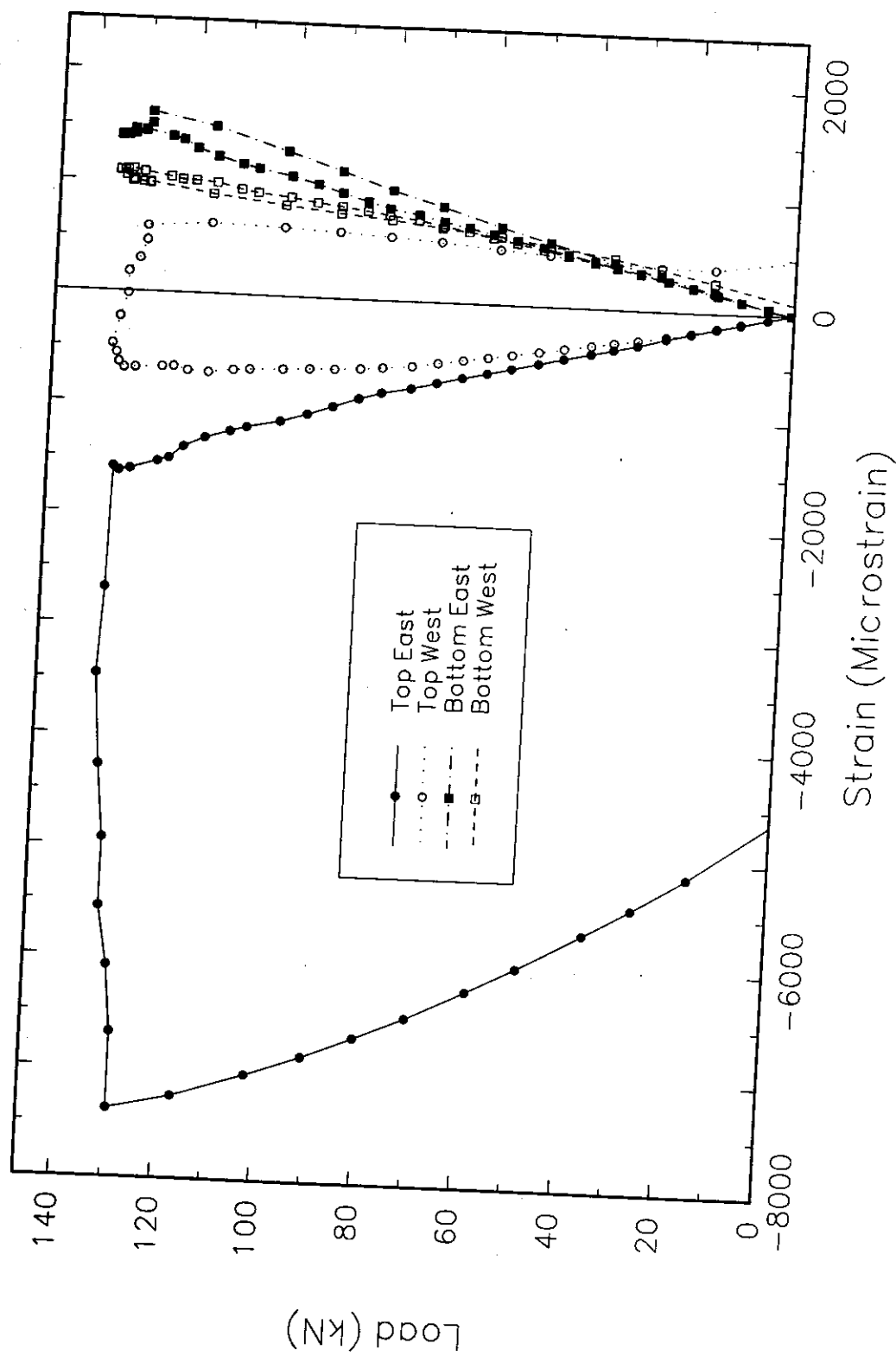
Figure 5.28
Load versus Flange Tip Strains
Test 3
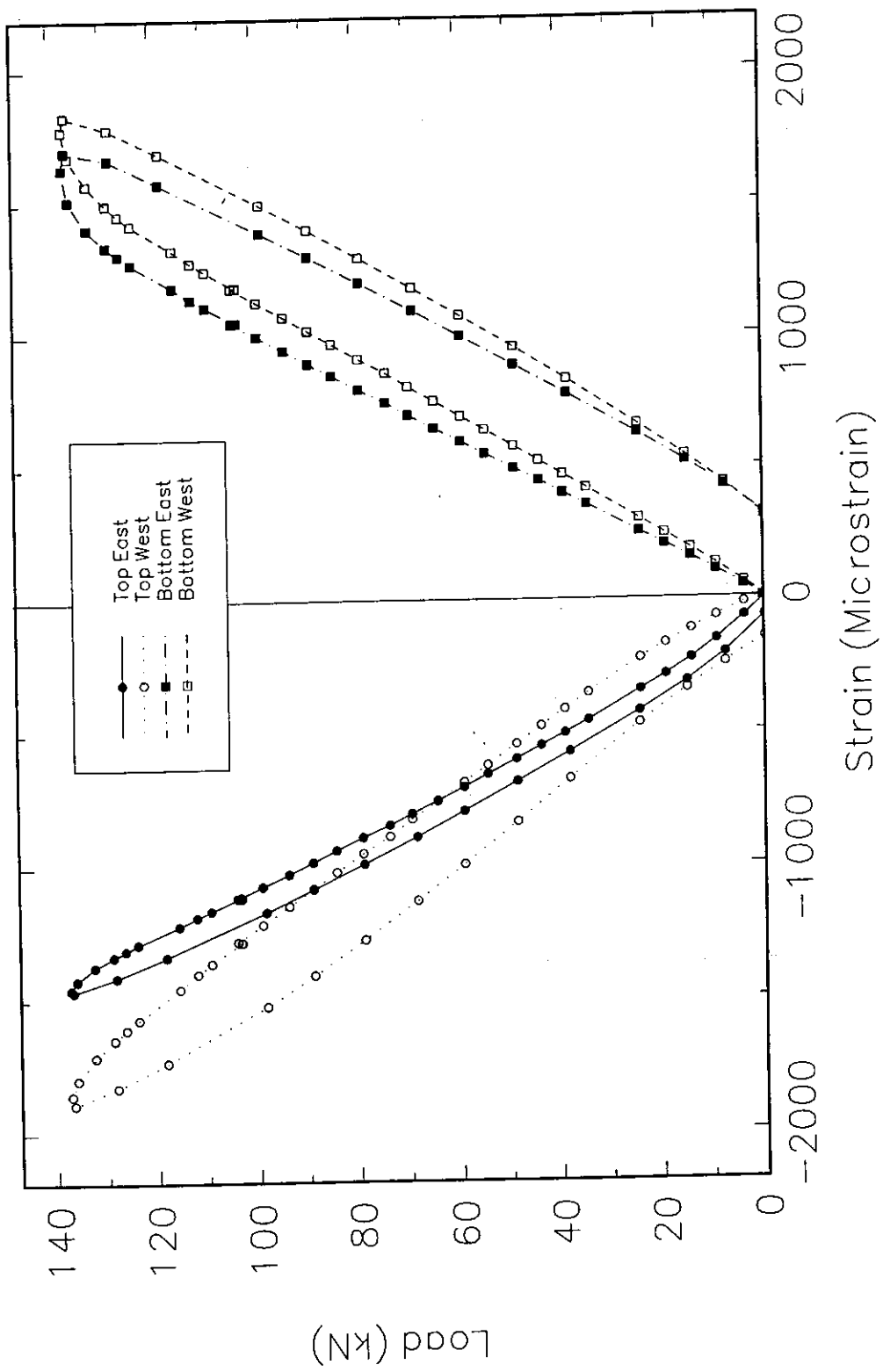
Figure 5.29
Load versus Flange Tip Strains
Test 4
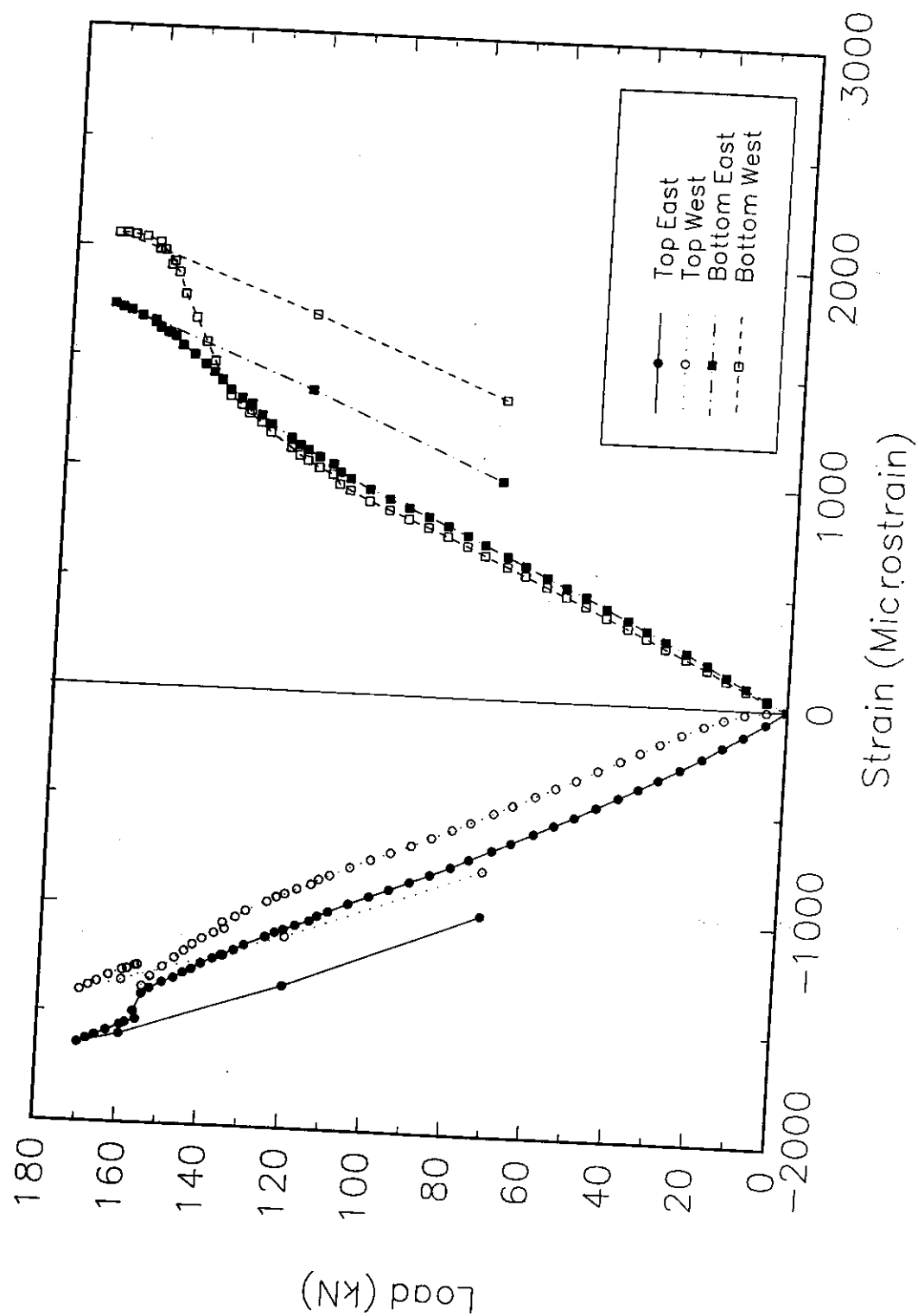
Figure 5.30
Load versus Flange Tip Strains
Test 5
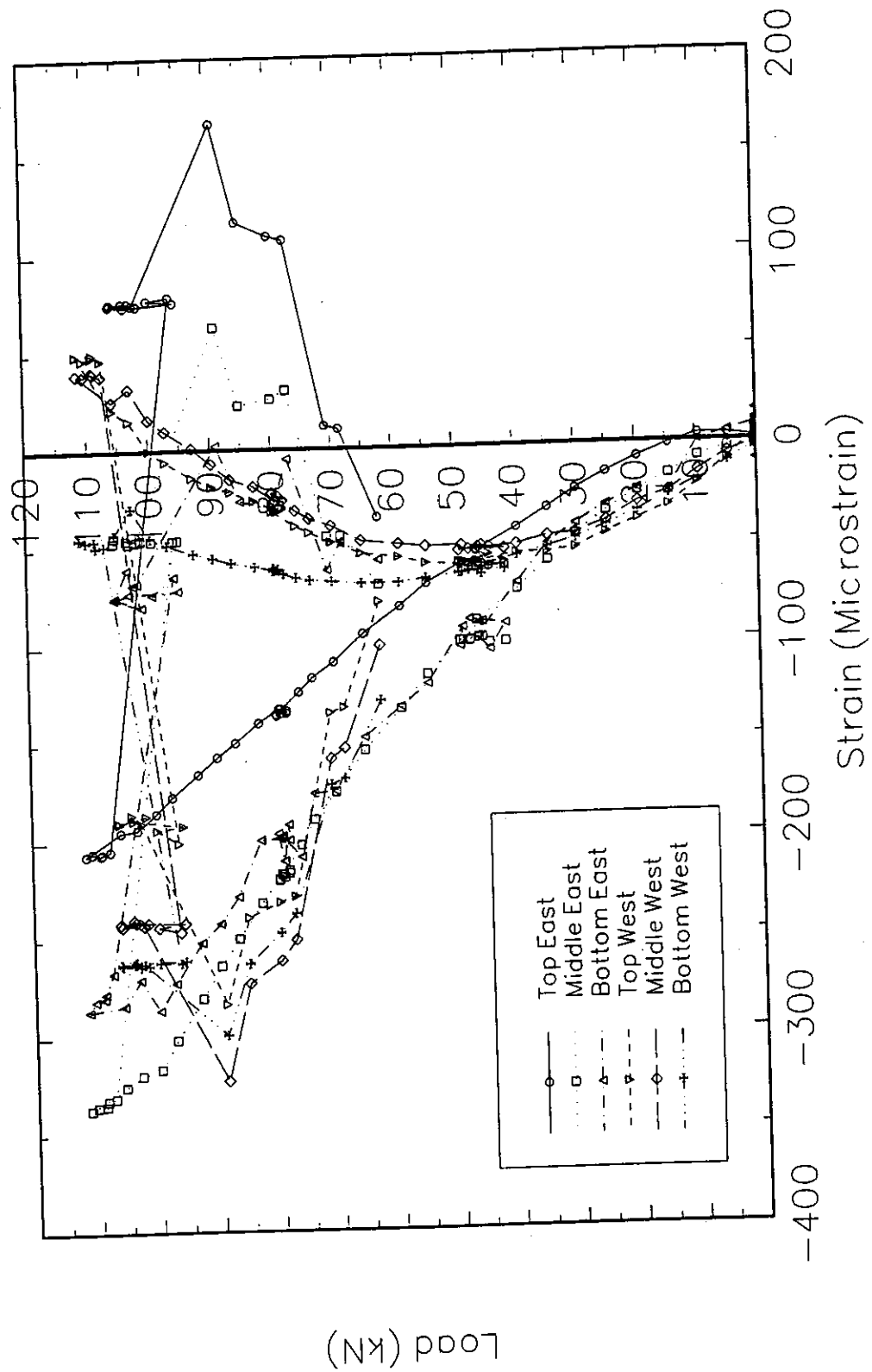
Figure 5.31
Vertical Web Strains
Test 1

6   DISCUSSION

6.1   Analysis

6.1.1   Finite Element Analysis

6.1.1.1   Finite Element Models

All styrene model beams were modelled using the same finite element mesh dimensions. Thicknesses and flange element widths were varied to reflect measured specimen dimensions. Styrene model specimen webs were modelled using a mesh of 3 x 22 plate elements. Accordingly, styrene model specimen flanges were 22 beam elements each and were connected to the top and bottom web plate edges. Figure 6.1 shows a typical finite element model, common to all finite element analyses for all tests.

Brace points, reaction and load points are indicated in Figure 6.1 and were defined as appropriate to reflect the boundary conditions of each test.

For the styrene model tests, lateral movement and twist about both the vertical and longitudinal axes were suppressed at the load and brace points. The brace point also provided the only resistance to longitudinal beam movement. Vertical reactions, at the ends of each beam, permitted deflection in the x-direction as shown in Figure 6.1. Figure 6.2 shows the calculated in-plane nodal stresses, in MPa, for the top flange of Beam A (other styrene beams were similar). In-plane nodal stress plots for the full scale tests indicated the presence of tension stresses at the ends of the beam flanges, corresponding to the inclusion of restraining end moments in the finite element analysis. Full

scale test finite element analysis restraining end moments were chosen to produce inflection point locations consistent with those presented in Table 5.1.

Since all beams were prismatic, any plot of stresses along a line parallel to the neutral axis is mathematically similar to the beam moment diagram. The stress plot represents the stresses arising from the load applied to the finite element model (1 N for model beams and 1 kN for full scale beams) and not the stresses present in the beam at the bifurcation load.

Figures 6.3 through 6.16 are the graphs of the eigenvector and corresponding eigenvalue calculated using the finite element model. Each line on the plot represents the buckled position of an element horizontal edge. The top flange, 2/3 web depth, 1/3 web depth and bottom flange deflected shapes are shown and labelled in the legend of each figure. The eigenvalue represents the value of the beam bifurcation load in Newtons for the styrene model tests and in kiloNewtons for the full scale beams. This is true since the eigenvalues shown in Figures 6.3 through 6.16 equal the coefficient by which the finite element load, a unit load in this case, must be multiplied to reach bifurcation.

6.1.1.2 Predicted Buckling Loads

Table 6.1 presents a comparison of finite element failure loads to measured peak loads for both the model and full scale test programs. The test/predicted ratios for the styrene model tests ranged from 0.7140 to 1.140 with a mean value of 0.8415. In most cases, styrene model test peak load did not reach the value predicted by the finite element model. This discrepancy could be attributed to two factors, initial imperfection in the specimens and the finite element modelling, as described in the following two paragraphs.

Finite element buckling analysis provides an estimate of the failure load of an initially perfect structure. While attempts were made to control and minimize initial imperfections in the styrene model test specimens, initial imperfections did exist. As part of his investigation, *Summers* (1982) intentionally introduced an initial mid-span lateral tension flange imperfection of L/800 (0.75 m). The failure load of the test beam was reduced to only 30% of that of a specimen with near zero initial tension flange imperfections (*Summers* (1982)). This example illustrates the potential effect of initial imperfections on buckling load.

The finite element mesh used in the analysis of styrene model tests was relatively coarse in the area of the observed web buckles. Figures 6.3 through 6.11 show the finite element predicted buckled shapes for styrene model tests A through I, respectively. In each case, the most severe web buckling (seen as a spike at the beam mid span in the 2/3 web depth deflected shape) occurs over only two elements. Since finite elements are assigned deflected shapes, they only approximate actual buckled shapes. With decreasing numbers of finite elements approximating an actual buckled shape, the variation between the actual and finite element approximation increases. Since actual buckled shapes are the lowest energy configuration a loaded structure can take, any other configuration will produce higher load. By using an inaccurate estimate of buckled shape, the finite element analysis load estimate will be higher than the actual failure load of the specimen.

Full scale finite element failure load predictions differed significantly from the full scale test peak loads as shown in Table 6.1. Test to finite element prediction ratios for the full scale tests ranged from 0.2482 to 0.3107 with a mean of 0.2830. The disagreement between the test peak loads and the finite

element predictions can be attributed to the effect of material yield. Full scale tests were either halted to avoid yield or were slightly inelastic. Finite element models assumed fully elastic behaviour and provided elastic buckling load estimates. In all cases, the finite element buckling load estimate was well in excess of the first yield load of the specimens.

6.1.1.3   Predicted Buckled Shapes

Although no tension flange movements were measured during the model tests, the predicted finite element buckled shapes for the model tests were very similar to observed test buckled shapes. All styrene model tests exhibited a characteristic upper web bulge directly below the load point. This bulge was also present in the finite element predicted buckled shapes shown in Figures 6.3 through 6.11 (Note: The buckled shapes are normalized on the largest predicted out-of-plane node deflection). Both the 2/3 and 1/3 web depth deflected shapes exhibit significant out-of-plane deflections at the mid span of each beam shown in Figures 6.3 through 6.11. Tension flange deflected shapes observed during the styrene model tests were also very similar to those shown in Figures 6.3 through 6.11.

While finite element buckling load estimates for the styrene model tests were greater than measured values, the two reasons cited for the inaccuracy, namely element mesh size and initial imperfections, would not normally result in significant discrepancy between finite element predicted buckled shape and structural behaviour.

Full scale test buckled shapes were measured accurately using apparatus described in chapter 4. The observed buckled shapes of the full scale test

specimens were very unlike the predicted finite element buckled shapes. In the finite element results, web bulges similar to those experienced in the model test series were predicted and are visible in the 2/3 and 1/2 web depth buckled shapes shown in Figures 6.12 through 6.16. Full scale test measured web bulging was less than 0.3 m in a square area, covering the full web depth directly below the load point.

The lack of agreement between the full scale test results and the finite element predicted buckled shape may be explained by the presence of fillets at the web-flange juncture and the lower load levels reached during the full scale tests.

Fillets reduce the depth to thickness ratio of the web and reduce the vertical stresses in the webs of point loaded beams. Both factors stabilize the web. Finite element models did not include fillets and therefore the finite element model web was less stable and was subjected to larger vertical stress than the real structure. These differences would make the finite element web more susceptible to web buckling than the full scale test specimen web.

Full scale tests were halted at load levels well below finite element predicted buckling load. It is likely that vertical web stresses below the load point for the full scale tests were also well below those predicted for the finite element model web at failure. The vertical web stresses in the full scale tests may have been insufficient to cause web buckling as predicted by the finite element model.

Full scale test lateral tension flange deflections ranged between 7.6 m at the maximum load for test 5, and 48.3 m at the maximum load of test 3. The

lateral deflected half-shapes of the bottom flanges at several load levels are shown in Figures 5.16 through 5.20 (refer to section 5.3.1 for explanation of Figures 5.16 though 5.20). The deflected half-shape of the bottom flanges of tests 1, 2 and 3 (Figures 5.16, 5.17 and 5.18) appeared very similar to the predicted deflected shapes predicted by the finite element analysis (Figures 6.12 through 6.16, bottom flange deflected shapes only) with both being sinusoid. The measured bottom flange half-shapes of tests 4 and 5 (Figures 5.19 and 5.20) were not similar to finite element outputs. This is attributed to rigid body motion of the beam supporting the cable transducers shown in Figure 4.18. The measured deflected half-shapes shown in Figures 5.19 and 5.20 do not agree with qualitative observations of tests 4 and 5 as no abrupt curvature changes were observed in the deflected bottom flanges of tests 4 or 5.

6.2   Revision of Proposed Model

The following section describes a modification made to the interaction equation [3.4] to address the presence of inelasticity in full scale tests.

The result of the proposed model developed in chapter 3 is the interaction equation [3.4] shown below:

$$[3.4]\ 1 \geq (\frac{\sigma_v^T}{2\sigma_{cr_v}})^2 + (\frac{\sigma_h^T}{\sigma_{cr_H}})^2$$

The critical buckling stresses for the assumed edge conditions and stress distributions were defined as:

$$[3.3]\ \sigma_{cr} = K\frac{\pi^2 E}{12(1-\nu^2)(c/t_w)^2}$$

The expression for critical stress, equation [3.3], is not limited by material properties and assumes elastic response for all stresses. If an elastic-plastic stress-strain response is assumed, ductile structural elements are limited by material strength and may not sustain stresses beyond yield stress. The critical stress is therefore limited to values less than or equal to yield stress. To account for inelasticity in full scale tests, the expression for critical stress in the interaction equation was changed to equation [6.1] (below) which limits critical stresses to the yield stress of the material.

$$[6.1] \quad \sigma_{cr} = K \frac{\pi^2 E}{12(1-\nu^2)(c/t_w)^2} \leq \sigma_Y$$

Where σ_Y = Yield Stress

Note: The inclusion of the yield stress limit on critical stress does not effect the predictions for styrene model tests since critical stresses were all in the elastic range.

6.3 Comparison of Test Loads to Design Strengths

Table 6.1 presents the test peak loads, *Costley* and *Summers* test results, AISC-LRFD and the test to predicted ratios for the AISC-LFRD design equation. Table 6.2 presents the S16.1 web crippling and web yielding design limits, test peak loads and test to predicted ratios for each.

The AISC-LRFD equation design loads, as they appear in Table 6.1, are unfactored and are generally conservative for the model tests. Styrene model test to predicted ratios range between 0.932 and 2.122. These values are acceptably conservative for structural design but are very scattered. For this

reason, the AISC-LRFD is not a good predictor of peak load for model tests. Full scale test peak loads were well above the unfactored design value from the AISC-LRFD equation. Test to predicted ratios range between 1.395 and 4.743. For full scale tests, the AISC-LRFD design equation provided inaccurate predictions of failure load and was overly conservative.

The AISC-LRFD design equation was based a column model of the web. Both the vertical stress distribution and the restraint provided by the tension flange are conservative assumptions. Vertical web stress distribution is assumed triangular through the web depth and all rotational restraint provided by the flanges is ignored. Both assumptions result in conservative failure load estimates.

To provide comparison with the existing CAN/CSA-S16.1 design Standard (Canadian Standards Association (1989)), the web crippling and web yielding design equations, from the standard, were used to calculate the unfactored full scale test failure loads. The predicted failure loads were well in excess of the peak test loads as presented in Table 6.2. Each beam in the full scale test series was a designed according to the S16.1 Standard, to reach plastic moment capacity, but none reached their unfactored design load. Also, by the S16.1 Standard, no stiffeners were required below the load point to sustain the full capacity of any of the five full scale tests.

Both the web crippling and web yielding design equations of the S16.1 Standard were based on test results of short span beams. These tests did not permit significant lateral displacement of twist of the tension flange. As a result, the tension flange movement failure mode is neither implicitly or explicitly addressed in the S16.1 Standard.

6.4   Comparison of Predictive Models

The predictions of the revised interaction equation are compared to the full scale, styrene model test, *Costley* and *Summers* test results in Table 6.1.

The discussion of the accuracy of the revised interaction equation is divided into two separate discussions. One discussion addresses the accuracy of the revised predictive model at predicting both the styrene model test failure loads and the *Summers* test failure load. The other discussion addresses the accuracy of the revised interaction equation at predicting failure loads for the full scale tests from this study and the *Costley* test.

The failure load predictions of the revised interaction equation were generally unconservative for the styrene and *Summers* model tests. Test to predicted ratios for the tests ranged from 0.612 to 1.055 with an average value of 0.802. The development of the interaction equation was based on assuming that an area of web of fixed dimensions relative to web depth was involved in buckling. This assumption led to the selection of the web area shown in Figure 3.3. In reality, the size of the web buckle is affected by the relative stiffness of the web and the restraining bottom flange. If the restraining flanges are infinitely stiff with respect to the web stiffness, the web will buckle such that rotations and out-of-plane deflections of the web at the web-flange juncture are zero. If the restraining bottom flange has zero stiffness (i.e. a Tee section) the bottom of the web is free to deflect and rotate without development of restraining forces. These extremes are analogous to a fixed-fixed column

(effective length = 0.5 L) and a cantilever column (effective length = 2 L). Real beams are between these two extremes.

Just as the effective length of a column changes with varying end restraint, the effective depth of the web can also vary with changing restraining flange stiffness. By decreasing flange lateral restraining stiffness, the effective web depth and the magnitude of lateral tension flange deflections (relative to web deflections) can be increased. As model tests proceeded from A through I, flange width decreased thereby creating a decreasing bottom flange lateral restraining stiffness trend through the tests. While the trend was somewhat disrupted by the effects of varying flange thickness, it can be observed as an overall effect through the entire test series.

While lateral flange deflections were not measured during the styrene model tests, reference can be made to the finite element analysis results. Normalized finite element predicted buckled shapes for styrene model tests A though I (Figures 6.3 through 6.11) exhibit a trend toward increasing normalized lateral tension flange deflection with decreasing flange width. This results in a larger effective web depth and, therefore, a reduction in the buckling load of the system.

With reduction of flange width and lateral restraining stiffness during the styrene model tests, a reduction in buckling load of the structural system was noted. This has been attributed to the increase in effective depth of the web. The interaction equation does not address the link between restraining flange stiffness and effective web depth but assumes that effective web depth is constant. With decreasing lateral restraining stiffness, the accuracy of the

predictions of the interaction equation were reduced. Test to predicted ratios decrease as restraining flange stiffness decreases.

The predication accuracy of the revised interaction equation was good for the full scale tests with test to predicted ratios ranging from 0.760 to 1.198 with an average of 1.014. All full scale test were either partially inelastic or were halted near calculated first yield stress. The addition of the yield stress limit on critical stress is the reason for this good correlation.

TABLE 6.1 Comparison of Measured to Predicted Loads

Beam	Test Peak Load (kN)	Finite Element Model		AISC-LRFD		Interaction	
		Load	Test Pred	Load	Test Pred	Load	Test Pred
Model A	0.4661	0.4088	1.140	03216	1.449	0.4419	1.055
Model B	0.3635	0.3997	0.909	0.3216	1.130	0.4127	0.881
Model C	0.2952	0.3170	0.931	0.3167	0.932	0.3800	0.777
Model D	0.3826	0.3916	0.977	0.2733	1.400	0.4190	0.913
Model E	0.2610	0.3655	0.714	0.2307	1.131	0.3847	0.678
Model F	0.2299	0.3099	0.742	0.1872	1.228	0.3375	0.681
Model G	0.2641	0.3682	0.717	0.1470	1.797	0.3819	0.612
Model H	0.2486	0.3476	0.715	0.1286	1.933	0.3440	0.723
Model I	0.2330	0.3204	0.727	0.1098	2.122	0.2948	0.790
Summers	0.1159	0.1315	0.881	.0193	6.005	0.1280	0.906
Test 1	111.46	358.6	0.311	36.6	3.045	104.1	1.071
Test 2	97.90	357.0	0.274	70.2	1.395	128.8	0.760
Test 3	135.17	492.1	0.275	28.5	4.743	112.8	1.198
Test 4	137.26	553.0	0.248	48.6	2.824	134.6	1.020
Test 5	170.00	557.0	0.305	93.2	1.824	166.8	1.019
Costley	122.6	379.4	0.323	127.2	0.964	120.9	1.014

Table 6.2 Comparison of Full Scale Test Loads to Design Loads

Test	Test Peak (kN)	S16.1 Web Crippling (kN)	Test/Pred	S16.1 Web Yielding (kN)	Test/Pred
Test 1	111.46	361.7	0.316	553.4	0.201
Test 2	97.90	361.7	0.271	553.4	0.177
Test 3	135.17	457.1	0.296	663.2	0.204
Test 4	137.26	457.1	0.300	663.2	0.207
Test 5	170.00	457.1	0.372	663.2	0.256
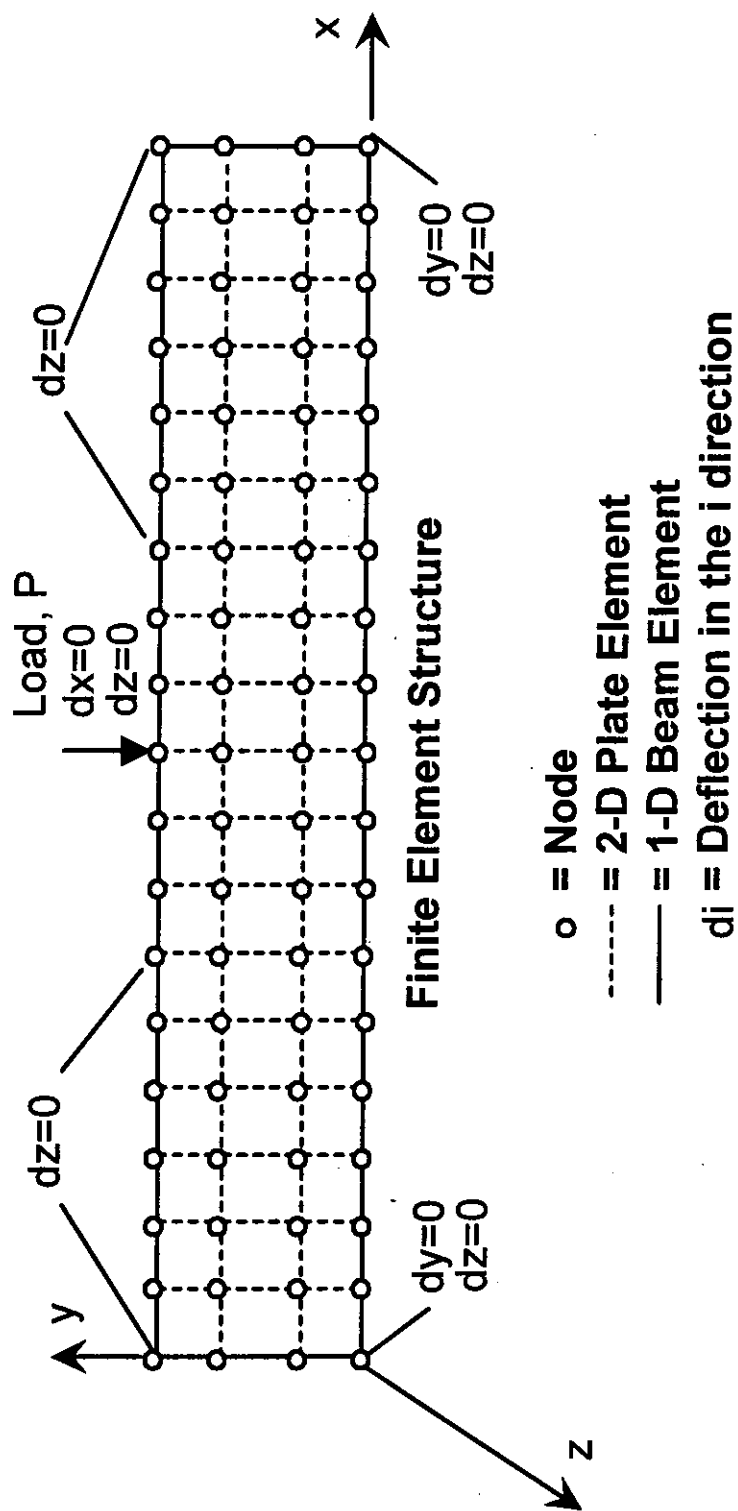
Figure 6.1
Finite Element Mesh

Test A Maximum Stress = 0.033 MPa @ 1 N
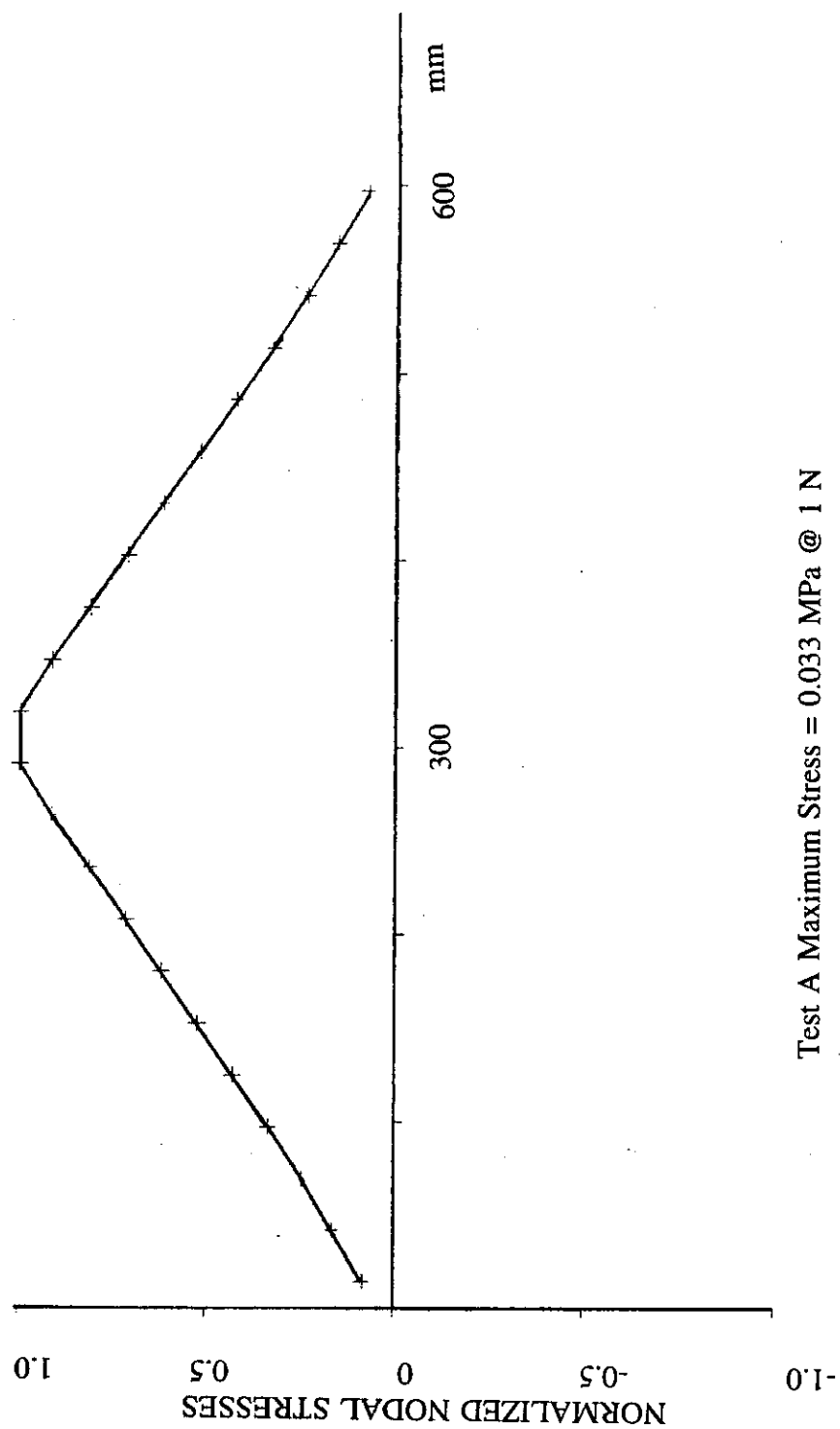
Figure 6.2
Finite Element In-Plane Stress Output
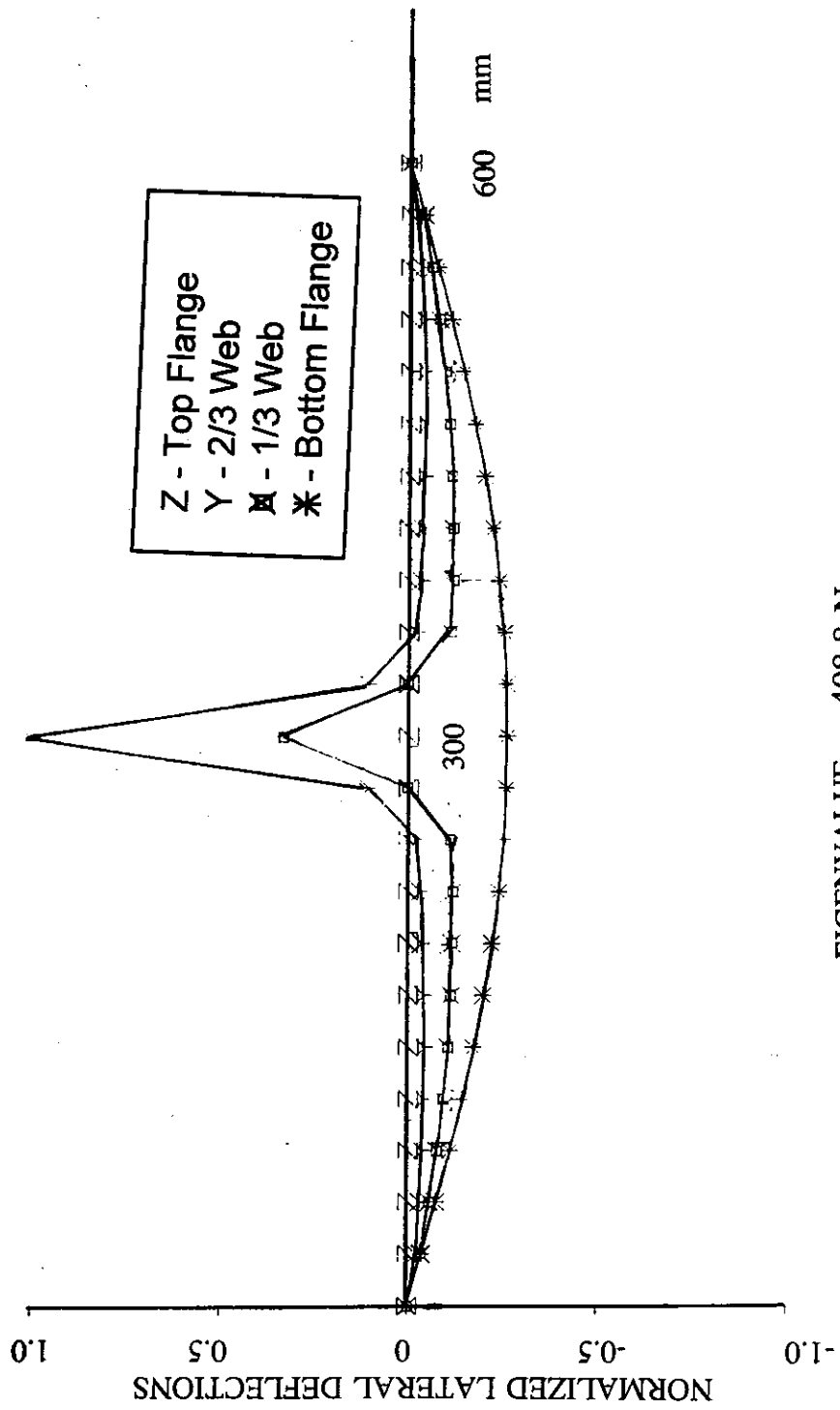
NORMALIZED LATERAL DEFLECTIONS
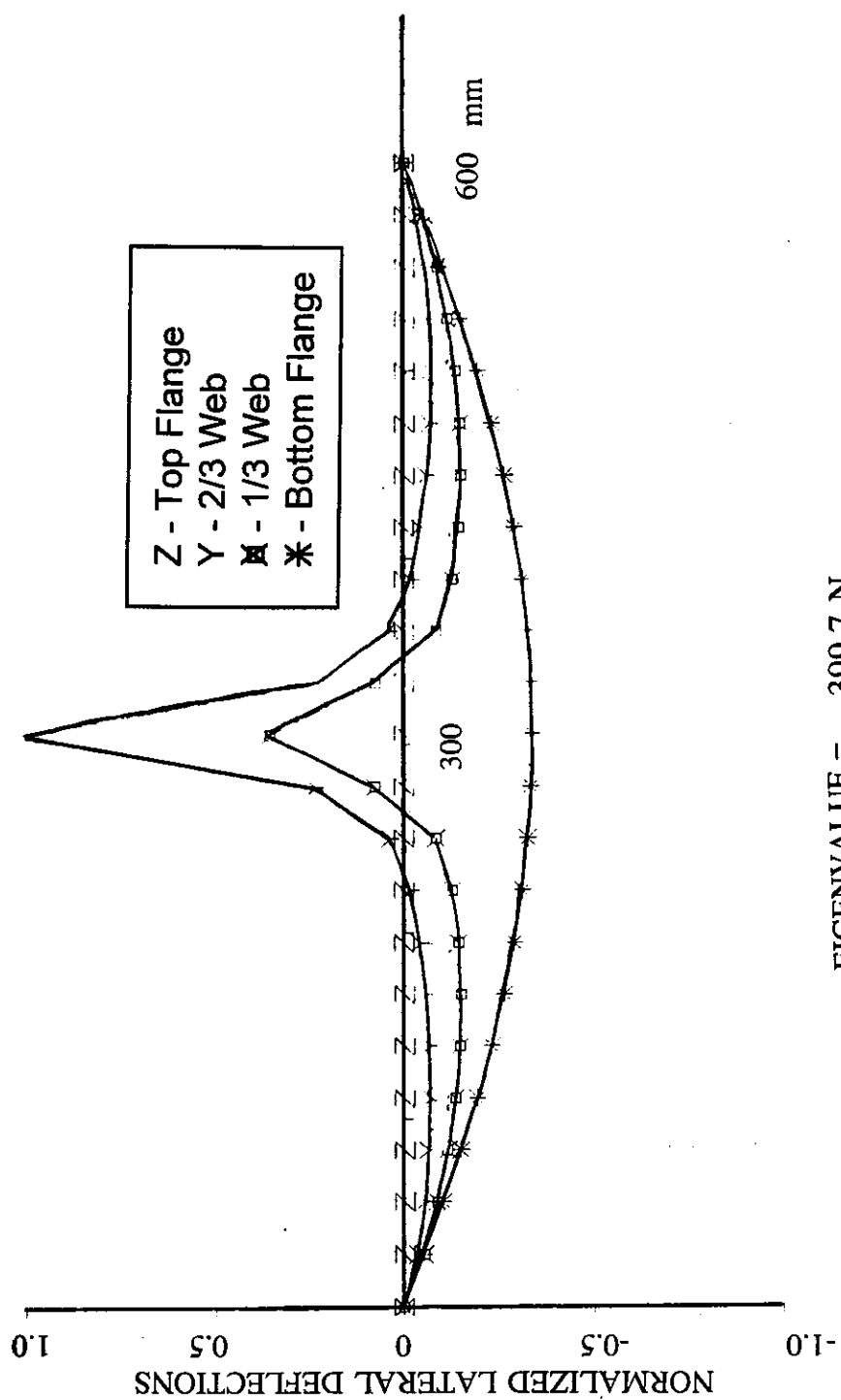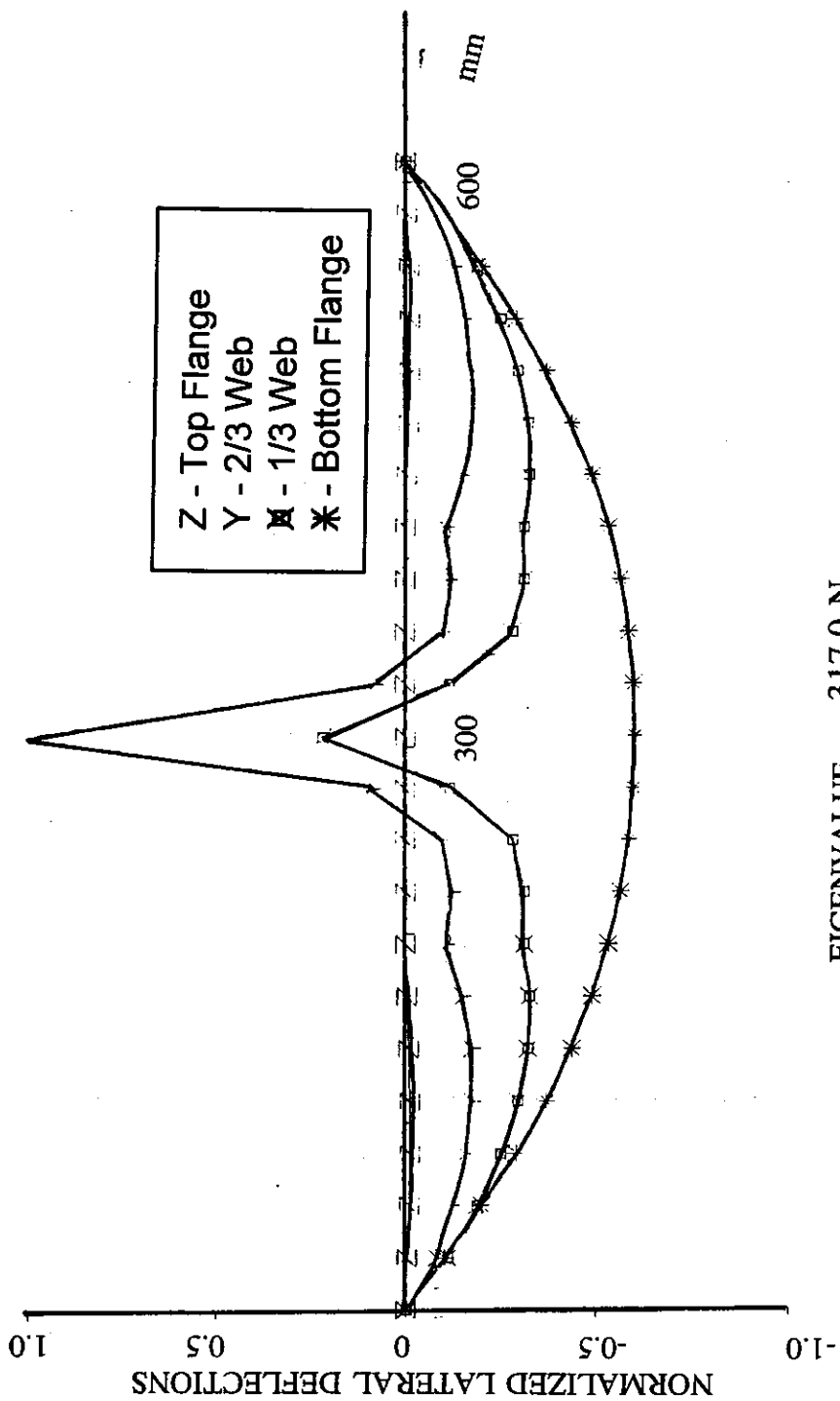
EIGENVALUE = 408.8 N
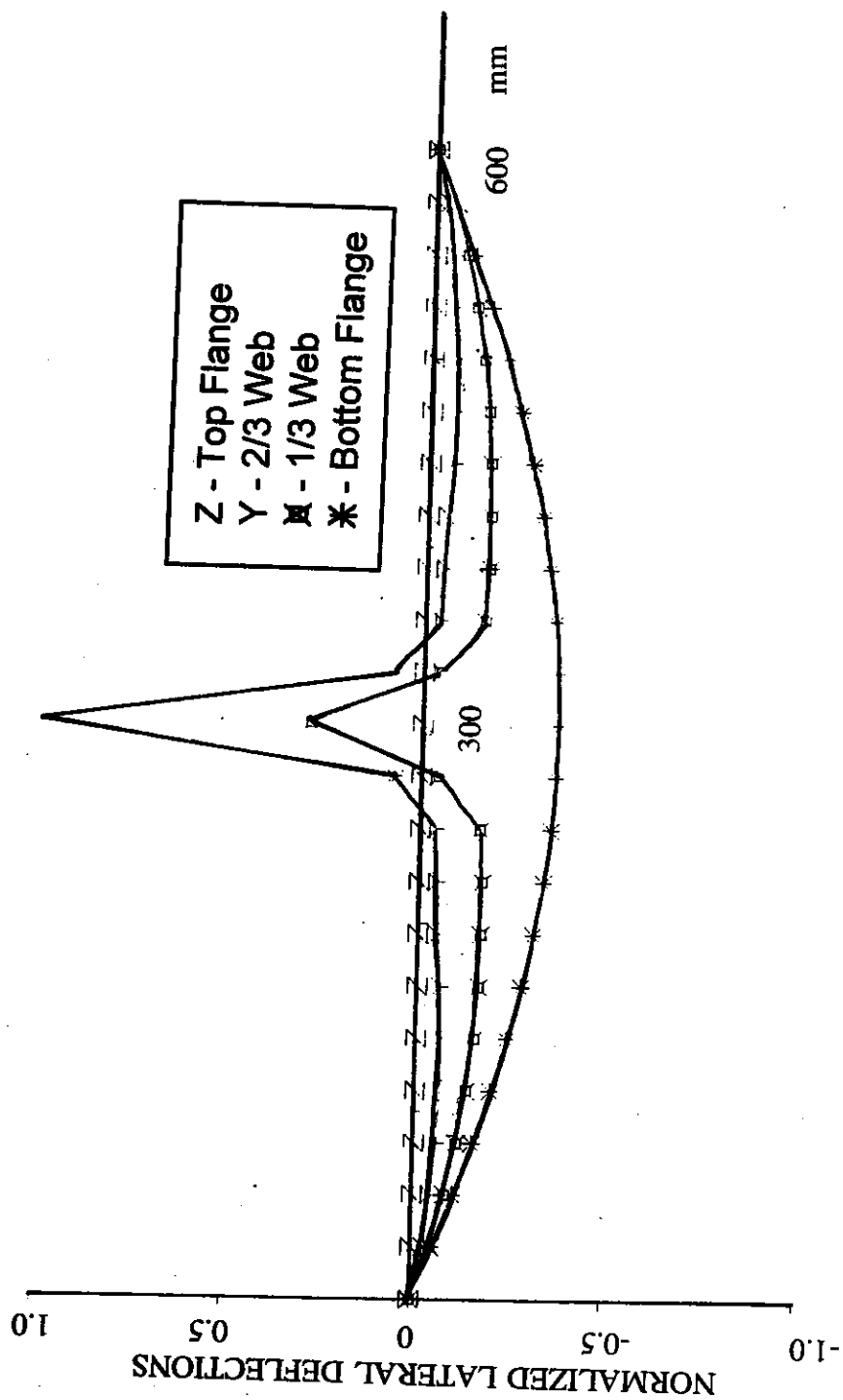
Figure 6.3
Test A FEM Buckled Shape

EIGENVALUE = 399.7 N

Figure 6.4
Test B FEM Buckled Shape

EIGENVALUE = 317.0 N

Figure 6.5
Test C FEM Buckled Shape

EIGENVALUE = 391.6 N

Figure 6.6
Test D FEM Buckled Shape
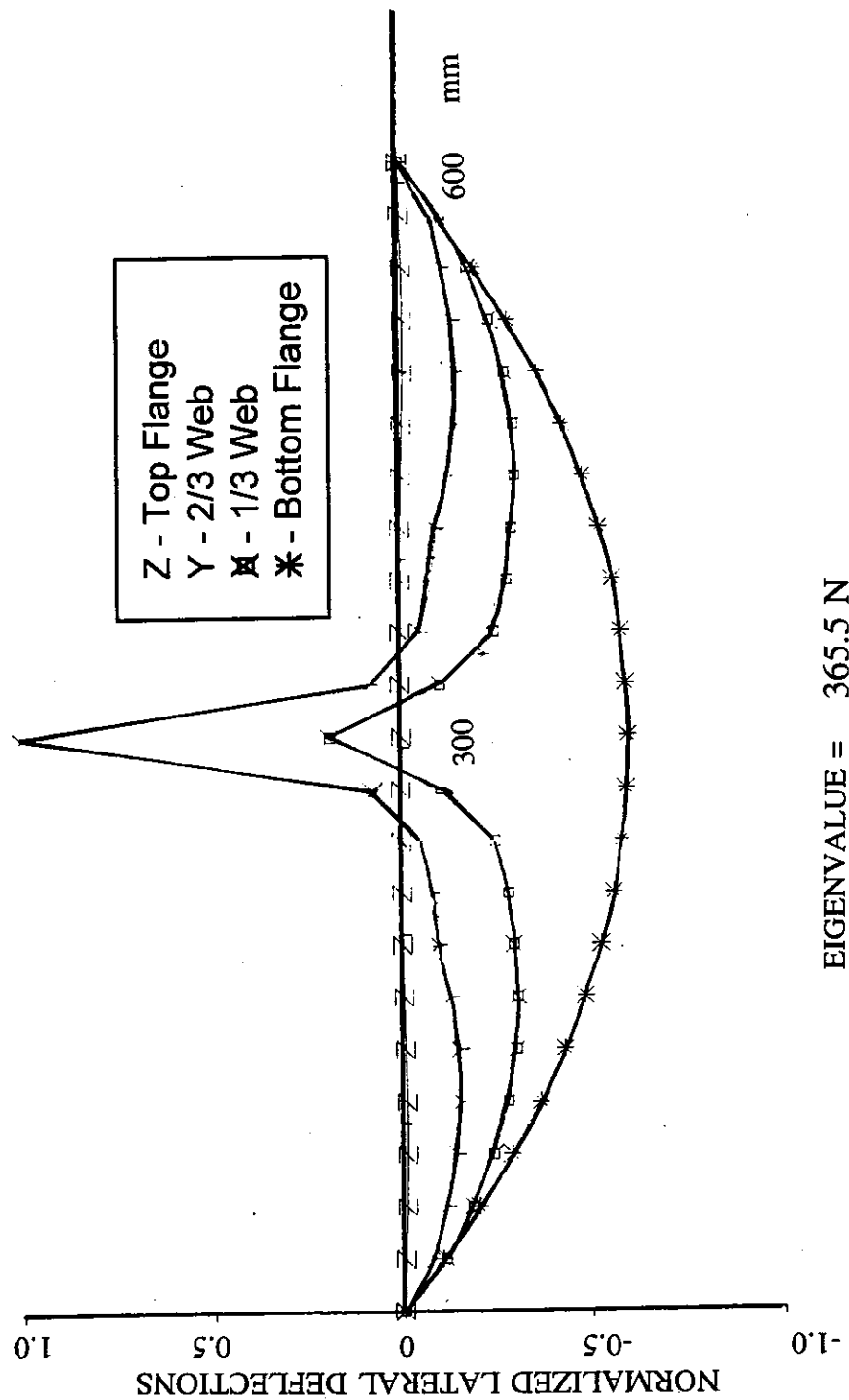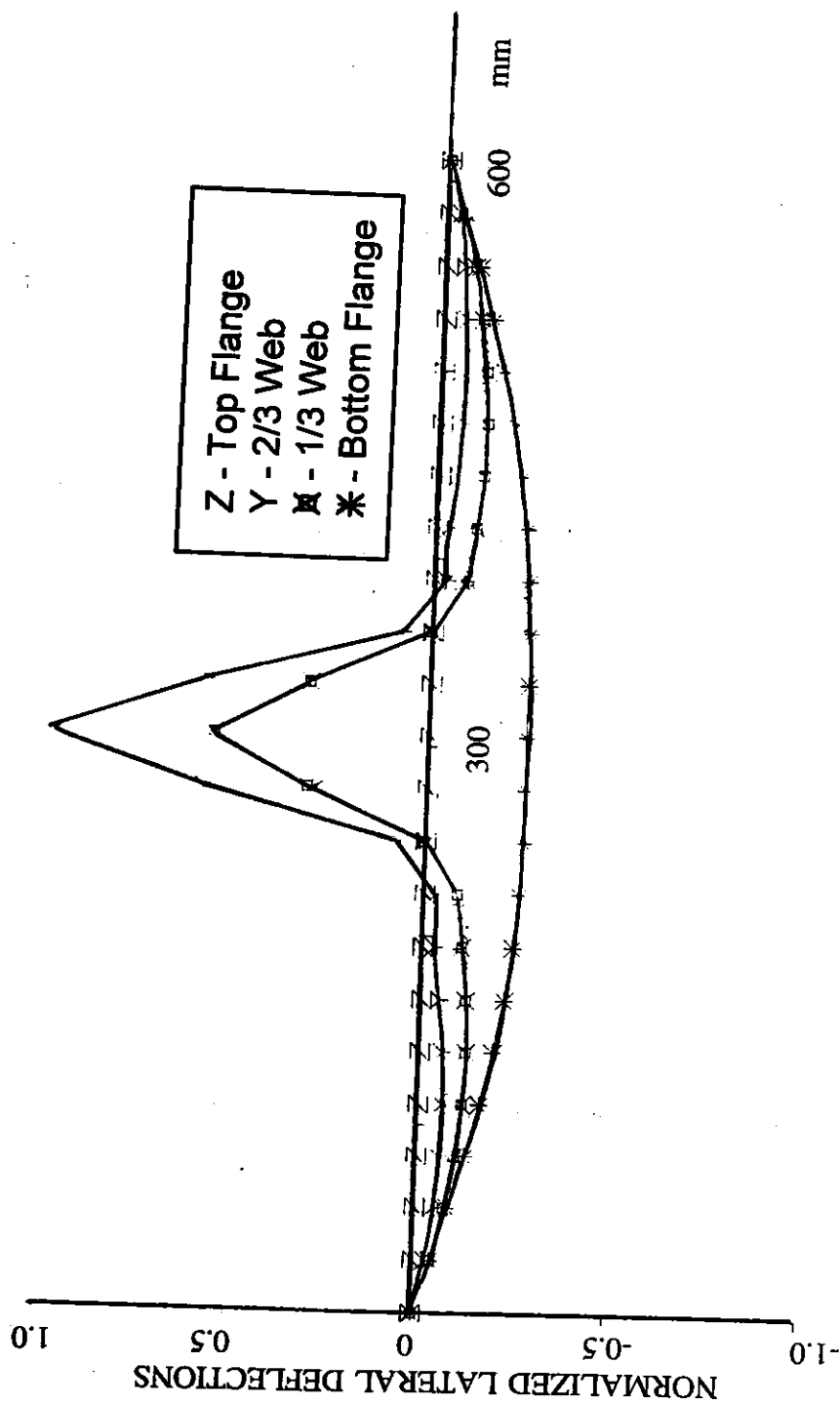
EIGENVALUE = 365.5 N

Figure 6.7
Test E FEM Buckled Shape

EIGENVALUE = 309.9 N

Figure 6.8
Test F FEM Buckled Shape

EIGENVALUE = 368.2 N

Figure 6.9
Test G FEM Buckled Shape
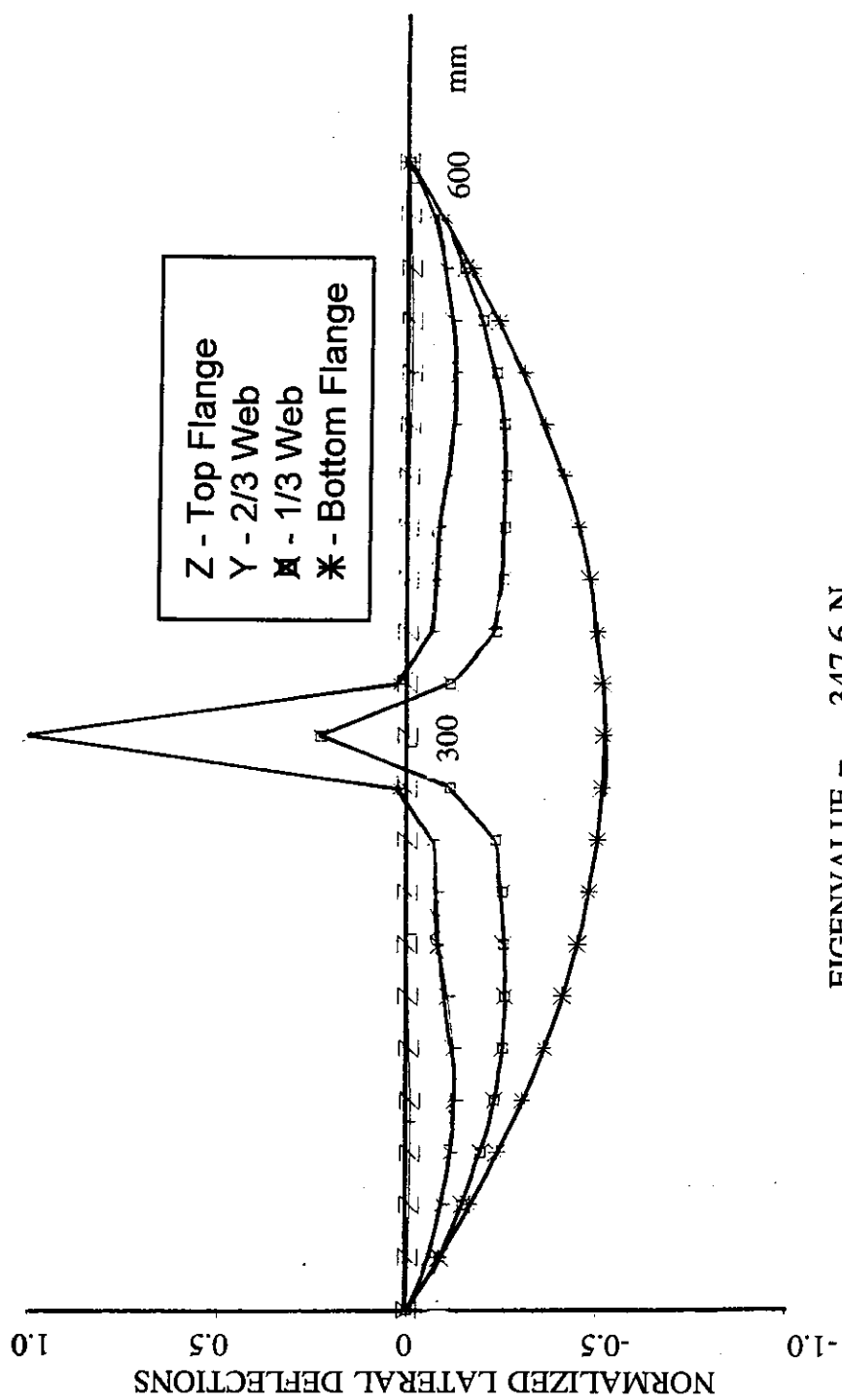
EIGENVALUE = 347.6 N
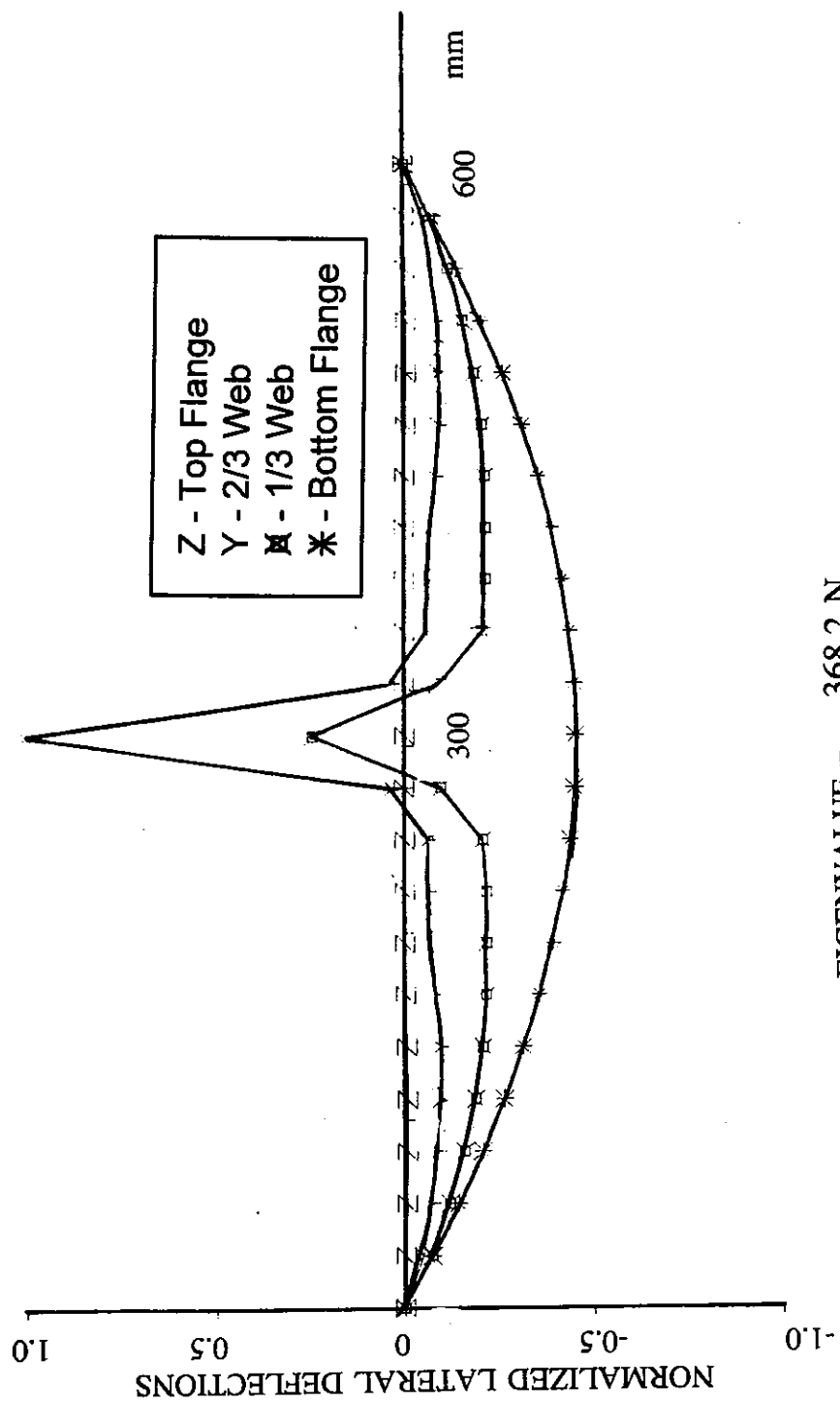
Figure 6.10
Test H FEM Buckled Shape

EIGENVALUE = 320.4 N

Figure 6.11
Test I FEM Buckled Shape

EIGENVALUE =   358.6 kN

Figure 6.12
Full Scale Test 1 FEM Buckled Shape

EIGENVALUE =   357.0 kN

Figure 6.13
Full Scale Test 2 FEM Buckled Shape

Z - Top Flange
Y - 2/3 Web
⋈ - 1/3 Web
✳ - Bottom Flange

EIGENVALUE =   492.1 kN

Figure 6.14
Full Scale Test 3 FEM Buckled Shape

EIGENVALUE =   553.0 kN

Figure 6.15
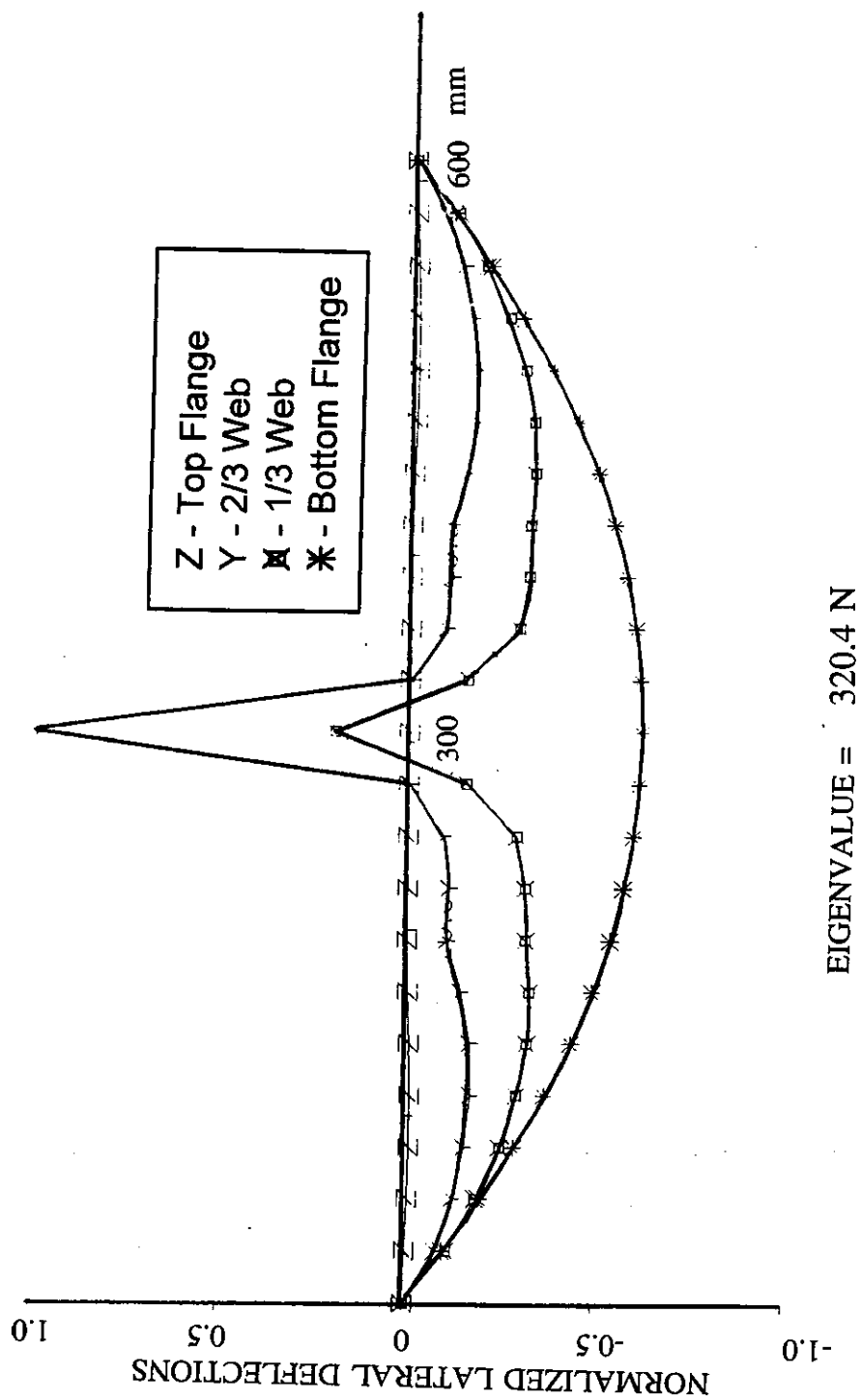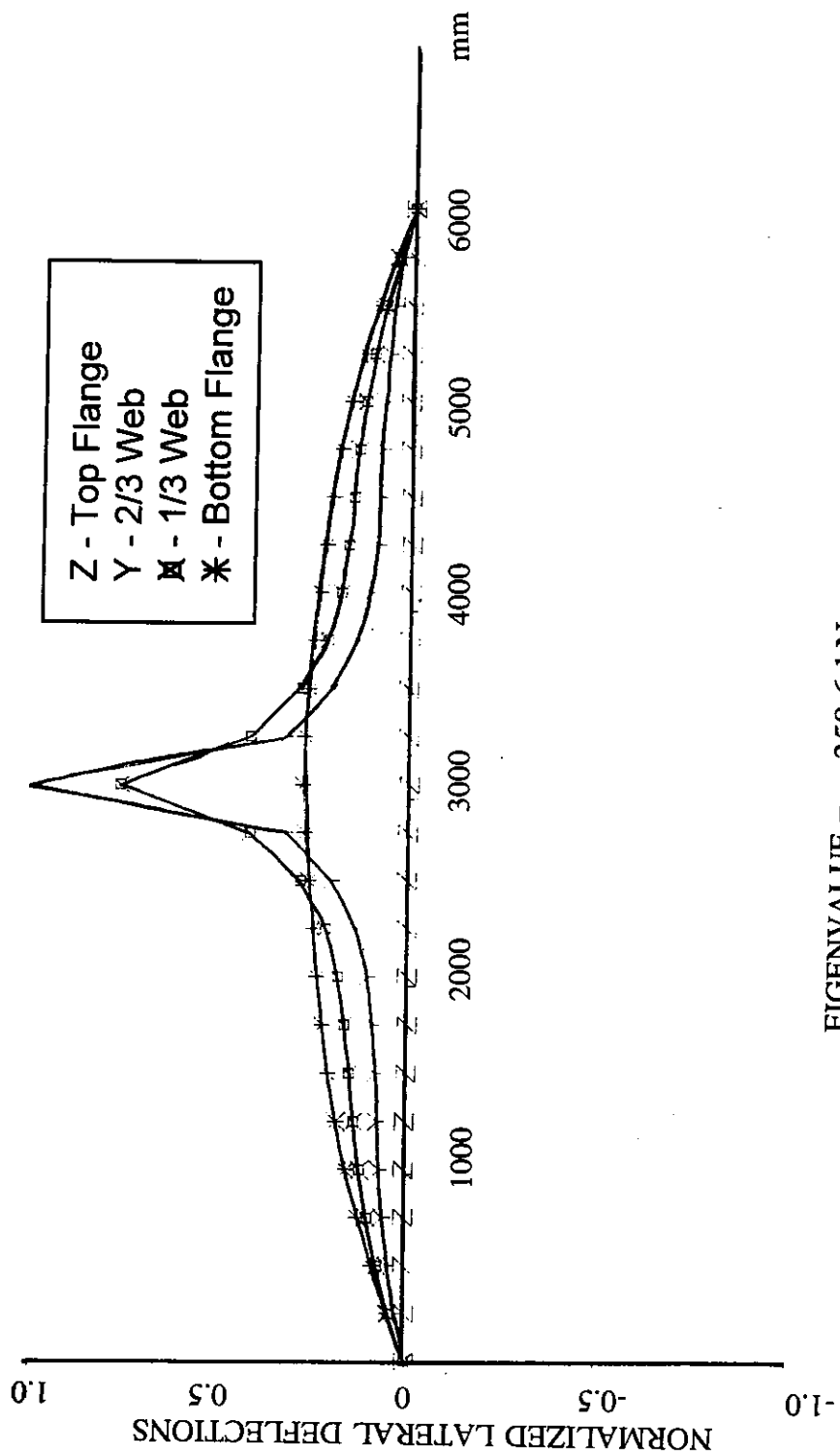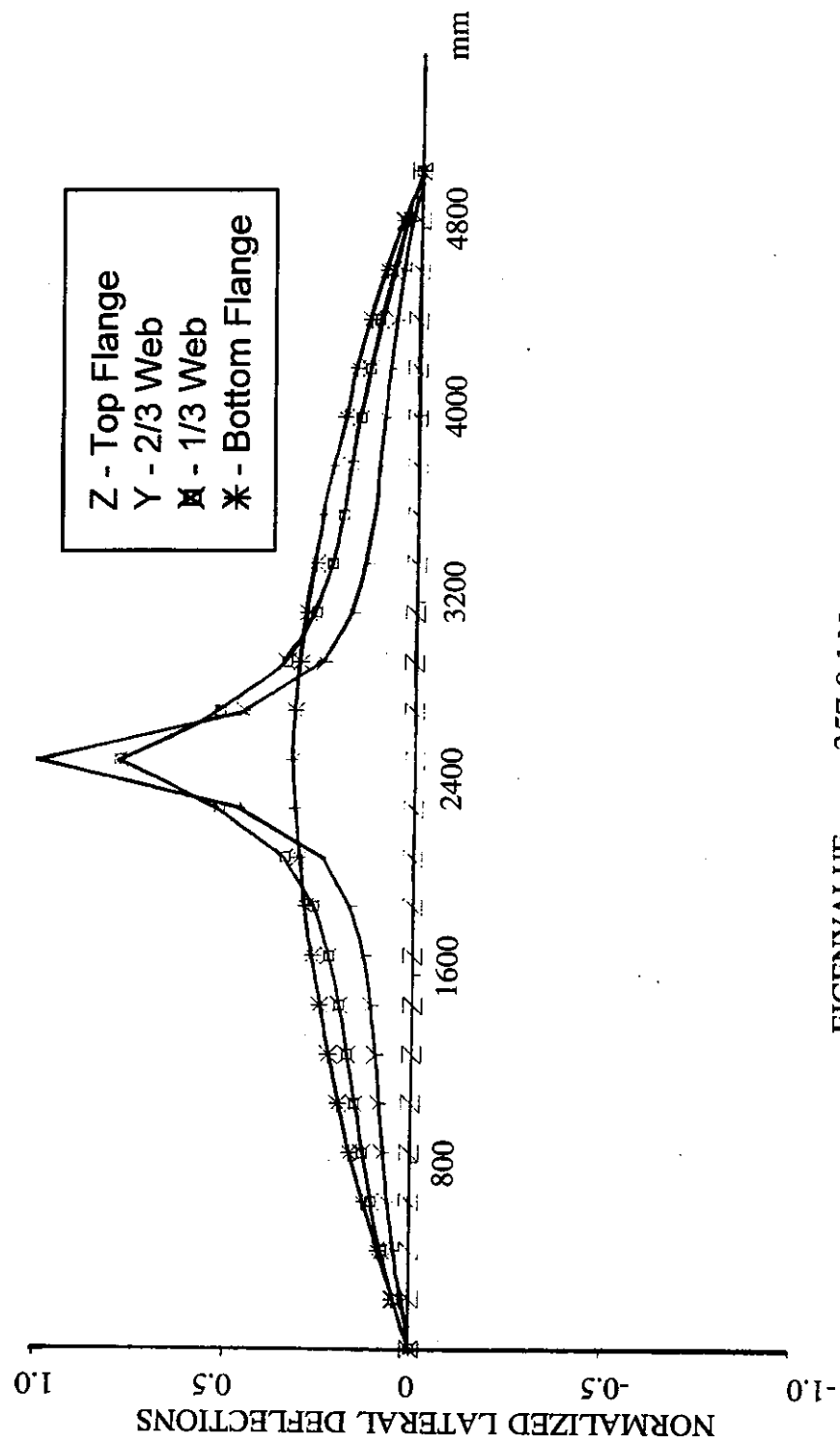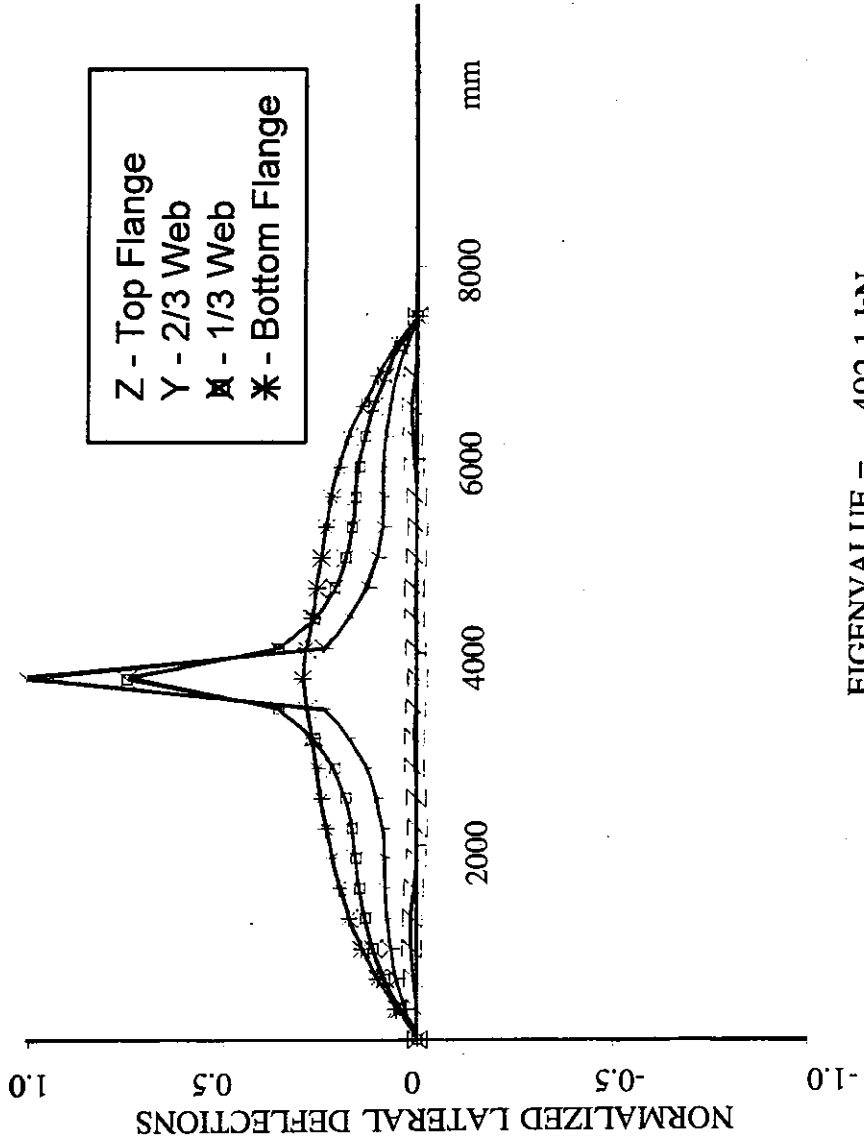Full Scale Test 4 FEM Buckled Shape

EIGENVALUE =   557.0 kN
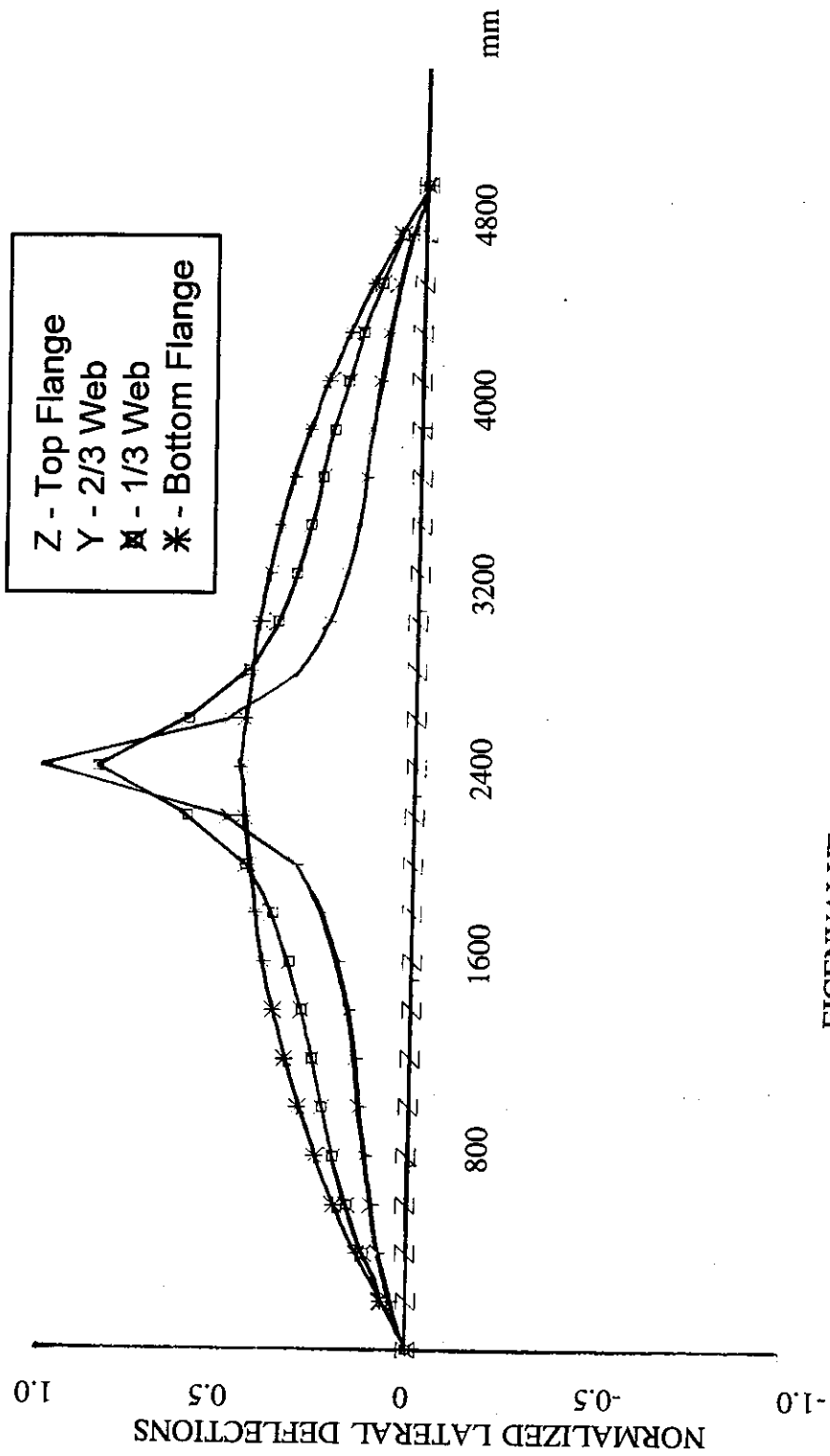
Figure 6.16
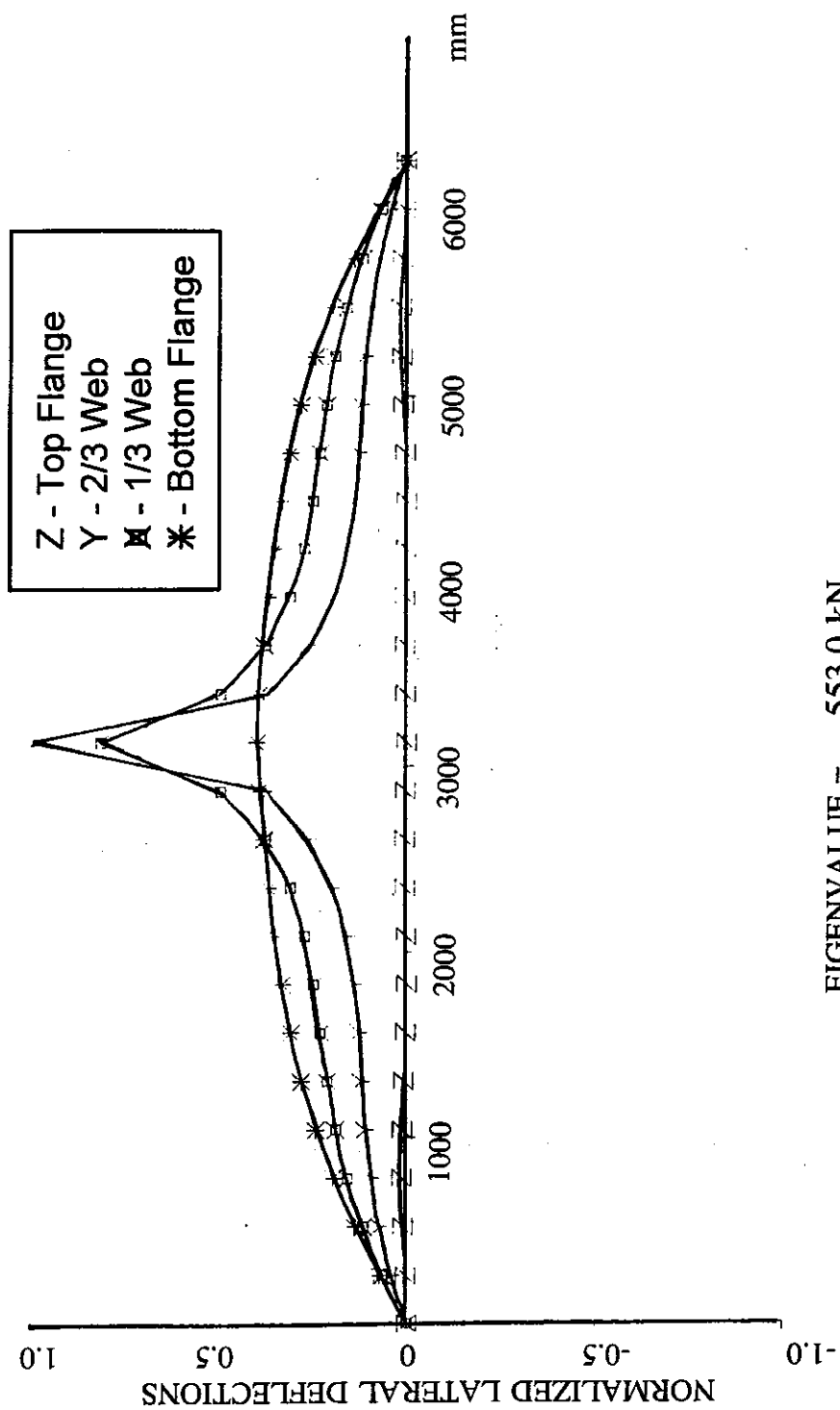Full Scale Test 5 FEM Buckled Shape

7   CONCLUSIONS

7.1   Observations

Styrene model specimens failed in tension flange movement as predicted by finite element modelling. The deflected shapes of failed beams were similar to those predicted by the finite element analysis.

All five of the full scale tests exhibited tension flange movement under the point load. Full scale tests 1, 3 and 4 , while designed to reach full plastic moment, could not sustain the unfactored design load. Tests 2 and 5 were stopped prematurely because of excessive out-of-plane deflections and concern about the safety of the test apparatus respectively.

Vertical web stresses observed in the full scale tests were significantly higher than those assumed by *Yura* and did not follow the assumed triangular stress distribution.

Out-of-plane web deflection measurements in the full scale tests indicated no significant web deformation. This was contrary to the finite element analysis prediction for the full scale tests.

Bottom flange warping restraint in the full scale tests was significantly reduced by end conditions.

Elastic end moments were very sensitive to initial conditions in the tests setup. Inflection point position was not constant for full scale tests.

7.2   Conclusions

The tension flange movement failure mode can limit the capacity of point loaded beams, designed to current S16.1 Standard (1989), to loads below the unfactored design strength.

The current S16.1 Standard (1989) does not address the tension flange movement failure mode. Both web crippling and web yielding design equations neglect the possible influence of tension flange movement on web strength.

The AISC-LRFD sidesway buckling provisions provide overly conservative design strengths for full scale tests with test to predicted ratios ranging from 1.395 to 4.743.

Lateral tension flange stiffness can effect the extent of web buckling and the ultimate strength of model beams.

Current predictive models are insufficient to allow accurate prediction of tension flange movement failure loads.

The revised interaction, equations [3.4] and [6.1], is the most consistent predictor of failure load with test to predicted ratios ranging from 0.612 to 1.198 over all tests.

Further research is necessary to develop accurate predictive models of the tension flange movement failure mode.

7.3   Recommendations

Further study must be done to determine the effects of varying end restraining moment, top flange restraint and warping restraint on tension flange movement failure mode.

Further study into the effects of inelasticity through performance of highly inelastic tests and inelastic finite element analysis must be done prior to the development of design standards for the tension flange movement failure mode.

The interaction of web buckling with lateral tension flange restraint must be studied further both by analytical and experimental methods.

The effects of stiffeners and loaded area have not been addressed in any research to date in the area of tension flange movement. Further research must be done to determine the effects of these two variables on tension flange movement failure loads.

REFERENCES

Akay, H.U., Johnson, C.P. and Will, K.M. (1977), Lateral and Local Buckling of Beams and Frames, Journal of the Structural Division, American Society of Civil Engineering, Vol.103 ST9 Sept, pp. 1821-1832.

American Institute of Steel Construction (1986), Manual of Steel Construction, Load & Resistance Factor Design, First Ed., American Institute of Steel Construction, Chicago, Illinois.

American Institute of Steel Construction (1989), Manual of Steel Construction, Allowable Stress Design, Ninth Ed., American Institute of Steel Construction, Chicago, Illinois.

Bansal, J.P. (1971), The Lateral Instability of Continuous Beams, AISI Project 157, Department of Civil Engineering, University of Texas, Austin, Texas, 126 pp.

Canadian Institute of Steel Construction (1991), Handbook of Steel Construction, Fourth Ed., Canadian Institute of Steel Construction, Markham, Ontario.

Canadian Standards Association (1989), CAN/CSA-S16.1-M89, Limit States Design of Steel Structures, Canadian Standards Association, Rexdale, Ontario.

Column Research Committee of Japan (1971), Handbook of Structural Stability, Column Research Committee of Japan, Tokyo, Japan.

Costley, H.E. (1970), Lateral and Local Instability of Continuous Beams, ACE Project 157, Department of Civil Engineering, University of Texas, Austin, Texas, 74 pp.

Galambos, T.V. (1988), Guide to Stability Design Criteria for Metal Structures, Fourth Ed., Structural Stability Research Council, John Wiley & Sons, New York, New York.

Summers, P.B. (1982) The Behaviour of Beams Subjected to Concentrated Loads, Master of Science in Engineering Thesis, Department of Civil Engineering, University of Texas, Austin, Texas, 117 pp.

APPENDIX A

Development of the AISC-LRFD design equations for sidesway web buckling.

For the case of loaded flange rotation permitted, the LRFD equation is based on the following:

$$[A.1] \quad \frac{P_{cr}}{P_E} = \frac{2kd_c}{P_E} \leq 2.0$$

where: P_{cr} Predicted failure load of the system.

P_E Euler buckling load of a web plate d_c wide.

k   Lateral flange stiffness defined below.

d_c Web depth.

In this case the value P_E is irrelevant since it appears on both sides of the expression. The assumption used in the derivation is that a triangular vertical load distribution from P_{cr} to 0 (the *Yura* theory) is approximately equivalent to a constant axial load of $0.5P_{cr}$. The final LRFD equation was derived as follows:

NO SWAY CASE

(See Figure A.1 for the source)

$$[A.2] \; P_{cr} \leq 2P_E \therefore \frac{P_{cr}}{P_E} \leq 2$$

SWAY CASE

(See Figure A.2 for the source)

$$\Sigma M_o = 0$$

$$0.5 P_{cr} \Delta = k \Delta d_c$$

$$[A.3] \; P_{cr} = 2kd_c$$

Equations [A.2] and [A.3] combine to form the failure envelope, equation [A.1].

Lateral flange stiffness must lie between the stiffnesses of the end fixity extremes:

$$Fixed\text{-}Fixed \ldots (\frac{192EI_f}{l^3})$$

$$Pin\text{-}Pin \ldots (\frac{48EI_f}{L^3})$$

Choosing a stiffness between the fixed-fixed and pin-pin case:

$$[A.4] \quad k = \frac{80EI_f}{L^3}$$

Combining the assumed lateral flange stiffness, [A.4] and the sway failure criterion, [A.3] and expanding I_f yields:

$$[A.5] \quad P_{cr} = 2d_c \left(\frac{80 \cdot 29000 \cdot \frac{1}{12} b_f^3 t_f}{L^3} \right) = 386,700 d_c t_f \left(\frac{b_f}{L} \right)^3$$

(Note: E = 29 000 ksi is used for mild steel)

Taking $d_c/t_f = 40$ to represent economical beams, [A.5] can be expressed as:

$$[A.6] \quad P_{cr} \approx \frac{24000 t_w^3}{d_c} \left[0.4 \left(\frac{d_c/t_w}{L/b_f} \right)^3 \right] \leq 2.0 P_E$$

[A.6] is the source of Eq. K1-7 of the AISC-LRFD (1986)

For the case of loaded flange rotation prevented, the same assumptions and procedures can be used to derive the final AISC-LRFD equation, shown as eq.[A.7].

$$[A.7] \quad P_{cr} = \frac{24000 t_w^3}{d_c} \left(1 + 0.4 \left(\frac{d_c/t_w}{l/b_f} \right)^3 \right) \leq 6.0 P_E$$
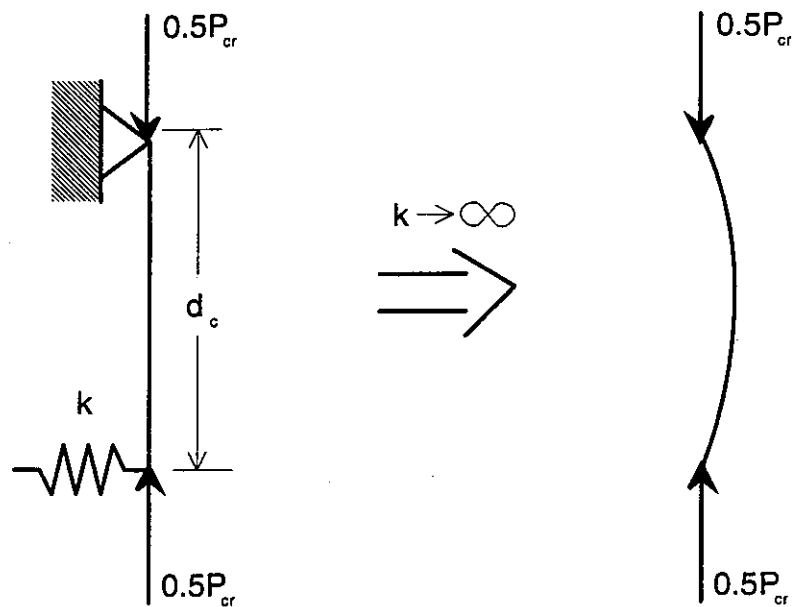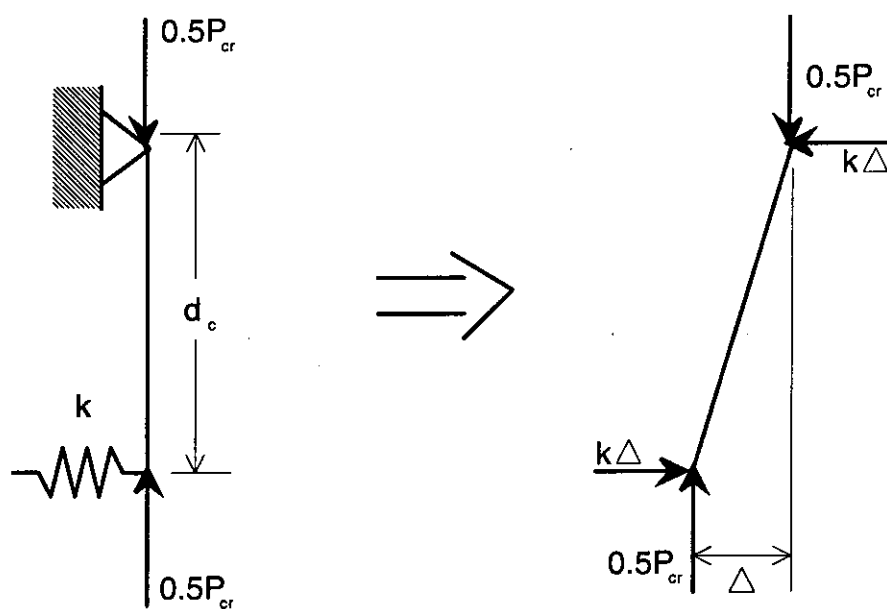
Figure A.1
No Sway Case

Figure A.2
Sway Case

Recent Structural Engineering Reports

Department of Civil Engineering

University of Alberta

181. *Numerical Analysis of Buried Pipelines* by Zhilong Zhou and David W. Murray, January 1993.

182. *Shear Connected Cavity Walls Under Vertical Loads* by A. Goyal, M.A. Hatzinikolas and J. Warwaruk, January 1993.

183. *Frame Methods for Analysis of Two-Way Slabs* by M. Mulenga and S.H. Simmonds, January 1993.

184. *Evaluation of Design Procedures for Torsion in Reinforced and Prestressed Concrete* by Mashour G. Ghoneim and J.G. MacGregor, February 1993.

185. *Distortional Buckling of Steel Beams* by Hesham S. Essa and D.J. Laurie Kennedy, April 1993.

186. *Effect of Size on Flexural Behaviour of High Strength Concrete Beams* by N. Alca and J.G. MacGregor, May 1993.

187. *Shear Lag in Bolted Single and Double Angle Tension Members* by Yue Wu and Geoffrey L. Kulak, June 1993.

188. *A Shear-Friction Truss Model for Reinforced Concrete Beams Subjected to Shear* by S.A. Chen and J.G. MacGregor, June 1993.

189. *An Investigation of Hoist-Induced Dynamic Loads* by Douglas A. Barrett and Terry M. Hrudey, July 1993.

190. *Analysis and Design of Fabricated Steel Structures for Fatigue: A Primer for Civil Engineers* by Geoffrey L. Kulak and Ian F.C. Smith, July 1993.

191. *Cyclic Behavior of Steel Gusset Plate Connections* by Jeffrey S. Rabinovitch and J.J. Roger Cheng, August 1993.

192. *Bending Strength of Longitudinally Stiffened Steel Cylinders* by Qishi Chen, Alla E. Elwi and Geoffrey L. Kulak, August 1993.

193. *Web Behaviour in Wood Composite Box Beams* by E. Thomas Lewicke, J.J. Roger Cheng and Lars Bach, August 1993.

194. *Experimental Investigation of the Compressive Behavior of Gusset Plate Connections* by Michael C.H. Yam and J.J. Roger Cheng, September 1993.

195. *Some Behavioural Aspects of Composite Trusses* by Berhanu Woldegiorgis and D.J. Laurie Kennedy, January 1994.

196. *Flexural Behavior of High Strength Concrete Columns* by Hisham H.H. Ibrahim and James G. MacGregor, March 1994.

197. *Prediction of Wrinkling Behavior of Girth-Welded Line Pipe* by L.T. Souza, A.E. Elwi, and D.W. Murray, April 1994.

198. *Assessment of Concrete Strength in Existing Structures* by F. Michael Bartlett and J.G. MacGregor, May 1994.

199. *The Flexural Creep Behavior of OSB Panels Under Various Climatic Conditions* by Naiwen Zhao, J.J. Roger Cheng, and Lars Bach, June 1994.

200. *High Performance Concrete Under High Sustained Compressive Stresses* by S. Iravani and J.G. MacGregor, June 1994.

201. *Strength and Installation Characteristics of Tension – Control Bolts* by Scott T. Undershute and Geoffrey L. Kulak, August 1994.

202. *Deformational Behavior of Line Pipe* by Mohareb, M., Elwi, A.E., Kulak, G.L., and Murray, D.W., September 1994.

203. *Behavior of Girth-Welded Line Pipe,* by Yoosef-Ghodsi, N., Kulak, G.L., and Murray, D.W., September 1994.

204. *Numerical Investigation of Eccentrically Loaded Tied High Strength Concrete Columns* by Jueren Xie, Alaa E. Elwi, and J.G. MacGregor, October 1994.

205. *Shear Strengthening of Concrete Girders Using Carbon Fibre Reinforced Plastic Sheets* by Efrosini H. Drimoussis and J.J. Roger Cheng, October 1994.

206. *Shrinkage and Flexural Tests of a Full-Scale Composite Truss* by Michael B. Maurer and D.J. Laurie Kennedy, December 1994.

207. *Analytical Investigation of the Compressive Behavior and Strength of Steel Gusset Plate Connections* by Michael C.H. Yam and J.J. Roger Cheng, December 1994.